

UNIVERSITY OF READING

Free and Moving Boundary Problems in Ion
Beam Dynamics.

Peter Spence

February 2012

Submitted to the Department of Mathematics and Statistics, University of Reading, in fulfilment of the requirements for the Degree of Doctor of Philosophy.

Abstract

This thesis models analytically and numerically a moving boundary problem originating in a small particle accelerator known as a neutron tube when a positive-ion plasma is exposed to a large accelerating electric field.

The coupled non-linear system of equations describing the flow of charge within the acceleration region, and the consequent plasma boundary location, are modelled in both one and two dimensions. The one-dimensional study provides an analytic solution to the steady-state problem in planar geometry that arises with given, steady boundary conditions, and goes on to develop a successful numerical method for the determination of a numerical solution to the same problem. The one-dimensional study continues with an analytic analysis of the time-dependent system, concluding with the development of numerical methods devised to analyse the full time-dependent problem. The two-dimensional work builds on the successful one-dimensional time-dependent numerical method, using space-charge limitation to aid in the determination of boundary location techniques, thus developing a model for the steady-state two-dimensional case. The method initially utilises a fixed boundary, iterative method as a vehicle for calculating the initial location of the boundary, and continues, having adjusted the boundary (and hence the solution region), until a termination criterion is satisfied.

Declaration

I confirm that this is my own work and the use of all material from other sources has been properly and fully acknowledged.



P J Spence

February 2012

©Crown Copyright 2012

"This document is of United Kingdom origin and contains proprietary information which is the property of the Secretary of State for Defence. It is furnished in confidence and may not be copied, used or disclosed in whole or in part, without prior written consent of the Director of Commercial 2 Defence Procurement Agency, Ash 2b, Mailpoint 88, MOD, Abbey Wood, Bristol, BS34 8JH, England."

Contents

1	Introduction	18
1.1	Problem Background	18
1.1.1	Neutron Tubes	19
1.1.1.1	Fusion Reactions	19
1.1.1.2	Tube Operation and Plasma Boundary For- mation	22
1.1.2	Previous Work	26
2	Mathematical Formulation	32
2.1	Tonks and Langmuir	34
2.2	Internal Model	38
2.3	Current Model	41
2.3.1	Field Equations	43
2.3.1.1	Time-dependent, Unsteady Equations	44
2.3.1.2	Magnetic Field Influence	46
2.3.1.3	Simplified Time-dependent and Steady-state Systems	47
2.3.2	Solution Region and Boundary Conditions	48
2.3.2.1	Overriding Problems	49

3	The One-dimensional Time-independent Solution	51
3.1	One-Dimensional Planar Time-independent Analytic Solution	52
3.1.1	One-dimensional Planar Canonical Form	55
3.1.1.1	Dimensionless Boundary Conditions	56
3.1.2	Integration of the Planar Canonical Form	57
3.1.3	Inversion of the One-dimensional Planar Solution . . .	59
3.2	One-dimensional Radially Symmetric Time-independent Equa- tion	62
3.2.1	One-dimensional Radial Canonical Form	66
3.2.1.1	Radial Dimensionless Boundary Conditions .	67
3.3	Numerical Methods for the One-dimensional Plasma Bound- ary Problem	68
3.3.1	A Numerical Method for the One-dimensional Planar Problem	68
3.3.1.1	Comparison Between Numerical and Analytic Solution	70
3.3.2	A Numerical Method for the One-dimensional Radial Problem	71
3.3.2.1	Radial ‘Shooting’ Method	74
4	The One-dimensional Time-dependent Solution.	81
4.1	Introduction to the One-dimensional Time-dependent Problem	81
4.1.1	Fields Pertinent to the Problem	83
4.1.2	The One-dimensional Time-dependent System	84
4.2	Analytic Solution	86

4.2.1	Analytic Solution Ahead of the Advancing Charge Front and Associated Separating Characteristic	86
4.2.2	Analytic Solution Behind the Advancing Charge Front	89
4.2.2.1	Linearisation of the Riccati equation	92
4.2.2.2	Determination of $\partial v/\partial x$ at the plasma bound- ary.	93
4.3	Numerical Schemes for the Determination of the Time-dependent Solution	94
4.3.1	Reduction of the Time-dependent System to Dimen- sionless Form	95
4.3.2	Numerical Method 1 for the Determination of the Time- dependent Solution	99
4.3.2.1	Mapping from the Moving Physical Domain to a Fixed Logical Domain	100
4.3.2.2	Numerical Implementation of the Time-stepping Algorithm Using Differences	105
4.3.2.3	Detailed Numerical Algorithm	107
4.3.2.4	CFL condition	116
4.3.2.5	Test Case	119
4.3.2.6	Results	121
4.3.2.7	Method 1 - Summary and Conclusion	133
4.3.3	Numerical Method 2 for the Determination of the Time- dependent Solution	136
4.3.3.1	Detailed Numerical Algorithm	138
4.3.3.2	Test Case	140

4.3.3.3	Results	141
4.3.3.4	Method 2 - Summary and Conclusion	146
4.4	Summary and Conclusion to the One-dimensional Time-dependent Problem	148
5	A Planar Two-dimensional Steady-state Solution	150
5.1	Two-dimensional Time-dependent System	152
5.1.1	Two-dimensional Cartesian Form	154
5.1.1.1	Dimensionless Cartesian Form	158
5.2	Strategy for the Determination of the Two-dimensional Steady-State Solution	161
5.2.1	Solution Algorithm for the Two-dimensional Steady-state Calculation	163
5.2.2	Test Case	171
5.2.2.1	Results	172
5.3	Summary and Conclusion to the Two-dimensional Steady State Model	187
6	Summary, Conclusions and Further Work	191
6.1	Summary and Conclusions	191
6.1.1	One-Dimensional Steady-state Problem	192
6.1.2	One-Dimensional Time-dependent Solution	192
6.1.2.1	Numerical Method 1 for the One-dimensional Time-dependent System	193
6.1.2.2	Numerical Method 2 for the One-dimensional Time-dependent System	195

6.1.3	Two-Dimensional Steady-state Problem	196
6.2	Further Work	198
A	D-T Fusion Reaction Cross-Sections	201
A.1	Kinetic Energy in the CM Frame of Reference.	202
A.2	Reaction Cross-Section in the CM and L Frames of Reference.	204
B	Magnetic Field Effects	206

List of Figures

1.1	Neutron tube schematic.	23
1.2	Schematic showing ions reaching the plasma - vacuum boundary prior to reaching the equilibrium state. In this state, the steady (relative to the timescale of the settling process) current density, $\mathbf{J}_{\text{in}}(\mathbf{x}, \mathbf{y})$, of ions reaching the boundary from below is higher than the current density, $\mathbf{J}_{\text{out}}(\mathbf{x}, \mathbf{y}, \mathbf{t})$, of ions leaving the boundary from above. The horizontal lines are simulated level curves of electric scalar potential. Note that the region is symmetric about the vertical axis.	24
1.3	Schematic showing ions reaching the plasma - vacuum boundary prior to reaching the equilibrium state. In this state, the current density, $\mathbf{J}_{\text{in}}(\mathbf{x}, \mathbf{y})$, of ions reaching the boundary from below is now lower than the current density, $\mathbf{J}_{\text{out}}(\mathbf{x}, \mathbf{y}, \mathbf{t})$, of the ions leaving the boundary from above, since the electric field strength at the boundary has been increased by it bulging into the region, hence causing ions to be extracted more rapidly. The plasma - vacuum boundary now begins to recede. Simulated level curves of electric scalar potential are also shown.	25

1.4	Schematic showing ions reaching the plasma - vacuum boundary at the equilibrium state. In this state, the current density, $\mathbf{J}_{\text{in}}(\mathbf{x}, \mathbf{y})$ of ions reaching the boundary from below is equal to the (now stable) current density, $\mathbf{J}_{\text{out}}(\mathbf{x}, \mathbf{y})$, of ions leaving the boundary from above. Simulated level curves of electric scalar potential are also shown.	26
2.1	The region upon which the complete plasma sheath equation is solved. The Dirichlet voltage conditions $\phi(0) = \phi_0$ and $\phi(r) = \phi_1$ are applied at the region boundaries. Since ions are positively charged, $\phi_0 > \phi_1$	35
2.2	Tube schematic showing the ion beam (marked 'non-zero charge density region'), the charge free region (marked 'zero charge density region'), and the plasma boundary situated directly above the source aperture.	42
2.3	Region of interest, R. The curved line is a representation of the edge of the ion beam, and separates the zero and non-zero charge density regions.	43
3.1	The one-dimensional planar solution region showing the passage of the steady ion beam from the (settled) plasma boundary at $x = s$ to the fixed target location at $x = x_T$. Plasma expands from some location to the left of the plasma boundary and is accelerated away from the boundary by the electric field arising from the applied potential difference. The lines $x = s$ and $x = x_T$ correspond to the boundaries S_1 and S_6 , respectively, in Figure 2.3.	54

3.2	One-dimensional radial solution region. The plasma is expanding from the centre of the two concentric circles (only half of the region is shown) and the plasma boundary (marked interface) forms some radial distance away from this central point at $r = s$. The <i>target</i> is located at $r = r_T$. Since the ions are positively charged, $\phi_S > \phi_T$.	63
3.3	Numerical and analytic solutions to the one-dimensional planar plasma boundary problem at different applied source potentials (initial energy and current density is the same in each case). The accumulation of points towards the left of the calculated numerical solutions is caused by the error control procedure within the solver (described above).	72
3.4	Numerical results from the radial shooting method. Curves show the variation in potential with distance away from the inner plasma free boundary (to the left) to the target (to the right). Solutions for a number of differing sets of initial conditions are shown.	78
4.1	One-dimensional planar solution region showing (in the short timescale) the rapidly advancing charge wavefront. Plasma expands from some location to the left of the time-dependent plasma boundary (at $x = s(t)$) and is accelerated away from the boundary by the electric field arising from the applied potential difference. The region to the left of the wavefront has non-zero charge density, whilst that to the right has zero charge density. The target is fixed and located at $x = x_T$, as before.	83

4.2	Actual characteristic curves spanning the charge free part of the solution region enclosed by the separation characteristic, the lower $t = 0$ boundary and the right hand fixed target. An impression of the moving plasma boundary is shown (marked $s(t)$).	90
4.3	Function used to represent time-dependent charge density ramp. The parameters h , b , and c in (4.56) are indicated. The subscript n in the axis titles indicates a non-dimensional variable.	109
4.4	The charge density surface $\rho(x, t)$. Output is shown at every 200 time steps.	124
4.5	Logarithmically spaced level curves of constant charge density over the first ~ 93 ns.	125
4.6	Logarithmically spaced level curves of constant charge density over the first ~ 10 ns.	126
4.7	The variation of electric scalar potential (voltage) with distance across the region at different solutions times. The analytic steady state solution and steady boundary location are shown.	127
4.8	Variation in plasma boundary location $s(t)$, and plasma boundary perturbation $\Delta s(t)$, with time.	128
4.9	Estimated time at which the boundary perturbation $\Delta s(t)$ becomes negative.	129
4.10	Estimated algorithm execution time to reach the point at which the boundary perturbation $\Delta s(t)$ becomes negative. Points marked “observation” were taken from the current Case.	130

4.11	Estimated number of time-steps to reach the point at which the boundary perturbation $\Delta s(t)$ becomes negative. Points marked “observation” were taken from the current Case.	131
4.12	The electric field surface $E(x, t)$, with adaptive parameter $\mu = 100$ (region start size of $L = 0.009$ m). Output is shown at every 40 time steps.	132
4.13	Variation in potential $\phi(x, t)$, with x at three specific times. Setting the adaptive parameter, μ , to be equal to ten leads to increased nodal density towards the left of the curves, as time increases. . . .	133
4.14	Variation in nodal location for the first fifteen nodes in physical space. Nodes rapidly move from an equally spaced distribution to being concentrated near the plasma boundary (where the charge density gradient is greatest).	134
4.15	The variation in nodal separation with node number at different solution times. The ordinate value at node 2, for instance, refers to the distance $x_2^k - x_1^k$ (for time-step k).	135
4.16	The charge density surface $\rho(x, t)$. Output is shown at every 600 time steps.	143
4.17	Equally spaced level curves of constant charge density for the entire solution (up to $0.9\mu s$).	144
4.18	The potential surface $\rho(x, t)$. Output is shown at every 600 time steps.	145
4.19	The analytic steady-state solution (red circles) with the calculated potential solution $\phi(x, t)$ at $t = 900ns$ (black solid line with 150 nodes).	145

4.20	Error in final calculated solution potential as a function of distance. The error is calculated as $\text{error}\% = \frac{100 \times (\phi(x, t_e) - \phi_a(x))}{\phi_m}$, where t_e is the final time (900ns in this case) and $\phi_a(x)$ is the analytic steady-state solution.	146
4.21	The variation in boundary location, $s(t)$, with time. The calculated boundary asymptotes to the analytic steady-state location as the source charge density ramp reaches its maximum value.	147
4.22	The variation in boundary perturbation, $\Delta s(t)$, with time. The perturbation, calculated from (4.79), asymptotes to zero as the source charge density ramp reaches its maximum value.	147
5.1	Region of interest, R . The curved line is a representation of the edge of the ion beam, and separates the zero and non-zero charge density regions.	151
5.2	Constant charge density profile along the emission boundary. The region line of symmetry is located at $x/L = 0$, the midpoint of the ramp transition is at c_x/L (in this case at $x/L = 0.16$, shown by the black square marker) and a measure of the transition width (the distance between the two red, circular markers) is given by w_x/L ($w_x/L = 0.0286$ in this case).	165

5.3	The location of the level curve corresponding to zero electric field magnitude, and nearest grid nodes. The blue line is the level curve, whilst the black, square markers are the nodes identified as being nearest this curve. Information is displayed in dimensional space, with the right hand edge of the flat emission boundary (x_E) being located at $x = 0.01\text{m}$. After the initial fixed boundary solution, nodes below the blue line are considered to be outside of the region.	170
5.4	After the initial calculation stage, the new boundary location is calculated to be the blue line. The nodes within the fixed grid that are closest to this boundary are shown as the black, square markers. A small part of the underlying computational grid is also shown.	173
5.5	The modified boundary conditions for v_x and v_y as a consequence of the new boundary shown in Figure 5.4.	174
5.6	The initial potential solution surface.	175
5.7	Initial potential solution level curves. The calculated, new plasma boundary is just visible and is shown as the blue line to the bottom left of the figure.	175
5.8	The initial charge density solution surface. The ramp along the emission surface (to the upper right of the figure) is visible, where the charge density at the emission surface decays rapidly from its maximum (j_0/v_i) to zero when at 4/5 distance along.	176
5.9	Initial charge density level curves. The highest charge density is shown in red, immediately above the emission region.	176

5.10	x component of velocity. The sharp ridge is evidence of mutual charge repulsion within the ion beam and shows evidence of lateral acceleration caused by this.	177
5.11	x component of velocity level curves. A small degree of beam splaying is evident.	178
5.12	y component of velocity.	178
5.13	Comparison between two-dimensional v_y component (along the y -axis line of symmetry) and the one-dimensional calculated velocity of a deuteron under the acceleration caused by the calculated steady-state accelerating voltage. It is noted that the one-dimensional curve does not reach the source boundary, as a consequence of the steady-state reduced region size.	179
5.14	MRMS with iteration number - stage 1.	179
5.15	Calculated boundary location for stage 2. The blue line shows the new boundary location and the black, square markers are the nodes nearest the boundary on the underlying grid. The red line is the boundary location calculated from the previous stage.	180
5.16	The modified boundary conditions for v_x and v_y as a consequence of the new boundary shown in Figure 5.15.	181
5.17	Stage 2 potential solution surface. Nodes behind the new emission boundary have been removed to highlight their location (just visible to the upper right) and do not contribute to the next stage.	182

5.18	Stage 2 potential solution level curves. There is advancement of the curves nearest the boundary from stage 1. The new, calculated plasma boundary is shown as the blue line to the bottom left of the figure.	183
5.19	The particle number density across the target. The very outer edge of the beam is considered to be when the number density falls below one particle per cubic metre (in this case at 0.015 m).	184
5.20	MRMS with iteration number - stages 1 and 2.	184
5.21	Calculated boundary location for stage 3. As before, the blue line shows the new boundary location and the black, square markers are the nodes nearest the boundary on the underlying grid. The red and green lines are the boundary locations from steps 2 and 1, respectively.	185
5.22	Stage 3 potential solution surface. Nodes behind the new emission boundary have been removed to highlight their location.	186
5.23	Stage 2 potential solution level curves. The calculated plasma boundary is shown as the blue line to the bottom left of the figure. The gap between the boundary and the first curve indicates that the solution is not changing rapidly there.	187
5.24	The electric field magnitude across the region. The electric field reaches zero at the plasma boundary, as required by (5.2c) (or the dimensionless equivalent).	188
5.25	The particle number density across the target. The very outer edge of the beam is considered to be when the number density falls below one particle per cubic metre (in this case at 0.014 m).	189

5.26	MRMS with iteration number - stages 1, 2 and 3.	189
6.1	Experimental accelerator set-up. The components shown in the schematic are encased in a sealed envelope, with the required potential difference between the source shield and target scintillator applied with a large pulse forming network.	199
A.1	Reaction cross-section as a function of energy for the D-T reaction in the CM frame of reference (black), with the scaled cross-sections for both the D-T (red) and T-D (blue) in the laboratory frame of reference also shown. The cross-section peaks occur at $\bar{E} \sim 66$ KeV for the CM frame, $E \sim 110$ KeV for D-T in the laboratory frame and $E \sim 165$ KeV for T-D in the laboratory frame. The original CM curve was taken from [4] and [5].	205

Chapter 1

Introduction

1.1 Problem Background

Neutron generators have been used as exploratory tools for a number of years, with the highly sensitive specific technique of Neutron Activation Analysis (NAA) being used to determine the elemental content of materials to a high degree of accuracy (See [39]). The method of NAA involves the illumination of the required sample by a pulse (or pulses) of neutrons resulting in the release of a characteristic signature from the sample, in the form of other types of radiation.

During the neutron illumination process, the sample becomes activated and subsequently emits secondary gamma radiation in two phases, as it de-activates. The first phase is a rapid de-excitation of the activated nuclei via gamma decay where the characteristic gamma frequencies are particular to the element originally excited. The second phase is a radioactive decay process from unstable isotopes formed from the neutron illumination process, the decay rates being strongly dependent upon the isotopes formed (half

lives ranging from 10^{-3} to 10^7 years). It is usually this second phase that is analysed to determine information about the sample constitution.

For many applications of NAA, the neutron source is a large, laboratory-scale piece of apparatus. However, in some applications (such as oil well logging), such a large scale piece of equipment cannot be used, and so the neutron source must be taken to the location of the sample. In this case, the neutron source is a much smaller device and is a *neutron generator*, comprising a power supply and sealed *neutron tube*.

The problem analysed in this thesis originates within a neutron tube that has an entirely different application, where it is used in nuclear weapon initiation. Briefly, the short, very intense pulse of neutrons created by the neutron tube is used to initiate a fission chain reaction within a nuclear weapon¹ [40].

1.1.1 Neutron Tubes

1.1.1.1 Fusion Reactions

In order to generate neutrons within a neutron tube, fusion² reactions are employed. By utilising fusion, the creation of neutrons can be precisely timed

¹A more detailed description of this application cannot be given due to classification issues.

²If fission reactions were to be used as a neutron source, a donor reactant would be chosen whose spontaneous fission products would be introduced to another fissile material. Subsequently, a further fission reaction would take place and one of the products of this second fission reaction would include neutrons with a specific energy. Creating neutrons by fission is less controllable by virtue of the spontaneous decay of the fission reactants, and on the chemical mixing of such materials.

and controlled by initiating the reaction only when required.

To create the fusion reaction within the tube, an ion beam consisting of one of the fusion reactants is accelerated to a relatively high energy towards a stationary target that is infused with the other reactant. The energy to which the incident particles are accelerated is chosen depending upon the fusion reaction *cross-section*, and is dependent upon the particular reaction concerned. The reaction cross-section relates to nucleon - nucleon scattering, and is a measure of the probability of a particular reaction taking place (see [21], and Appendix A). It effectively gives an indication of the apparent size of the target nucleon for a given reaction and given energy. The reaction cross-section has the dimensions of area and is usually measured in *barns* where 1 barn is 100fm^2 or 10^{-28}m^2 . Sometimes, the reaction cross-section is given in a centre of mass frame of reference. In this reference frame, the reaction probability is independent of the total momentum of the reacting particles relative to the laboratory. The D-T cross-section referred to in this thesis is measured in the laboratory frame of reference, where the target particle is stationary relative to the laboratory. It is scaled from the generic centre-of-mass frame of reference cross-section (for the two given reactants) according to the reacting particle masses (Appendix A).

Most fusion reactions capable of creating neutrons have negligible reaction cross-sections (i.e. they do not generate an appreciable number of neutrons for a given energy) unless the incident ion is accelerated to such high energies that the process is virtually impossible to achieve in a small neutron tube. This is since the large electrostatic potential used to accelerate ions must be held-off across a small distance of the order of mm . The term hold-off

refers to the high voltage electrodes within the neutron tube being separated by an insulating wall. The insulator used is usually a ceramic that not only separates the electrodes and hence resists electrostatic breakdown (where the potential energy of electrons at the cathode is so great that they are able to jump the gap between the electrodes either directly across the vacuum gap, or by skipping along the ceramic wall), but it also maintains a seal that resists permeation from gases within the atmosphere, thereby maintaining the vacuum within the sealed tube.

To utilise low cross-section reactions, not only would the device have to be relatively large (scaled by, say, a factor of ten) and cumbersome, but the tube power supply would need to generate the huge potential differences necessary to drive the reaction; this is very difficult to achieve. Therefore, it is usual for a neutron tube to utilise the deuterium-tritium fusion reaction (or D-T reaction), whereby deuterium ions are accelerated on to a stationary (relative to the laboratory) tritiated target. This reaction has a relatively high peak cross-section, which occurs when the incident deuteron has a kinetic energy of $\sim 110\text{KeV}$. It is noted that the converse T-D (tritium-deuterium) reaction, whereby tritium ions are accelerated onto a stationary deuterium target, has a peak cross-section when the incident triton has a kinetic energy of $\sim 165\text{KV}$ (see Appendix A). The laboratory frame reaction cross-sections for these reactions are shown in Figure A.1.

For the D-T fusion reaction to take place with the maximum probability, deuterium ions must be accelerated to an energy of $\sim 110\text{KV}$ before striking the tritium impregnated target. Upon striking the target, some of the incident deuteron particles fuse with the tritium within the target (the

proportion of fused incident ions being dependent upon the reaction cross-section) consequently releasing neutrons with 14.1MeV in addition to 3.5MeV alpha particles. Those deuterium ions that do not fuse with tritium lose energy as they penetrate the target, thereby losing some of their ability to fuse (by effectively sliding down the cross-section curve) at the next interaction.

1.1.1.2 Tube Operation and Plasma Boundary Formation

Geometrically, the tube consists of a sealed envelope, across which the $\sim 110\text{KV}$ electrostatic potential difference is held off by a ceramic wall. A source of deuterium ions is situated at the anode end of the tube whilst the tritiated target is at the cathode end (see Figure 1.1). Upon operation, a plasma of deuterium ions expands into the acceleration gap acting as a conductive ‘gas’ which is generally impenetrable to the tube main accelerating field (due to its conductivity). At about the same time, the $\sim 110\text{KV}$ accelerating voltage is applied across the tube and ions begin streaming away from the plasma-vacuum interface (the plasma boundary) formed by the expanding plasma. Shaped electrodes within the tube act as ion lenses focussing the ion beam onto the tritiated target where the fusion reaction takes place.

There are two distinct timescales that exist within the operation of the tube. The timescale over which the source operates and the accelerating voltage is applied, is generally several orders of magnitude greater than the timescale over which the plasma boundary settles to a stable position for a given set of conditions. The accelerating voltage is ramped up in a period of μs , whereas for a given impulse, the boundary settling process occurs in a period of ns.

Since the tube operates in a dynamic manner, whereby the source and

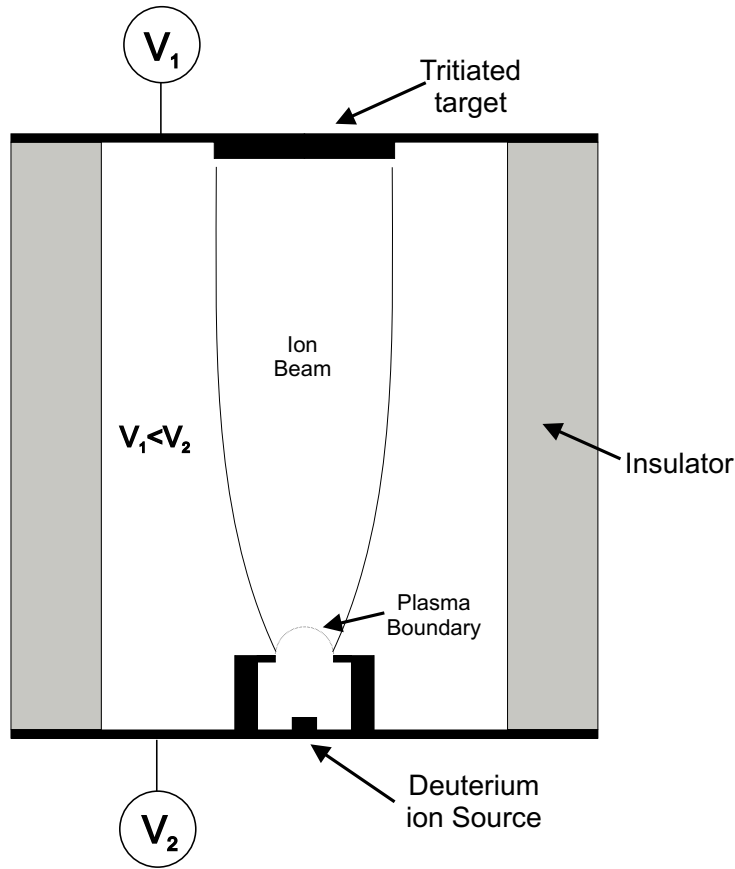


Figure 1.1: Neutron tube schematic.

accelerating voltage are switched on, reach relatively stable conditions and are then switched off, then due to the relatively long time scales of the source drive and acceleration voltage pulses (in comparison to the timescale of the boundary settling process), it is believed that the boundary moves in accordance with the applied acceleration voltage, eventually settling to a stable location during the relatively stable phase of tube operation. The boundary movement process takes place in the following way.

Ions reaching the plasma-vacuum boundary at a specific rate cause the boundary to bulge into the vacuum (see Figures 1.2 and 1.3 where the ion

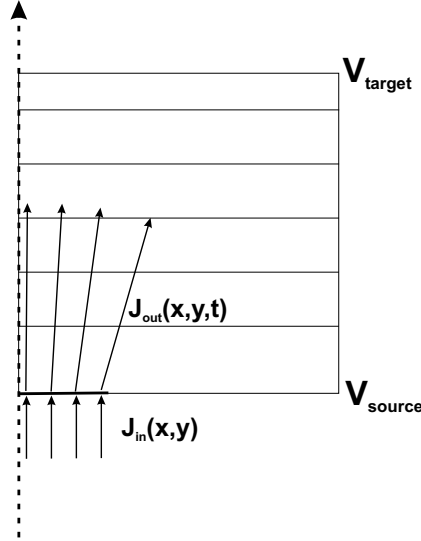


Figure 1.2: Schematic showing ions reaching the plasma - vacuum boundary prior to reaching the equilibrium state. In this state, the steady (relative to the timescale of the settling process) current density, $\mathbf{J}_{\text{in}}(\mathbf{x}, \mathbf{y})$, of ions reaching the boundary from below is higher than the current density, $\mathbf{J}_{\text{out}}(\mathbf{x}, \mathbf{y}, \mathbf{t})$, of ions leaving the boundary from above. The horizontal lines are simulated level curves of electric scalar potential. Note that the region is symmetric about the vertical axis.

arrival rate and departure rates are represented by the current densities $\mathbf{J}_{\text{in}}(\mathbf{x}, \mathbf{y})$ and $\mathbf{J}_{\text{out}}(\mathbf{x}, \mathbf{y}, \mathbf{t})$ respectively), thereby concentrating the electric field within the region (since the plasma acts as a Dirichlet boundary condition for the electric scalar potential within the tube main gap). The increased electric field (as a consequence of the reduction in electrode separation) causes ions to be accelerated away from the boundary more rapidly than they arrive there, and consequently the boundary recedes until the electric field at the boundary becomes zero [8] (see Figure 1.4). In this equilibrium state, ions leave the boundary at the same rate as they arrive there, and the the

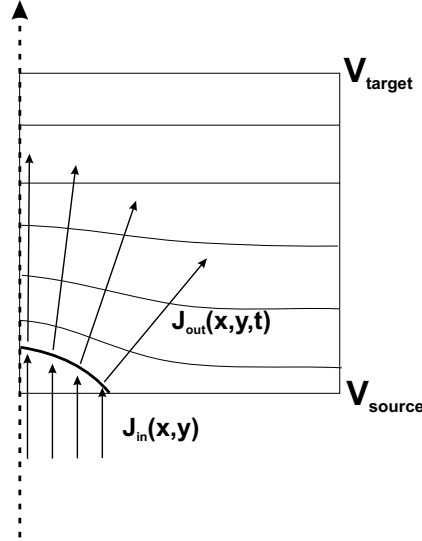


Figure 1.3: Schematic showing ions reaching the plasma - vacuum boundary prior to reaching the equilibrium state. In this state, the current density, $\mathbf{J}_{in}(\mathbf{x}, \mathbf{y})$, of ions reaching the boundary from below is now lower than the current density, $\mathbf{J}_{out}(\mathbf{x}, \mathbf{y}, \mathbf{t})$, of the ions leaving the boundary from above, since the electric field strength at the boundary has been increased by it bulging into the region, hence causing ions to be extracted more rapidly. The plasma - vacuum boundary now begins to recede. Simulated level curves of electric scalar potential are also shown.

plasma-vacuum boundary position has stabilised.

The determination of the position of the plasma-vacuum boundary during the settling process is a moving boundary problem, in which the boundary converges to an equilibrium position over a short period of time. On the timescale of the overall tube operation, the determination of the plasma-vacuum boundary position for a given source current density³ and accelera-

³The source current density profile is determined by the source metallurgy and geometry in addition to currents and voltages applied to it.

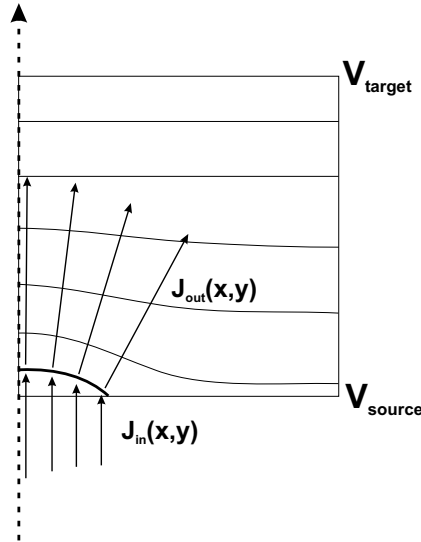


Figure 1.4: Schematic showing ions reaching the plasma - vacuum boundary at the equilibrium state. In this state, the current density, $\mathbf{J}_{\text{in}}(\mathbf{x}, \mathbf{y})$ of ions reaching the boundary from below is equal to the (now stable) current density, $\mathbf{J}_{\text{out}}(\mathbf{x}, \mathbf{y})$, of ions leaving the boundary from above. Simulated level curves of electric scalar potential are also shown.

tion potential difference is also a free boundary problem. It is the purpose of this analysis to determine the free boundary positions for problems with given steady state source current densities and acceleration voltages using mathematical techniques tailored to the problem. In addition, the full time dependent moving boundary problem occurring at the shorter timescale is also explored.

1.1.2 Previous Work

The problem of determining the position of the plasma boundary within an ion accelerator setup is one that has attracted a good deal of attention,

particularly in the 1960s and 1970s. As a consequence, I have had to deal selectively with the references in an attempt to develop a coherent account of past work, without reviewing subject matter that does not directly influence the current work (although some of this experimental work is mentioned in passing). Here I present a general history of related work, but detail on some of the more relevant works is given in Chapter 2.

Tonks and Langmuir [2] first theoretically analysed the behaviour of a plasma expanding into a region with an applied electric field by investigating low pressure plasma discharge within a discharge tube (a plasma is defined as a neutral *gas* consisting of electrons and positive ions). In this work, the ion number density distribution within such a plasma is determined by approximating solutions to specific cases of what they called the ‘complete plasma sheath equation’ (an integro-differential equation) in one dimension for different geometries (more general solutions of this equation were also considered by Self [7]).

The analysis of Tonks, Langmuir and Self detailed specifically the behaviour of an expanding plasma up to and including the plasma sheath⁴ (or the plasma boundary), but their analysis was unable to adequately describe the self-consistent electric field outside the plasma region (beyond the sheath). This was primarily due to their representation of the ion number density (the free charge density of ions divided by their charge) within the plasma being no longer valid outside the plasma region. More recently, in an independent work ([11]), a similar approach (to Tonks and Langmuir) was adopted, but the ion number density within the plasma region was calculated

⁴The region where electrons within the plasma are repelled by the external electric field.

from the ion equations of motion instead of using the approach of Tonks and Langmuir. This enabled the calculation of the correct potential distribution outside the plasma region, whilst also determining the position of the plasma sheath, although the ion number density within the plasma was not correct. This is true because the representation of ion acceleration outside the plasma region is correct, but inside the plasma region it is not correct. The disconnected nature of the plasma region and ion acceleration region enables this to be the case. Electric scalar potential distributions for a specific application were then calculated in one dimension. As a way of determining the plasma sheath thickness and position a Maxwell-Boltzmann distribution ([18]) was used to represent the electron number density within the plasma (as in previous works) and solutions were approximated by asymptotic methods.

Other work detailing the behaviour of an expanding plasma originate from the experimental discovery by Tonks and Langmuir in 1929 ([1]) of plasma oscillations (the ability of a neutral plasma to support wave motion and potentially shock like behaviour). Previous models (such as those mentioned above) of the plasma behaviour were unable to support such oscillations. The inclusion of the Vlasov equations ([41], [32]) (a hyperbolic system describing the behaviour of the ion number density in a plasma with a long range charge interaction) as a description of the ion charge density would enable such plasma oscillations to occur within the plasma model. Works such as Whealton *et al* [12] and Whealton, Bell *et al* [22] solve the non-linear Vlasov-Poisson system (a similar system to that originally proposed by Tonks and Langmuir but where the ion number density is determined from the Vlasov equation) and consequently trace ions through the plasma and into

the electrostatic field in a Lagrangian manner.

Treating ions as particles and tracing them through calculated field solutions is a method commonly used for the determination of the ion charge density outside the plasma region in ion beam numerical methods (refer, for example, to [28] and [31] in addition to references mentioned above). There are several problems associated with this method of predicting the ion beam location, the most notable being the number of ion beams that must be used to accurately represent the charge density distribution within the solution region. Not only is accurate ion beam tracing very computationally intensive, but accurate methods of assigning the calculated space charge density to the field solver mesh must be used as part of the computation procedure ([27]).

Most field solvers used in ion beam tracing codes have used static mesh finite difference approximations to the field equations. However in 2004, Humphries [37] proposed a free surface finite element approximation to the plasma boundary problem, whilst maintaining the Lagrangian particle tracing procedure. In this work, the free surface position is determined by maintaining a constant ion current density at the surface (thereby placing the required additional boundary condition there). Nodes along the emission surface are iterated to a stable position by moving them at each iteration with the distance moved being determined from how far away from the required constant current density the calculated emission current density is. For a more in depth history of work in this area (until 1983) refer to Lejeune [16] where a very comprehensive set of references is also listed.

Our interest essentially follows on from [11], but we are not interested

in the plasma or plasma sheath per-se (as many previous works are). Consequently we concentrate on the boundary value problem that the plasma expanding into an electric field presents. Since we are not interested in the plasma, but merely the plasma boundary position, we do not include the electron number density in calculations and seek the plasma boundary position as a consequence of other conditions. The known (from experiment) current density distribution at the plasma boundary is used (this is not necessarily constant in position) in conjunction with a calculated ion charge density (from the ion equation of motion), and extra Neumann boundary conditions (see [8]) at the plasma boundary. We calculate the electric scalar potential distribution in addition to the charge density and charged particle velocity distributions, treating the particle velocity as a conservative field. Also, the position of the plasma boundary or the ion emission region shape (treating this boundary as the edge of the solution region) is calculated both analytically and numerically in one dimension and numerically in two-dimensional planar geometry.

We begin by discussing in detail, the formulations of Tonks and Langmuir and of the internal work (these are most relevant to the model adopted in this thesis), [11], in addition to some of the other work mentioned above. Subsequently, we formulate a mathematical description of the problem investigated here, discussing methods employed to solve the problem. Our analysis begins with a solution of the simpler one-dimensional steady state problem, and follows with a full time dependent solution of the one-dimensional problem with a moving boundary. Following on from this, using information acquired

in the one-dimensional case, an approach to solving the more difficult two-dimensional case is given whereby the time dependency in the field equations is used in a pseudo manner as a device for obtaining convergence in the free boundary case.

Chapter 2

Mathematical Formulation

The situation outlined in Chapter 1 corresponds to a system of coupled problems describing the various phenomena occurring within a neutron tube during normal operation. These phenomena, as previously indicated, can be broken down into four main areas and are listed as follows.

1. Source Operation and Plasma Expansion

The tube ion source produces a plasma consisting of both positively charged deuterium ions and electrons. After release from the ion source, the plasma expands into a field free region (termed the plasma cup) until it meets the high voltage accelerating field by passing through an aperture.

2. Plasma - Vacuum boundary

As the neutral plasma reaches the high voltage accelerating field region of the neutron tube, a sheath forms at the boundary between the neutral plasma and acceleration region. Within the sheath, the density of electrons gradually reduces with distance into the acceleration

region until all electrons are repelled by the electric field. We define this location as the plasma - vacuum boundary, and it corresponds to a boundary shape whereby the flux of ions reaching it from the source is matched by the flux of ions leaving it towards the target. It is also defined by a zero field condition (see [8]) since if a non-zero electric field were to exist on the acceleration field side of the boundary¹, then ions will be extracted from the boundary more rapidly than they arrive there from the plasma side and the boundary would adjust until the balance is restored. The shape of the boundary is dependent upon the deuterium ion current density across it, the potential difference across it, and the geometry of the acceleration region, in addition to the zero field condition at the boundary.

3. Acceleration Region

Once ions reach the plasma boundary, they are extracted and accelerated towards the target. The electric field within the acceleration region is dependent upon the charge density within it, the potential difference applied across it, and the shape of the plasma boundary formed at the anode. The ion beam shape is also dependent upon the electric field and hence its own charge density.

4. Target

After being accelerated across the neutron tube, the (now) high energy ions strike the tritiated target undergoing fusion, and release 14.1 MeV neutrons isotropically.

¹A plasma by definition is a field free region.

For reasons that will become more apparent in the following sections, it is possible to decouple the behaviour of ions within the plasma from ions within the acceleration region. Since we are not specifically concerned with the modelling of the plasma itself, it is only the acceleration region and position of the plasma boundary that is of concern in this thesis. However, two plasma models that lead logically on to the boundary value problem considered here, are now discussed.

2.1 Tonks and Langmuir

As mentioned previously in Section 1.1.2, Tonks and Langmuir ([2]) considered the ion density within an expanding plasma and formulated what they termed the *complete plasma sheath equation*, for a one-dimensional plasma expanding from the origin into a region with a potential difference applied across it (see Figure 2.1). This equation was constructed from the Maxwell continuity equation (or Gauss' Law) relating the divergence of the displacement current from a region to the charge density enclosed within that region. In one dimension this can be written as

$$\frac{d^2\phi}{dx^2} = -\frac{q}{\varepsilon_0} (N_i - N_e), \quad (2.1)$$

where $\phi(x)$ is the voltage (electric scalar potential), q the electron charge, ε_0 a scaling parameter called the permittivity of free space, and N_i and N_e the ion and electron number densities within the plasma, respectively (here it is assumed that ions are singly charged).

Equation (2.1) is written in this form (the charge density as the product of particle charge and number density) to allow the use of the Maxwell-

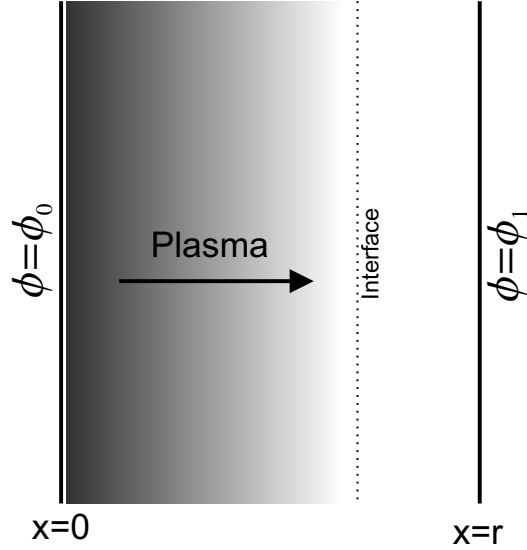


Figure 2.1: The region upon which the complete plasma sheath equation is solved. The Dirichlet voltage conditions $\phi(0) = \phi_0$ and $\phi(r) = \phi_1$ are applied at the region boundaries. Since ions are positively charged, $\phi_0 > \phi_1$.

Boltzmann distribution ([18]),

$$f(T, \epsilon) = N_0 e^{\frac{-\epsilon}{kT}}, \quad (2.2)$$

to describe the electron number density within the plasma. The Maxwell-Boltzmann distribution² function $f(T, \epsilon)$ gives the mean number of particles in a state of energy ϵ for a system of particles at absolute temperature T (k

²This distribution is applicable when the particles are completely distinguishable from one another. This in the absence of quantum effects which become prevalent when the particle density is such that the mean distance between the particles is of the order of their De Broglie wavelength. When quantum effects become important, their number distribution for a given energy depends upon whether the particles are bosons (Bose-Einstein distribution with integer spin quanta) whose wave-functions can superpose, or fermions (Fermi-Dirac distribution with half integer spin quanta) whose wave-functions cannot superpose.

being the Boltzmann constant). This is the most likely number of particles with that energy and that temperature, and is determined by analysing the number of ways of arranging particles in a particular state within the system, and choosing the state with the greatest number of arrangements possible (and hence the most likely state). Setting

$$\begin{aligned} N_e(T, \epsilon) &= f(T, \epsilon(\phi)) \\ &= N_0 e^{\frac{q\phi}{kT}} \end{aligned} \tag{2.3}$$

from (2.2), where $\epsilon(\phi) = -q\phi$, and where N_0 is the total number of electrons within the plasma, gives an expression for the electron number density as a function of voltage in the Poisson equation (2.1).

If we assume that ions are created (atoms are ionised) throughout the expanding plasma (an assumption that would be valid for a discharge ion source), an expression for the total ion number density at a given position x within the region can be determined from the ion number density per unit length $n(x)$ at that position. This is related to an ion generation rate per unit volume $G(x)$ at x by the relationship (in one dimension)

$$n(x) = \frac{G(x)}{v(x)},$$

where $v(x)$ is the ion speed at x . The total ion number density $N_i(x)$ at x can then be written

$$N_i(x) = \int_0^x \frac{G(z)}{v(z)} dz, \tag{2.4}$$

with the ion speed at z being determined by conserving energy from

$$\frac{1}{2}mv(z)^2 = q(\phi(z) - \phi(x)), \tag{2.5}$$

where $\phi(z)$ is the voltage (potential energy per unit charge at z) and m is the ion mass; rearranging (2.5) gives the ion speed

$$v(z) = \sqrt{\frac{2q}{m}} (\phi(z) - \phi(x))^{\frac{1}{2}}. \quad (2.6)$$

Substituting (2.3), (2.4), and (2.6) into (2.1) gives the complete plasma sheath equation

$$\frac{d^2\phi}{dx^2} = -\frac{q}{\varepsilon_0} \left\{ \left(\frac{m}{2q}\right)^{\frac{1}{2}} \int_0^x \frac{G(z)}{[\phi(z) - \phi(x)]^{\frac{1}{2}}} dz - n_0 e^{\frac{q\phi(x)}{kT}} \right\}. \quad (2.7)$$

This equation describes the voltage profile, $\phi(x)$, within a plasma in addition to the ion and electron number densities as a consequence of the applied electric field. The interface between the plasma and vacuum region (Figure 2.1) is determined as the location where the electron number density, (2.3), is less than some given parameter δ , where $\delta \ll N_0$. At this location, effectively all electrons have been repelled by the external electric field (this point is not distinct as the electron number density decays to zero exponentially as the voltage decreases with the dependent variable x). Beyond the plasma-vacuum interface, no further ions are generated and the integral in (2.7) becomes

$$\begin{aligned} \int_0^x \frac{G(z)}{[\phi(z) - \phi(x)]^{\frac{1}{2}}} dz &= \int_0^s \frac{G(z)}{[\phi(z) - \phi(s)]^{\frac{1}{2}}} dz + \int_s^x \frac{G(z)}{[\phi(z) - \phi(x)]^{\frac{1}{2}}} dz \\ &= \int_0^s \frac{G(z)}{[\phi(z) - \phi(s)]^{\frac{1}{2}}} dz \\ &= C, \end{aligned}$$

where C is a constant depending on the position s of the interface. Additionally, since the electron number density in the region beyond the interface

is effectively zero (that is, less than δ), the incorrect implication is that the ion charge density outside the plasma is constant. Furthermore, Tonks and Langmuir sought to model a discharge ion source where ions are generated throughout the plasma region. The ionisation region is localised in modern neutron tube designs and so such a model is inappropriate. We therefore conclude that (2.7) is not adequate for the problem at hand. To correctly describe the ion *beam* behaviour after ions have been stripped away from the plasma surface, a different model of the ion density in this region must be employed, and this is most readily achieved using the equations of motion for the ions as they are accelerated by the external electric field.

2.2 Internal Model

The internal model, [11], investigates the one-dimensional expansion of a plasma within the region $x \in (-\infty, 0]$ with the applied Dirichlet conditions $\phi(-\infty) = 0$ and $\phi(0) = \phi_0$, where $\phi(x)$ is the voltage at x , as before. In order to describe the voltage distribution within this region, the same form of the Maxwell equation (2.1) used by Tonks and Langmuir is employed. However, instead of modelling the generation of ions throughout the plasma, it is assumed that ions are generated only at the left hand end of the region (at $x = -\infty$) and their number density is calculated from their speed at x , $v(x)$. It is noted here, that whilst $\phi(0) = \phi_0$ and $v(-\infty) = v_0$ seems contradictory, it is the notation used in the original paper.

Equating the ion kinetic and potential energy (from the applied electric

field) at x we have

$$\begin{aligned}\frac{m}{2}(v(x)^2 - v_0^2) &= -q(\phi(x) - \phi(-\infty)) \\ &= -q\phi(x),\end{aligned}$$

or

$$v(x) = \sqrt{v_0^2 - \frac{2q}{m}\phi}, \quad (2.8)$$

where m , q and $v(x)$ are as previously defined, and where $v_0 = v(-\infty)$.

Denoting $N_i(x)$ as the ion number density, as above, then the ion flux $\Gamma(x)$ at x is given by³

$$\Gamma(x) = N_i(x)v(x).$$

In a steady state of ion flow⁴

$$\frac{d\Gamma}{dx} = 0,$$

which implies that Γ is independent of x , or that

$$\begin{aligned}\Gamma(x) &= N_0v_0 \\ &= \text{const},\end{aligned} \quad (2.9)$$

where $N_0 = N_i(-\infty)$. This gives the expression

$$N_i(x) = \frac{N_0v_0}{v(x)}, \quad (2.10)$$

from (2.8) and (2.9) for the ion number density. Since ions are created by ionising neutral atoms, then by conserving charge we can also say that $N_e(-\infty) = N_0$. By assuming the Maxwell-Boltzmann distribution (2.2) for

³The one-dimensional definition of flux density.

⁴From the continuity equation $\nabla \cdot \mathbf{\Gamma} = -\frac{\partial N_i}{\partial t}$, where the time derivative is zero.

the electron number density (with $N_e(T, \phi) = f(T, \epsilon(\phi))$ as previously defined), the Poisson equation, (2.1), can be written

$$\frac{d^2\phi}{dx^2} = \frac{N_0q}{\epsilon_0} \left\{ e^{\left(\frac{q\phi}{kT}\right)} - v_0 \left(v_0^2 - \frac{2q}{m}\phi \right)^{-\frac{1}{2}} \right\}, \quad (2.11)$$

from (2.2) and (2.10). Furthermore, by defining the dimensionless parameters

$$\begin{aligned} \alpha &= \frac{mv_0^2}{2kT}, \\ \psi &= \frac{q\phi}{kT}, \\ \text{and} \quad z &= \frac{x}{\lambda_D}, \end{aligned}$$

where

$$\lambda_D = \sqrt{\frac{\epsilon_0 kT}{q^2 N_0}}$$

is the Debye shielding length ([41], [32]), (2.11) can be re-written in the scale invariant form

$$\frac{d^2\psi}{dz^2} = e^\psi - \left(1 - \frac{\psi}{\alpha} \right)^{-\frac{1}{2}}. \quad (2.12)$$

Solutions to (2.12) were calculated for a typical neutron tube application. These solutions gave a good indication of the location of the plasma boundary based upon the electron number density and the calculated self-consistent accelerating potential. Results from this model indicate that ions within the plasma are shielded from the external accelerating field by the presence of neutralising electrons. The shielding shows that within the plasma region, ion trajectories are completely unaffected by the external field, and only when the electron number density begins to drop within the thin plasma sheath region do the ions begin to *feel* the external field. This leads to the concept (as it was termed) of the plasma “freezing in” the ion trajectories

due to its self-shielding effect, or that the plasma and acceleration regions are effectively uncoupled except for the very thin plasma sheath region.

This model leads nicely on to the present work, where we assume that the plasma and acceleration regions are uncoupled.

2.3 Current Model

A representative neutron tube acceleration region is shown in Figure 2.2, with the ion source located at the bottom and the target at the top (both in black). The plasma boundary (marked) is situated immediately above the aperture in the ion source plasma cup. A representation of the ion beam is shown by the two curved lines separating the zero charge density and non-zero charge density regions, stretching from the ion source cup to the target. The insulators provide resistance to gas permeation, in addition to holding off the voltage between the source and target electrodes; they have a different dielectric permittivity to the vacuum they enclose.

This schematic is representative of either a two-dimensional planar region, or as a cross-section through a three-dimensional axially symmetric arrangement. In both cases, a vertical line of symmetry (marked) separates identical parts of the region on either side of it. In the axially symmetric case, the vertical line represents an axis of rotational symmetry thereby reducing the dimension of the problem (since only axial and radial coordinates need be represented); in the planar case, the vertical line mirrors the solution on either side of it. With this in mind, if it is assumed that the tube insulators are a sufficient distance away⁵, then depending upon the numerical

⁵By sufficient distance, we mean far enough away that they do not have any influence

algorithm chosen, it is only the evacuated region (zero and non-zero charge density) immediately above the plasma boundary that need be modelled in order to fully determine the ion beam voltage and velocity distributions. The ion beam profile and consequent boundaries forming the edge of the ion beam should naturally emerge as part of the solution. By observing the vertical

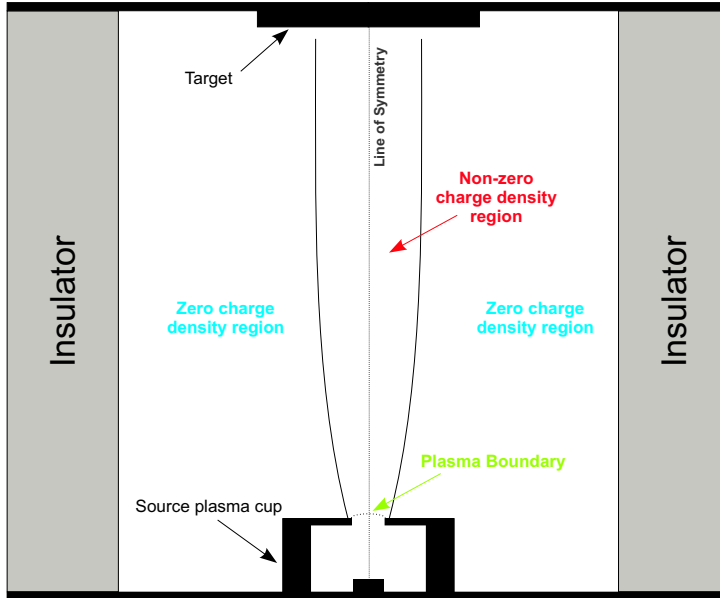


Figure 2.2: Tube schematic showing the ion beam (marked 'non-zero charge density region'), the charge free region (marked 'zero charge density region'), and the plasma boundary situated directly above the source aperture.

line of symmetry at the centre of the ion beam, the region of interest shown in Figure 2.2 can be represented as Figure 2.3 (this will be referred to in the ensuing formulation), where the region boundary is split into seven distinct sections; these are labelled $\{S_i\}$.

on the electric fields in the vicinity of the ion beam.

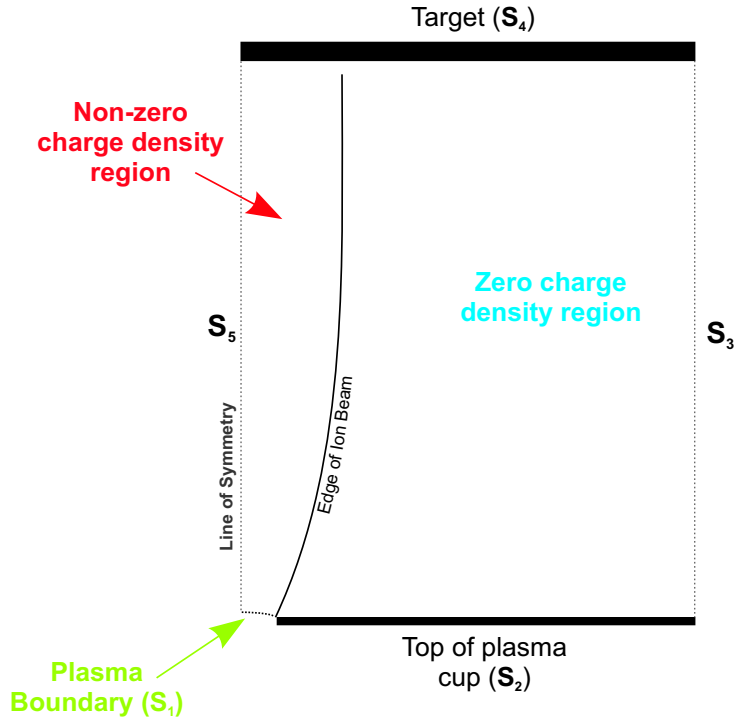


Figure 2.3: Region of interest, R . The curved line is a representation of the edge of the ion beam, and separates the zero and non-zero charge density regions.

2.3.1 Field Equations

The following set of equations describe the ion beam and voltage profile in the evacuated region shown in Figure 2.3. As described, due to the nature of the problem, the system is dynamic with the flow of charged particles being governed by the current density at the plasma boundary and by the applied potential difference (the shape of the plasma boundary itself also being dynamic); consequently, the electric field within the region is also dynamic. Therefore, the set of equations describing the problem is initially time-dependent, later becoming time-independent upon settling to the equilibrium state.

2.3.1.1 Time-dependent, Unsteady Equations

The full set of equations describing the problem in the time-dependent regime are

$$m \left\{ (\mathbf{v} \cdot \nabla) \mathbf{v} + \frac{\partial \mathbf{v}}{\partial t} \right\} = q (\mathbf{E} + \mathbf{v} \times \mathbf{B}), \quad (2.13a)$$

$$\nabla \cdot (\rho \mathbf{v}) = -\frac{\partial \rho}{\partial t}, \quad (2.13b)$$

$$\nabla \cdot \mathbf{E} = \frac{\rho}{\varepsilon_0}, \quad (2.13c)$$

$$\nabla \cdot \mathbf{B} = 0, \quad (2.13d)$$

$$\mathbf{E} = -\nabla \phi - \frac{\partial \mathbf{A}}{\partial t}, \quad (2.13e)$$

$$\text{and, } \mathbf{B} = \nabla \times \mathbf{A}. \quad (2.13f)$$

Here the constants m and q are the ion mass and charge respectively (as in Tonks and Langmuir [2], and in the internal model [11]), the vector $\mathbf{v}(\mathbf{x}, t)$ is the velocity vector field generated by the passage of particles across the region under consideration (\mathbf{x} represents the vector of linearly independent coordinates appropriate for a given coordinate system), and the scalar field $\phi(\mathbf{x}, t)$ is the voltage within the region (as above). The quantity $\rho(\mathbf{x}, t)$ is the scalar charge density field arising from the presence of charged particles within the solution region, $\mathbf{B}(\mathbf{x}, t)$ is the magnetic field within the region (which can be applied directly or induced by the flow of charged particles), and $\mathbf{A}(\mathbf{x}, t)$ is the magnetic vector potential defined by (2.13f).

Equation (2.13a), termed the Lorentz force equation, is the balance of particle inertia (on the left hand side) and particle accelerating force (on the right hand side). The time-dependent velocity component arises from

Newton's second law of motion, namely

$$\mathbf{F} = m\mathbf{a} = m\frac{d\mathbf{v}}{dt}, \quad (2.14)$$

(where \mathbf{F} is force and \mathbf{a} the particle acceleration due to that force) and since $d\mathbf{v}/dt$ is the total derivative of the velocity field, we can write using the chain rule

$$\frac{d\mathbf{v}}{dt} = (\mathbf{v} \cdot \nabla)\mathbf{v} + \frac{\partial\mathbf{v}}{\partial t}, \quad (2.15)$$

so that (2.14) and (2.15) give rise to (2.13a).

Equation (2.13b) represents conservation of charge and is a continuity equation indicating that the rate of change of charge density within a region is equal to the divergence of the current density from that region, where the current density $\mathbf{J}(\mathbf{x}, t)$ is defined by

$$\mathbf{J} = \rho\mathbf{v}. \quad (2.16)$$

Clearly if there is no net current density divergence from the region (no net charge flow from the region), then the charge density will remain constant within the region.

Equation (2.13c) is Gauss' Law and is the equivalent of (2.1) expressed in more than one dimension. It arises because sources of electrical charge can be mono-polar, and therefore give rise to a diverging electric field from a region enclosing them.

Equation (2.13d) arises from the fact that magnetic monopoles do not exist in nature, and hence there can be no net magnetic field divergence from a region. Therefore the magnetic field cannot consist of a scalar potential component, and can only be written in terms of the curl of a vector field as given by (2.13f). The link between the electric and magnetic fields is present

in the general electric field definition (2.13e).

All the variables within the equations (2.13) above are time-dependent, since all fields and scalar quantities within the neutron tube acceleration region are time-dependent until an equilibrium state is reached. If the system is allowed to settle to such an equilibrium state (by applying constant drive conditions), it is considered steady, where no fields or scalar quantities change with time at any location within the region.

2.3.1.2 Magnetic Field Influence

At this point, the system of equations can be simplified by making the assumption that magnetic field effects are negligible. External magnetic fields are not applied to the neutron tube, and magnetic fields induced by the charged particle flow are small in comparison to the applied electric field. This is a known fact in the neutron generator community and is a consequence of the relatively low ion currents within the neutron tube; it is born out of extensive experimental experience and is justified to some extent, mathematically, in Appendix B.

2.3.1.3 Simplified Time-dependent and Steady-state Systems

By removing magnetic field effects, the full system of equations, (2.13), can be restated as

$$m \left\{ (\mathbf{v} \cdot \nabla) \mathbf{v} + \frac{\partial \mathbf{v}}{\partial t} \right\} = q \mathbf{E}, \quad (2.17a)$$

$$\nabla \cdot (\rho \mathbf{v}) = -\frac{\partial \rho}{\partial t}, \quad (2.17b)$$

$$\nabla \cdot \nabla \phi = -\frac{\rho}{\varepsilon_0}, \quad (2.17c)$$

where in (2.17c), the electric field has been written as a conservative field (from (B.16) in Appendix B) with the definition

$$\mathbf{E} = -\nabla \phi, \quad (2.18)$$

for the electric scalar potential ϕ . This system of time-dependent equations can be further reduced, in the steady-state case, by immediately setting the time derivatives in (2.17a) and (2.17b) to zero, giving

$$m(\mathbf{v} \cdot \nabla) \mathbf{v} = -q \nabla \phi, \quad (2.19a)$$

$$\nabla \cdot (\rho \mathbf{v}) = 0, \quad (2.19b)$$

$$\nabla \cdot \nabla \phi = \frac{-\rho}{\varepsilon_0}. \quad (2.19c)$$

In this case, the variables $\phi(\mathbf{x})$, $\rho(\mathbf{x})$, and $\mathbf{v}(\mathbf{x})$ are now the time-independent variables to be found.

From a physical point of view, when in a steady-state, the ion current flowing across the tube acceleration region is constant, as are the consequent charge density, velocity and electric fields (provided that the applied voltage is constant). This leads to the immediate conclusion that the time derivatives within (2.17a) and (2.17b) are zero when the system is in this equilibrium state, hence (2.19), above.

2.3.2 Solution Region and Boundary Conditions

Depending upon whether a time-dependent or steady-state solution to the plasma boundary problem is required, solutions to the equations (2.17), or (2.19) are sought on the region R , shown in Figure 2.3, with the following boundary conditions applied

$$\phi(\mathbf{x}, t) = \phi_S, \quad t \geq 0, \mathbf{x} \in S_1 \cup S_2 \quad (2.20a)$$

$$\phi(\mathbf{x}, t) = \phi_T, \quad t \geq 0, \mathbf{x} \in S_4 \quad (2.20b)$$

$$\nabla\phi(\mathbf{x}, t) \cdot \mathbf{n}_1 = 0, \quad t > 0, \mathbf{x} \in S_1 \quad (2.20c)$$

$$\nabla\phi(\mathbf{x}, t) \cdot \mathbf{n}_5 = 0, \quad t > 0, \mathbf{x} \in S_5 \quad (2.20d)$$

$$\rho = \rho_s(\mathbf{x}, t), \quad t \geq 0, \mathbf{x} \in S_1 \quad (2.20e)$$

$$\rho = 0, \quad t \geq 0, \mathbf{x} \in S_2, \quad (2.20f)$$

$$\rho = 0, \quad t = 0, \mathbf{x} \in R, \mathbf{x} \notin S_1 \cup S_2, \quad (2.20g)$$

$$\nabla\rho(\mathbf{x}, t) \cdot \mathbf{n}_5 = 0, \quad t > 0, \mathbf{x} \in S_5 \quad (2.20h)$$

$$\mathbf{v} = v_i(\mathbf{x})\mathbf{n}_1, \quad t \geq 0, \mathbf{x} \in S_1 \quad (2.20i)$$

$$\mathbf{v} = 0, \quad t = 0, \mathbf{x} \in R, \mathbf{x} \notin S_1 \quad (2.20j)$$

$$\mathbf{v} \cdot \mathbf{n}_5 = 0, \quad t > 0, \mathbf{x} \in S_5 \quad (2.20k)$$

where $\{S_i\}$ are the boundary segments enclosing R (shown in Figure 2.3).

The potentials ϕ_S and ϕ_T in (2.20a) and (2.20b) are the constant applied source and target voltages, respectively. The condition (2.20c) states that the electric field (given by (2.18)) normal to the plasma boundary (S_1) is zero (\mathbf{n}_1 being the vector normal to S_1), and furthermore, since (2.20a) applies there, the electric field tangential to the boundary is also zero, or $\nabla\phi(\mathbf{x}, t) \cdot \mathbf{s}_1 = 0$ (where \mathbf{s}_1 is the vector tangential to S_1); this implies that $\nabla\phi = \mathbf{0}$ on S_1 . The

condition (2.20d) is applied to the line of symmetry, S_5 , and indicates that there is no change in potential across this boundary, whilst the additional condition (2.20c) on segment S_1 is required to determine the position of the plasma boundary, from which charged particles are emitted ([8]).

Conditions (2.20e) and (2.20i) refer to the known charge density distribution, ρ_s , of ions at the emission boundary and the known velocity magnitude, v_i , of the ions as they leave it (which is usually assumed to be constant in time). Ions emerge from the plasma boundary with a known kinetic energy, and it is assumed that they are emitted in a direction that is normal to the boundary surface, hence the presence of the unit normal vector \mathbf{n}_1 in (2.20i). The condition (2.20f) states that there is no charge on the top of the plasma cup⁶, with (2.20g) and (2.20j) stating that the starting condition (for the time dependent problem) is a region without charge or velocity anywhere, except on those boundaries indicated.

The final two conditions, (2.20h) and (2.20k), are applied to the line of symmetry, S_5 , and indicate that there is no change in charge density across, or that there is no velocity into the boundary, S_5 . The remaining segment does not have conditions applied.

2.3.2.1 Overriding Problems

The two overriding intrinsic problems with the model constructed here are firstly that from both the unsteady and steady systems of equations, it is clear the problem is non-linear in nature, and secondly that it is a moving (or free) boundary problem (we do not know the region upon which the problem is

⁶In reality this is a fixed metal boundary held at the specific electric potential ϕ_S .

to be solved in advance). Therefore, to understand the problem fully, the one-dimensional steady-state and time-dependent solutions are thoroughly studied, prior to examining a two-dimensional approach. As we shall see, the one-dimensional steady-state solution in planar geometry is analytically soluble, with the one-dimensional time-dependent case being at least partially, analytically soluble. Furthermore, studying numerical methods in one dimension allows us to check the validity and applicability of methods that might be applied to the two-dimensional case.

Chapter 3

The One-dimensional Time-independent Solution

The steady-state problem detailed in Chapter 2 can be restated in one dimension. We now explore the steady-state one-dimensional case thoroughly with an view to gaining some insight into the one and two-dimensional time-dependent cases. As mentioned in §2.3.2, and as we shall see, the one-dimensional time-independent free boundary problem in planar geometry is analytically soluble. The solution to this problem is first derived, and compared with that given by a rapid numerical method before being restated in radial geometry, giving rise to a non-linear ordinary differential equation for which no closed solution appears to exist. The radial problem is then solved by modifying the numerical method used in the planar case (taking account of subtleties particular to the radial case), and solutions to this problem explored.

In the following chapter, the full one-dimensional time-dependent solution is examined and two different numerical approaches to this problem

described, along with numerical results.

3.1 One-Dimensional Planar Time-independent Analytic Solution

The equations, (2.19), can be written in an equivalent one-dimensional planar form as

$$mv \frac{dv}{dx} = -q \frac{d\phi}{dx}, \quad (3.1a)$$

$$\frac{d}{dx}(\rho v) = 0, \quad (3.1b)$$

$$\frac{d^2\phi}{dx^2} = -\frac{\rho}{\varepsilon_0}, \quad (3.1c)$$

where (3.1a) is simply the x component of the vector equation (2.19a), and m , q , and ε_0 are constants (as before). Here, what is now, the x direction was previously the vertical (y) direction.

Intuitively, the continuity equation (3.1b) must be satisfied, since in one dimension, particles entering the solution region will always leave it (in more than one dimension this is not necessarily true due to the possible presence of magnetic fields causing vorticity within the charged particle beam). More importantly, (3.1b) implies that the quantity ρv is constant at all points within the one-dimensional region¹. By integrating (3.1b) and setting the constant of integration to be J_0 (the known initial current density) we have

$$\rho(x) = \frac{J_0}{v(x)}, \quad (3.2)$$

¹This must be so or *pockets* of local charge compression or rarefaction would unphysically form within the region.

or simply the one-dimensional equivalent definition of (2.16).

The plasma boundary problem detailed in §2.3 is therefore reduced to the simultaneous solution for $\phi(x)$ (the one-dimensional electric scalar potential or voltage) and $v(x)$ (the scalar particle velocity) of (3.1a) and (3.1c), and is considered on the domain $x \in [s, x_T]$ (shown in Figure 3.1) subject to the conditions

$$\phi = \phi_T, \quad x = x_T, \quad (3.3a)$$

$$\phi = \phi_S, \quad x = s, \quad (3.3b)$$

$$\frac{d\phi}{dx} = 0, \quad x = s, \quad (3.3c)$$

$$v = v_i, \quad x = s, \quad (3.3d)$$

where s is the location of the plasma free boundary. It should be pointed out here, that to accelerate a positively charged particle (such as a deuteron) away from the plasma boundary at s , then $\phi_S > \phi_T$.

To solve the system, (3.1), we begin by writing (3.1a) as

$$\frac{m}{2} \frac{d}{dx} (v(x)^2) = -q \frac{d\phi}{dx},$$

which can be immediately integrated to give

$$v(x)^2 = -\frac{2q}{m} \phi(x) + c_1, \quad (3.4)$$

where c_1 is a constant of integration. When $x = s$, $\phi = \phi_S$ and $v(s) = v_i$ (the initial velocity of an emerging ion determined from the plasma ion temperature) from (3.3b) and (3.3d), so that the constant c_1 is given by

$$c_1 = v_i^2 + \frac{2q}{m} \phi_S$$

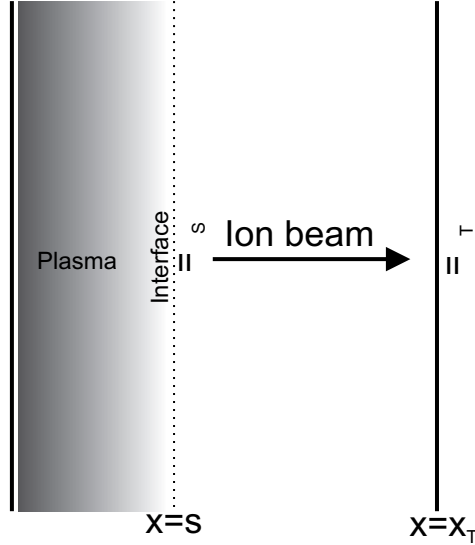


Figure 3.1: The one-dimensional planar solution region showing the passage of the steady ion beam from the (settled) plasma boundary at $x = s$ to the fixed target location at $x = x_T$. Plasma expands from some location to the left of the plasma boundary and is accelerated away from the boundary by the electric field arising from the applied potential difference. The lines $x = s$ and $x = x_T$ correspond to the boundaries S_1 and S_6 , respectively, in Figure 2.3.

from (3.4).

The scalar particle velocity $v(x)$ can then be written

$$v(x) = \sqrt{\frac{2q}{m}(\phi_S - \phi(x)) + v_i^2}, \quad (3.5)$$

since $v(x) > 0$ is consistent with particles travelling in the positive x direction, which follows as $\phi_S > \phi_T$. Upon substituting (3.5) (along with (3.2)) into (3.1c) we have the single ordinary differential equation

$$\frac{d^2\phi}{dx^2} = -\frac{J_0}{\varepsilon_0} \left(\frac{2q}{m}(\phi_S - \phi(x)) + v_i^2 \right)^{-\frac{1}{2}}, \quad (3.6)$$

holding for $s < x < x_T$ and subject to the boundary conditions (3.3a), (3.3b),

and (3.3c). It is noted here that ϕ and $\frac{d\phi}{dx}$ must be continuous on the interval $[s, x_T]$, whilst $\frac{d^2\phi}{dx^2}$ must be continuous on the interval (s, x_T) .

3.1.1 One-dimensional Planar Canonical Form

In order to expose the underlying features of the one-dimensional problem, we now restate it in a simplified dimensionless canonical form, from which integration to give an analytic solution is relatively simple.

Dividing the term in brackets on the right-hand side of (3.6) through by v_i^2 gives

$$\frac{d^2\phi}{dx^2} = -\frac{J_0}{\varepsilon_0 v_i} \left(\frac{2q}{m v_i^2} (\phi_S - \phi(x)) + 1 \right)^{-\frac{1}{2}}, \quad (3.7)$$

so that the dimensionless variable

$$\begin{aligned} w(x) &= \frac{2q}{m v_i^2} (\phi_S - \phi(x)) + 1, \\ &= v^2(x)/v_i^2 \\ &> 0, \end{aligned} \quad (3.8)$$

from (3.5), is the ratio of a particle's kinetic energy at x to its initial kinetic energy. It readily follows from (3.7) that w satisfies

$$\frac{d^2w}{dx^2} = \beta^2 w^{-\frac{1}{2}}, \quad (3.9)$$

(here it is assumed that $w^{\frac{1}{2}} = +\sqrt{w}$) where the constant,

$$\beta = \sqrt{\frac{2qJ_0}{m\varepsilon_0 v_i^3}},$$

must have units of length, L . By defining $y = \beta x$ and determining the necessary derivatives with respect to y , (3.9) can be further reduced to

$$\frac{d^2\hat{w}}{dy^2} = \hat{w}^{-\frac{1}{2}}, \quad (3.10)$$

which is the dimensionless canonical form of (3.6), where

$$\hat{w}(y) = w(y/\beta) = w(x).$$

At this point, from (3.10), it is clear that $\hat{w}''(y) > 0$, since

$$\begin{aligned} w^{1/2}(x) &= v(x)/v_i \\ &> 0, \end{aligned}$$

from (3.8), and since $v(x)$ must be positive for particles to travel in the correct direction.

3.1.1.1 Dimensionless Boundary Conditions

In order to solve the boundary value problem for (3.10), the original boundary conditions (3.3a), (3.3b) and (3.3c) must also be restated in a dimensionless form; this is done as follows. From the definition for \hat{w} (or w) and the conditions (3.3a) and (3.3b), we can say

$$\begin{aligned} \hat{w}|_{y=y_T} &= w(\phi(x_T)) \\ &= \frac{2q}{mv_i^2}(\phi_S - \phi_T) + 1 \\ &= k_0, \end{aligned} \tag{3.11}$$

say, where $y_T = \beta x_T$. Clearly, $k_0 > 0$ (since $\phi_S > \phi_T$) and typically has a numerical value of the order 10^3 for the deuterium ions accelerated in this application.

Defining $\eta = \beta s$ consistently with the transformation from x to y , the re-

maining boundary conditions become

$$\begin{aligned}\hat{w}|_{y=\eta} &= w(\phi(s)) \\ &= 1,\end{aligned}\tag{3.12}$$

from (3.3b) and (3.8), and

$$\begin{aligned}\left.\frac{d\hat{w}}{dy}\right|_{y=\eta} &= \beta^{-1}w'(s) \\ &= -\beta^{-1}\frac{2q}{mv_i^2}\phi'(s) \\ &= 0,\end{aligned}\tag{3.13}$$

from (3.3c) and (3.8). Similarly, as in (3.6), \hat{w} and $\frac{d\hat{w}}{dy}$ must be continuous on the interval $[y_T, \eta]$, whilst $\frac{d^2\hat{w}}{dy^2}$ must be continuous on the interval (y_T, η) .

3.1.2 Integration of the Planar Canonical Form

The integration of (3.10) is easily performed by multiplying both sides of (3.10) by $2\frac{d\hat{w}}{dy}$ giving

$$2\frac{d\hat{w}}{dy}\frac{d^2\hat{w}}{dy^2} = 2\frac{d\hat{w}}{dy}\hat{w}^{-\frac{1}{2}},$$

or

$$\frac{d}{dy}\left(\frac{d\hat{w}}{dy}\right)^2 = 4\frac{d}{dy}\left(\hat{w}^{\frac{1}{2}}\right).\tag{3.14}$$

Integrating (3.14) we have

$$\frac{d\hat{w}}{dy} = +\sqrt{4\hat{w}^{\frac{1}{2}} + c_2},\tag{3.15}$$

where c_2 is a constant of integration. The positive square root is taken due to the following argument. Since it has already been established that $\hat{w}''(y) > 0$, then $\hat{w}'(y)$ is an increasing function of y for $y > \eta$. Moreover, since $\hat{w}'(\eta) = 0$, from (3.13), we conclude that $\hat{w}'(y) > 0$ for $y > \eta$.

Rearranging (3.15) at $y = \eta$ and using the dimensionless conditions (3.12) and (3.13), we see at once that $c_2 = -4$ and therefore

$$\frac{d\hat{w}}{dy} = 2\sqrt{\hat{w}^{\frac{1}{2}} - 1}. \quad (3.16)$$

If we now set

$$\mathbf{w}^2 = \hat{w}^{\frac{1}{2}} - 1, \quad (3.17)$$

then

$$\frac{d\hat{w}}{d\mathbf{w}} = 4\mathbf{w}(\mathbf{w}^2 + 1), \quad (3.18)$$

and since

$$\frac{d\hat{w}}{dy} = \frac{d\hat{w}}{d\mathbf{w}} \frac{d\mathbf{w}}{dy},$$

then

$$2(\mathbf{w}^2 + 1) \frac{d\mathbf{w}}{dy} = 1 \quad (3.19)$$

from (3.16) and (3.18). Integrating both sides of (3.19) gives the complete analytic solution of (3.10) subject to (3.11), (3.12) and (3.13) in terms of the variables \mathbf{w} and y in the implicit form

$$y = 2 \left(\frac{1}{3}\mathbf{w}^3 + \mathbf{w} + c_3 \right), \quad (3.20)$$

where c_3 is given by

$$c_3 = \frac{1}{2}y_T - \frac{1}{3} \left(k_0^{\frac{1}{2}} - 1 \right)^{\frac{3}{2}} - \left(k_0^{\frac{1}{2}} - 1 \right)^{\frac{1}{2}} \quad (3.21)$$

from (3.11) and (3.17). Finally, (3.20) can be written in terms of the original variables x and ϕ (from (3.8)) therefore giving the implicit one-dimensional steady-state analytic solution of (3.6) subject to (3.3a), (3.3b) and (3.3c)

$$\begin{aligned} x(\phi) = \frac{2}{\beta} \left[\frac{1}{3} \left(\sqrt{\frac{2q}{mv_i^2}(\phi_S - \phi) + 1} - 1 \right)^{\frac{3}{2}} + \left(\sqrt{\frac{2q}{mv_i^2}(\phi_S - \phi) + 1} - 1 \right)^{\frac{1}{2}} \right. \\ \left. - \frac{1}{3} \left(k_0^{\frac{1}{2}} - 1 \right)^{\frac{3}{2}} - \left(k_0^{\frac{1}{2}} - 1 \right)^{\frac{1}{2}} \right] + x_T. \end{aligned} \quad (3.22)$$

An expression for the location of the plasma boundary s for a given set of conditions can now be determined by setting $x = s$ and consequently $\phi(s) = \phi_S$, giving

$$\begin{aligned} s &= x_T - \frac{2}{\beta} \left[\frac{1}{3} \left(k_0^{\frac{1}{2}} - 1 \right)^{\frac{3}{2}} + \left(k_0^{\frac{1}{2}} - 1 \right)^{\frac{1}{2}} \right] \\ &= \frac{2c_3}{\beta}, \end{aligned} \tag{3.23}$$

from (3.21) and (3.22).

3.1.3 Inversion of the One-dimensional Planar Solution

The implicit solution (3.22) can be written in the explicit form $\phi = \phi(x)$ by observing from (3.20) that, written in the transformed variables $y = y(\mathbf{w})$, it is the canonical cubic polynomial.

We can rewrite (3.20) as

$$\mathbf{w}^3 + 3\mathbf{w} + z = 0, \tag{3.24}$$

where

$$\mathbf{w} = \sqrt{(\hat{w}^{\frac{1}{2}} - 1)}, \quad z = 3 \left(c_3 - \frac{y}{2} \right).$$

The discriminant D for (3.24), where

$$\begin{aligned} D &= -108 - 27z^2 \\ &< 0 \quad \forall y, \end{aligned}$$

indicates that (3.24) has one real and a pair of complex conjugate roots, and since we are dealing with a physically real situation, we are concerned only with the one real root. To solve (3.24), we proceed in a manner analagous to Cardano's method (circa 1545) and choose to detail the solution, instead

of using a symbolic solver.

Equation (3.24) is similar to the identity

$$4 \sinh^3 u + 3 \sinh u = \sinh 3u, \quad (3.25)$$

and so writing $w = 2 \sinh u$ in (3.24) we obtain

$$2 (4 \sinh^3 u + 3 \sinh u) + z = 0,$$

or

$$2 \sinh 3u + z = 0,$$

from (3.25). Writing $\sinh 3u$ in exponential form we have

$$e^{3u} - e^{-3u} + z = 0,$$

or by multiplying through by e^{3u} , the quadratic

$$(e^{3u})^2 + ze^{3u} - 1 = 0.$$

Since the exponential function takes only positive values, the appropriate solution to the quadratic is

$$2e^{3u} = -z + \sqrt{(z^2 + 4)}, \quad (3.26)$$

and by writing

$$\lambda = z + \sqrt{(z^2 + 4)},$$

then

$$\begin{aligned} 2e^{3u}\lambda &= (-z + \sqrt{(z^2 + 4)})(z + \sqrt{(z^2 + 4)}) \\ &= 4, \end{aligned}$$

therefore

$$\lambda = 2e^{-3u}. \quad (3.27)$$

From (3.26) and (3.27) we conclude

$$e^u = \left(\frac{-z + \sqrt{(z^2 + 4)}}{2} \right)^{\frac{1}{3}}, \quad e^{-u} = \left(\frac{z + \sqrt{(z^2 + 4)}}{2} \right)^{\frac{1}{3}},$$

and that the inverted form of (3.24) is

$$w = e^u - e^{-u} = \left(\frac{-z + \sqrt{(z^2 + 4)}}{2} \right)^{\frac{1}{3}} - \left(\frac{z + \sqrt{(z^2 + 4)}}{2} \right)^{\frac{1}{3}}.$$

This solution for w can be written in terms of the original variables x and $\phi(x)$ as

$$\begin{aligned} \left(\frac{2q}{mv_i^2} (\phi_S - \phi(x)) + 1 \right)^{\frac{1}{2}} = 1 + \frac{1}{2^{\frac{2}{3}}} \left\{ \left(-3 \left(c_3 - \frac{\beta x}{2} \right) + \sqrt{9 \left(c_3 - \frac{\beta x}{2} \right)^2 + 4} \right)^{\frac{1}{3}} \right. \\ \left. - \left(3 \left(c_3 - \frac{\beta x}{2} \right) + \sqrt{9 \left(c_3 - \frac{\beta x}{2} \right)^2 + 4} \right)^{\frac{1}{3}} \right\}^2, \end{aligned}$$

which finally, upon squaring both sides and rearranging, gives the inverted form of (3.22) as

$$\begin{aligned} \phi(x) = \phi_S - \frac{mv_i^2}{2q} \left[\frac{1}{2^{\frac{4}{3}}} \left\{ \left(-3 \left(c_3 - \frac{\beta x}{2} \right) + \sqrt{9 \left(c_3 - \frac{\beta x}{2} \right)^2 + 4} \right)^{\frac{1}{3}} \right. \right. \\ \left. \left. - \left(3 \left(c_3 - \frac{\beta x}{2} \right) + \sqrt{9 \left(c_3 - \frac{\beta x}{2} \right)^2 + 4} \right)^{\frac{1}{3}} \right\}^4 \right. \\ \left. + 2^{\frac{1}{3}} \left\{ \left(-3 \left(c_3 - \frac{\beta x}{2} \right) + \sqrt{9 \left(c_3 - \frac{\beta x}{2} \right)^2 + 4} \right)^{\frac{1}{3}} \right. \right. \\ \left. \left. - \left(3 \left(c_3 - \frac{\beta x}{2} \right) + \sqrt{9 \left(c_3 - \frac{\beta x}{2} \right)^2 + 4} \right)^{\frac{1}{3}} \right\}^2 \right], \quad (3.28) \end{aligned}$$

where c_3 is defined by (3.21).

3.2 One-dimensional Radially Symmetric Time-independent Equation

We now consider the plasma boundary problem on the domain shown in Figure 3.2. Here ions are accelerated radially outwards from the interface at $r = s$ towards the target at $r = r_T$, and their radial speed $v(r, \theta)$, the scalar potential distribution $\phi(r, \theta)$ and the boundary location $r = s$ are determined by the boundary conditions

$$\phi = \phi_T, \quad r = r_T, \quad (3.29a)$$

$$\phi = \phi_S, \quad r = s, \quad (3.29b)$$

$$\frac{d\phi}{dr} = 0, \quad r = s, \quad (3.29c)$$

$$v = v_i, \quad r = s. \quad (3.29d)$$

As in the planar case, the potential $\phi(r)$ decreases with increasing r , or $\phi_S > \phi_T$. Since the Dirichlet boundary value ϕ_T in (3.29a) is constant on the boundary at $r = r_T$, and ϕ_S and v_i in (3.29b) and (3.29d) are also constant on the boundary at $r = s$, then the scalar potential $\phi(r, \theta)$, ion speed $v(r, \theta)$ (and consequent charge and current densities) are independent of angular position within the region and are therefore functions of radial location only (the plasma interface shape is also independent of angular location). The problem is therefore one-dimensional in r where $r \in [s, r_T]$. In the two-dimensional polar coordinate system, the gradient operator is given by

$$\nabla = \frac{\partial}{\partial r} \hat{\mathbf{p}} + \frac{1}{r} \frac{\partial}{\partial \theta} \hat{\mathbf{q}},$$

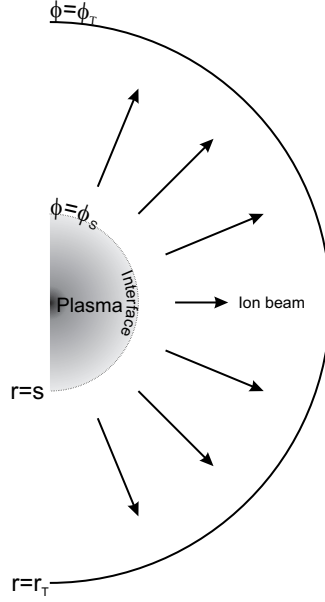


Figure 3.2: One-dimensional radial solution region. The plasma is expanding from the centre of the two concentric circles (only half of the region is shown) and the plasma boundary (marked interface) forms some radial distance away from this central point at $r = s$. The *target* is located at $r = r_T$. Since the ions are positively charged, $\phi_S > \phi_T$.

where $\hat{\mathbf{p}}$ and $\hat{\mathbf{q}}$ are the curvilinear unit vectors in the r and θ directions, the Laplacian operator is given by

$$\nabla \cdot \nabla = \frac{1}{r} \frac{\partial}{\partial r} \left(r \frac{\partial}{\partial r} \right) + \frac{1}{r^2} \frac{\partial^2}{\partial \theta^2},$$

and the divergence of a vector field \mathbf{F} , say, is given by

$$\nabla \cdot \mathbf{F} = \frac{1}{r} \frac{\partial}{\partial r} (r F_p) + \frac{1}{r} \frac{\partial F_q}{\partial \theta},$$

where F_p and F_q are the field components in the r and θ directions, respectively.

One-dimensional radial equivalents to the system (2.19) are then found to be

$$\begin{aligned}\frac{1}{r} \frac{\partial}{\partial r} \left(r \frac{\partial \phi}{\partial r} \right) + \frac{1}{r^2} \frac{\partial^2 \phi}{\partial \theta^2} &= \frac{1}{r} \frac{\partial}{\partial r} \left(r \frac{\partial \phi}{\partial r} \right) \\ &= -\frac{\rho(r)}{\varepsilon_0},\end{aligned}$$

$$\begin{aligned}m(\mathbf{v} \cdot \nabla) \mathbf{v} &= m \left\{ \left(v_p \frac{\partial v_p}{\partial r} + \frac{v_\theta}{r} \frac{\partial v_p}{\partial \theta} \right) \hat{\mathbf{p}} + \left(v_p \frac{\partial v_q}{\partial r} + \frac{v_q}{r} \frac{\partial v_q}{\partial \theta} \right) \hat{\mathbf{q}} \right\} \\ &= m v_p \frac{\partial v_p}{\partial r} \hat{\mathbf{p}} \\ &= -q \frac{\partial \phi}{\partial r} \hat{\mathbf{p}},\end{aligned}$$

and

$$\begin{aligned}\nabla \cdot (\rho \mathbf{v}) &= \frac{1}{r} \frac{\partial}{\partial r} (r \rho v_p) + \frac{1}{r} \frac{\partial \rho v_q}{\partial \theta} \\ &= \frac{1}{r} \frac{\partial}{\partial r} (r \rho v_p) \\ &= 0,\end{aligned}$$

since derivatives with respect to θ , and velocity components in the θ (or $\hat{\mathbf{q}}$) direction are zero. To clarify, the one-dimensional radial equations for the plasma free boundary problem are

$$m v \frac{dv}{dr} = -q \frac{d\phi}{dr}, \quad (3.30a)$$

$$\frac{1}{r} \frac{d}{dr} (r \rho v) = 0, \quad (3.30b)$$

$$\frac{1}{r} \frac{d}{dr} \left(r \frac{d\phi}{dr} \right) = -\frac{\rho}{\varepsilon_0}, \quad (3.30c)$$

where the subscript p , denoting the radial direction, has been dropped and the partial derivatives replaced by ordinary derivatives. Here, v , ϕ , and ρ are functions of r only. Manipulation of these equations can now proceed as in the planar case.

Integrating both sides of (3.30b) we have

$$r\rho v = c_1,$$

where c_1 is found to be

$$\begin{aligned} c_1 &= s\rho_s v_i \\ &= sJ_0, \end{aligned}$$

ρ_s being the initial charge density (at the free boundary), and J_0 the initial current density (at the free boundary) from (2.16). We can then say

$$\begin{aligned} J(r) &= \rho(r)v(r) \\ &= J_0 \frac{s}{r}, \end{aligned} \tag{3.31}$$

where the reciprocal dependence of J on r is expected for a radially expanding density.

The speed v at r of a charged particle emitted from the free boundary at s can be determined from (3.30a) in a similar manner to the planar case (see (3.5) in §3.1 above) giving

$$v(r) = \sqrt{\frac{2q}{m} (\phi_s - \phi(r)) + v_i^2}. \tag{3.32}$$

Using (3.31) and (3.32), we can now rewrite (3.30c), (3.30a), and (3.30b) as the single ordinary differential equation

$$\frac{d}{dr} \left(r \frac{d\phi}{dr} \right) = -\frac{sJ_0}{\varepsilon_0} \left(\frac{2q}{m} (\phi_s - \phi(r)) + v_i^2 \right)^{-\frac{1}{2}}, \tag{3.33}$$

where the *unknown* free boundary location s appears explicitly on the right-hand side. The solution of (3.33) subject to the boundary conditions (3.29a), (3.29b) and (3.29c) will result in a potential distribution as a function of radial distance (that is particular to the specific boundary conditions applied).

3.2.1 One-dimensional Radial Canonical Form

As in the planar case (§3.1.1), the ordinary differential equation (3.33) can be non-dimensionalised revealing a simple canonical form. Once again, dividing the term in brackets on the right-hand side of (3.33) through by v_i^2 gives

$$\frac{d}{dr} \left(r \frac{d\phi}{dr} \right) = -\frac{sJ_0}{\varepsilon_0 v_i} \left(\frac{2q}{mv_i^2} (\phi_S - \phi(r)) + 1 \right)^{-\frac{1}{2}}, \quad (3.34)$$

so that the dimensionless variable

$$\begin{aligned} \omega(r) &= \frac{2q}{mv_i^2} (\phi_S - \phi(r)) + 1, \\ &= \frac{v(r)^2}{v_i^2} \end{aligned} \quad (3.35)$$

can be defined, from (3.32). Clearly, since particles must accelerate away (in the sense of positive r) from the plasma boundary at $r = s$, then $v(r) \geq v_i$, $r \geq s$ indicating that $\omega(r)^{\frac{1}{2}} \geq 1$, $r \geq s$.

Derivatives of $\omega(r)$ are then given by

$$\frac{d\omega}{dr} = -\frac{2q}{mv_i^2} \frac{d\phi}{dr} \quad (3.36)$$

and

$$\frac{d^2\omega}{dr^2} = -\frac{2q}{mv_i^2} \frac{d^2\phi}{dr^2},$$

so that (3.34) can be written

$$-\frac{mv_i^2}{2q} \left(r \frac{d^2\omega}{dr^2} + \frac{d\omega}{dr} \right) = -\frac{sJ_0}{\varepsilon_0 v_i} \omega^{-\frac{1}{2}},$$

or

$$\frac{d}{dr} \left(r \frac{d\omega}{dr} \right) = s\beta\omega^{-\frac{1}{2}}, \quad (3.37)$$

where

$$\beta = \frac{2qJ_0}{m\varepsilon_0 v_i^3},$$

which has the dimensions of L^{-2} . We now define the new dimensionless variables Q and R by

$$\omega(r) = \beta^{\frac{1}{3}} s^{\frac{2}{3}} Q(r),$$

and

$$R = \beta^{\frac{1}{2}} r, \quad (3.38)$$

respectively. Substituting these into (3.37) gives

$$\frac{d}{dR} \left(R \frac{d\hat{Q}}{dR} \right) = \hat{Q}^{-\frac{1}{2}}, \quad (3.39)$$

the dimensionless canonical form of (3.33), where $Q(r) = Q(R/\beta^{\frac{1}{2}}) = \hat{Q}(R)$.

3.2.1.1 Radial Dimensionless Boundary Conditions

As in the planar case, we must also restate the boundary conditions in a dimensionless form. With reference to (3.35) and (3.36) we have

$$\begin{aligned} \hat{Q}(R_T) &= Q(r_T) \\ &= \beta^{-\frac{1}{3}} s^{-\frac{2}{3}} \left(\frac{2q}{mv_i^2} (\phi_S - \phi_T) + 1 \right) \\ &= \beta^{-\frac{1}{3}} s^{-\frac{2}{3}} k_0, \end{aligned} \quad (3.40)$$

say, from (3.29a) and (3.11), where $R_T = \beta^{\frac{1}{2}} r_T$;

$$\begin{aligned} \hat{Q}(R_s) &= Q(s) \\ &= \beta^{-\frac{1}{3}} s^{-\frac{2}{3}} \end{aligned}$$

from (3.29b), where $R_s = \beta^{\frac{1}{2}} s$; and

$$\begin{aligned} \left. \frac{d\hat{Q}}{dR} \right|_{R=R_s} &= \left. \frac{dQ}{d\omega} \frac{d\omega}{d\phi} \frac{d\phi}{dr} \right|_s \frac{dr}{dR} \\ &= 0, \end{aligned} \quad (3.41)$$

from (3.29c) and (3.38).

3.3 Numerical Methods for the One-dimensional Plasma Boundary Problem

There is no apparent analytic solution to (3.33) subject to the conditions (3.29a), (3.29b) and (3.29c). However, a number of numerical methods can be employed that utilise, for instance, moving mesh algorithms to iterate towards the solution of both (3.6) and (3.33) (an example is given in [34]). It is though, much more efficient to apply a relatively simple numerical method for initial value problems to these equations, than to employ a relatively complex moving mesh method. We now investigate the application of such a method to the one-dimensional, steady-state, planar problem, comparing numerical solutions to the analytic solution given in §3.1. This method is then used to study the one-dimensional, steady-state, radial problem.

3.3.1 A Numerical Method for the One-dimensional Planar Problem

Since the one-dimensional planar equation (3.6) can be integrated analytically giving the explicit solution (3.28), it would seem appropriate to develop a numerical method for this problem against which the analytic solution can be compared, before applying the method to the equivalent radial problem (3.33).

A simple and efficient way of numerically solving (3.6) can be developed by splitting its canonical form, (3.10), into a coupled pair of first order ordinary differential equations, integrating them in non-dimensional space, and then returning the solution to physical space (where some physical inter-

pretation of the solutions can be extracted). This is most easily done by setting

$$\frac{d\hat{w}}{dy} = z, \quad (3.42)$$

so that from (3.10)

$$\frac{dz}{dy} = \hat{w}^{-\frac{1}{2}}, \quad (3.43)$$

and integrating forwards with respect to y from the (source) free boundary position $\eta = \beta^{\frac{1}{2}}s$ (where s is selected in advance) with the initial conditions (3.12) and (3.13). Integration proceeds until (3.11) is satisfied, and since $\hat{w}'(y) > 0$ for $y > \eta$, the condition (3.11) can be satisfied only once over the solution region and this is at the right hand end of the region (integration proceeds with positive y from left to right). Therefore, the location of the right hand end (the target end) of the solution region is given by the value of y at the point where (3.11) is satisfied (where $y_T = \beta^{\frac{1}{2}}x_T$, say).

The differential equation (3.10) is invariant under a translation of domain and this can be simply shown by shifting the dependent variable in (3.10) by a constant, \mathbf{a} , say. Upon doing this, derivatives in (3.10) are unchanged yielding the similar one-dimensional equation

$$\frac{d^2\hat{w}_m}{d\mathbf{m}^2} = \hat{w}_m^{-\frac{1}{2}}, \quad (3.44)$$

where $\mathbf{m} = y + \mathbf{a}$, and $\hat{w}_m = \hat{w}(\mathbf{m})$. Here, the domain shift has introduced the second term on the left hand side of (3.45)

With this in mind, it is clear that an initial choice of free boundary location η leads to a unique region size ($y_T - \eta$). Once this size is known (from the method described above), the fixed target location y_T can be set, with the free boundary location at the left hand end of the region now varying with the applied boundary conditions.

3.3.1.1 Comparison Between Numerical and Analytic Solution

To test the numerical method just described, solutions to the planar plasma boundary problem were found for several different sets of boundary conditions. The MATLAB function ODE45 was used to integrate (3.42) and (3.43) with constant initial particle energy (50eV) and current density ($J_0 = 18800\text{Am}^{-2}$), typical of a neutron tube application, and with the target potential, ϕ_T , set at zero; several different source potentials (40, 60, 80 and 100 kilovolts), that are typical of those seen in a neutron tube application, were applied. It was expected that the solution region would reduce in size as the applied potential difference was reduced (see Figures 1.2, 1.3 and 1.4 and the associated text in §1.1.1), and this behaviour is clearly seen in Figure 3.3 which shows the numerical and the associated analytic solutions (calculated from (3.28)). The location of the free plasma boundary with an applied source potential of 100kV has been labelled as the *nominal plasma boundary location* to illustrate the reduction in region width with reducing source potential. The curve labelled *Plasma boundary location as a function of source-target potential difference* is calculated from (3.23).

The ODE45 function was executed with a specified relative tolerance of 1×10^{-9} . This causes the solver, at a particular point, to repeatedly generate the solution with successively reduced integration step sizes. This step size reduction process is repeated until the difference between two consecutive approximations of the solution, at that point, falls below the specified tolerance. In the planar case, this process can be checked by calculating the analytic potential solution, from (3.28), at the same integration locations as those generated in the numerical approximation; consequently the absolute RMS

difference (over the entire set of points) between the two solutions can be calculated. For the curves in Figure 3.3, calculated absolute RMS differences between numerical and analytic potential solutions range from $\sim 7.5 \times 10^{-5}$ to $\sim 1.6 \times 10^{-4}$. This gives confidence in the use of the ODE45 function so that it can be used in a numerical method for the subtly different radial problem, for which no analytic solution exists.

3.3.2 A Numerical Method for the One-dimensional Radial Problem

There are some fundamental differences between the basic physical situations in the planar and radial cases that must be taken into consideration when calculating solutions to the radial problem described in §3.2. In the planar case, one of the initial specifications for the problem is the current density J_0 at the ion source, with variations in this value giving rise to variations in the solution and solution domain size. The physically planar nature of the problem implies that the emitted ion current from the ion source is linearly proportional to the emission ion current density, where the constant of proportionality is the emission surface area, and which in the planar case, is independent of domain location. This is manifested in the differential equation (3.10), by it being invariant under a translation of domain; see (3.44) and associated text. Physically, this does not change the emitted ion current as already noted.

The situation is different in the radial case where ions emitted with a given current density from a boundary close to the origin, give rise to a lower emitted ion current than those emitted from a boundary further away from

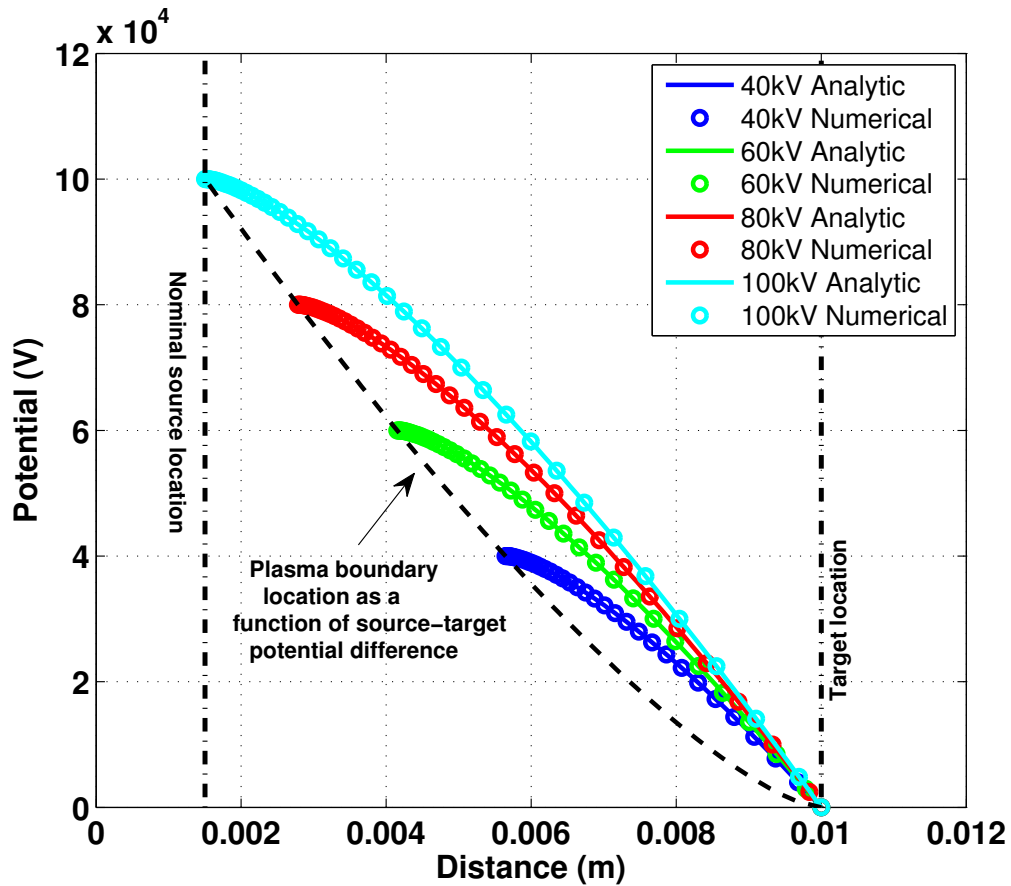


Figure 3.3: Numerical and analytic solutions to the one-dimensional planar plasma boundary problem at different applied source potentials (initial energy and current density is the same in each case). The accumulation of points towards the left of the calculated numerical solutions is caused by the error control procedure within the solver (described above).

the origin. This is due to the emission boundary area, and hence emission current for a given current density, being radially dependent and is manifested in the differential equation (3.39), by it not being invariant under a shift of domain. This can be simply shown in the same manner as in the planar case

by shifting the dependent variable in (3.39) by a constant, \mathbf{a} , say. Substituting the new variable, $\mathbf{n} = R + \mathbf{a}$, into (3.39), we deduce

$$\frac{d}{d\mathbf{n}} \left(\mathbf{n} \frac{d\hat{Q}_{\mathbf{n}}}{d\mathbf{n}} \right) - \mathbf{a} \frac{d^2\hat{Q}_{\mathbf{n}}}{d\mathbf{n}^2} = \hat{Q}_{\mathbf{n}}^{-\frac{1}{2}}, \quad (3.45)$$

where the domain shift has introduced the curvature term on the left hand side (not present in (3.39)), the effect on the solution of which, is clearly dependent upon the size of the domain shift; here $\hat{Q}_{\mathbf{n}} = \hat{Q}(\mathbf{n})$.

With this in mind, a particular domain location, size, and associated potential solution for this equation with a given emission ion current and set of initial conditions, is unique and cannot be translated (in order to fix the target location) as in the planar case, hence a slightly different solution method must be employed and this is described as follows.

To solve the radial problem described in §3.2, as in the planar case, we begin by splitting (3.39) in to a pair of first order equations by setting

$$\frac{d\hat{Q}}{dR} = \xi, \quad (3.46)$$

so that expansion of the derivative on the left-hand side of (3.39) gives

$$\frac{d\xi}{dR} = \frac{1}{R} \left(\hat{Q}^{-\frac{1}{2}} - \xi \right). \quad (3.47)$$

These can be used to calculate the single unique solution for a given set of initial conditions, by utilising the fact that $\hat{Q}(R)$ and $\hat{Q}'(R)$ are strictly increasing functions over the solution domain; this is shown in the following section.

3.3.2.1 Radial ‘Shooting’ Method

As already mentioned, the situation in the radial case is subtly different to that of the planar case as a consequence of the plasma boundary location appearing explicitly on the right hand side of the original radial equation, (3.33). This is manifested in the dimensionless equation, (3.39), by it not being invariant under a shift of domain (unlike the planar case). This means that, in order to integrate forwards from the plasma boundary (as in the planar case), the location of that boundary must be known in advance. Since this is not the case, a method for determining the boundary location, whilst simultaneously determining the solution that satisfies the boundary conditions, must be ascertained.

In other words, selecting the plasma boundary location in advance and integrating forwards from it will not necessarily yield a solution whereby the boundary condition, (3.40), is satisfied at the required, fixed target location. Since integrating from the fixed target location is not feasible (there is no gradient information known in advance at the target), we must develop a method that iterates towards the correct plasma boundary location for a given set of conditions, whereby integration towards the target from the correct plasma boundary causes the boundary condition, (3.40), and the correct target location to coincide. This is reminiscent of a *shooting* method, commonly employed to solve ordinary differential equations (see [20], for example).

To do this, we initially use a search method whereby we choose an initial plasma boundary location, R_{s_0} say, and integrate towards the target, stopping when (3.40) is satisfied. If the integration stops before the required

target location is reached, the initial plasma boundary location is incremented by the small amount, ΔR_s , and the integration repeated. This procedure stops at the i^{th} initial plasma boundary location, $R_{s_i} = R_{s_0} + (i-1)\Delta R_s$, when the chosen target location, R_T , falls within the range of calculated target locations resulting from solutions starting at $R_{s_{i-1}}$ and R_{s_i} . Once a plasma boundary location interval (containing the correct plasma boundary) that gives rise to a set of solutions, including that solution that gives rise to the correct target location for the given boundary conditions, is known, a bisection-type method is applied at the plasma boundary, with the calculated target location being used at each step to inform the starting plasma boundary location; it being adjusted accordingly.

This process is only possible if the dimensionless solution potential $\hat{Q}(R)$ monotonically increases (in a concave, upwards manner) from the known value at the plasma boundary to that at the target, or if both $\hat{Q}'(R)$ and $\hat{Q}''(R)$ are greater than zero over the domain $R \in [R_s, R_T]$. To show this, we first make the transformation $\mathbf{u} = \ln R$ (so that $\mathbf{u} \in [\mathbf{u}_s, \mathbf{u}_0]$, with $\mathbf{u}_s = \ln R_s$), and $\hat{Q}(R) = \hat{Q}(e^{\mathbf{u}}) = \hat{P}(\mathbf{u})$, so that (3.39) is reduced to

$$\hat{P}''(\mathbf{u}) = e^{\mathbf{u}} \hat{P}^{-\frac{1}{2}}. \quad (3.48)$$

Now, since $\hat{P}(\mathbf{u}) = \hat{Q}(R)$, and

$$\begin{aligned} \hat{Q}(R) &= Q(r) \\ &= \beta^{-\frac{1}{3}} s^{-\frac{2}{3}} \omega(r) \\ &> 0, \quad R \in [R_s, R_T] \end{aligned}$$

(since $\beta, s > 0$), we can conclude that

$$\begin{aligned}\hat{P}''(\mathbf{u}) &= R \frac{d}{dR} \left(R \frac{d\hat{Q}}{dR} \right) \\ &> 0,\end{aligned}\tag{3.49}$$

from (3.48). Additionally, by writing

$$\begin{aligned}\hat{P}'(\mathbf{u}) &= R\hat{Q}'(R) \\ &= \int_{\mathbf{u}_s}^{\mathbf{u}} e^{\zeta} \hat{P}^{-\frac{1}{2}}(\zeta) \, d\zeta + \hat{P}'(\mathbf{u}_s),\end{aligned}\tag{3.50}$$

we can also conclude from the mean value theorem for integrals that $\hat{P}'(\mathbf{u}) > 0$, since $\hat{P}'(\mathbf{u}_s) = 0$, from (3.41); this, in turn, implies that $\hat{Q}'(R) > 0$, $R \in [R_s, R_T]$, from (3.50).

It is now known that $\hat{Q}'(R) > 0$ over the solution domain, from (3.50), but it is not immediately obvious that $\hat{Q}''(R) > 0$, $R \in [R_s, R_T]$. It is clear that the curve $\hat{P}(\mathbf{u})$ is concave upwards, since $\hat{P}''(\mathbf{u}) > 0$, from (3.49). Also, by superimposing the R axis over the \mathbf{u} axis (but with a different scale), the graph of $\hat{P}(\mathbf{u})$ read against the R axis is simply $\hat{Q}(R)$; this must also be concave upwards as it is the same curve, merely being read against the different, strictly increasing scale, $R = e^{\mathbf{u}}$. With this in mind, the curvature must be the same sign for both $\hat{P}(\mathbf{u})$ and $\hat{Q}(R)$, where for $\hat{P}(\mathbf{u})$, it is given by

$$\begin{aligned}\varrho_P &= \frac{\hat{P}''(\mathbf{u})}{\left(1 + (\hat{P}'(\mathbf{u}))^2\right)^{\frac{3}{2}}}, \\ &> 0, \quad \mathbf{u} \in [\mathbf{u}_s, \mathbf{u}_0]\end{aligned}$$

since $\hat{P}''(\mathbf{u}) > 0$. The equivalent expression in \hat{Q} is then

$$\varrho_Q = \frac{\hat{Q}''(R)}{\left(1 + (\hat{Q}'(R))^2\right)^{\frac{3}{2}}},$$

which has the same sign as ϱ_P , implying that $\hat{Q}''(R) > 0$ (since $\hat{Q}'(R) > 0$).

Since it is the case that $\hat{Q}(R)$ curves upwards from $R = R_s$ in a concave manner, we expect that a change in initial plasma boundary location, for a given set of initial conditions, will give rise to a corresponding change (in the same direction) in calculated target location. This therefore enables the refinement process, described above, to take place.

Radial Numerical Results

As in the planar case, the MATLAB function ODE45 was used (again, with a specified relative tolerance of 1×10^{-9}) to solve the pair of equations, (3.46) and (3.47), thereby generating a potential solution for each initial plasma boundary location (as described above). The event trapping mechanism in ODE45 was used to terminate the integration when the value of the calculated (dimensionless) solution potential reached that given by (3.40). Dimensionless solutions were then transformed back to physical space for display.

In each case, the initial search procedure starts the plasma boundary location guesses with the physical location $s_0 = 0.001\text{m}$, or dimensionless location $R_{s_0} = 2.621$. The search procedure successively increments from this starting location with an incremental step size of $\Delta s = 5 \times 10^{-4}\text{m}$, or $\Delta R_s = 1.311$. This continues until a plasma boundary interval is found, in which the corresponding, calculated target interval contains the required target location; the target was set at 0.02m in all cases. Once this interval

is located, the bisection algorithm begins whereby the plasma boundary interval is successively halved (with the calculated target interval being used to inform the bisection method) until the calculated target location falls to within 10^{-7}m (or 2.6×10^{-4} dimensionless length units) of the required target location.

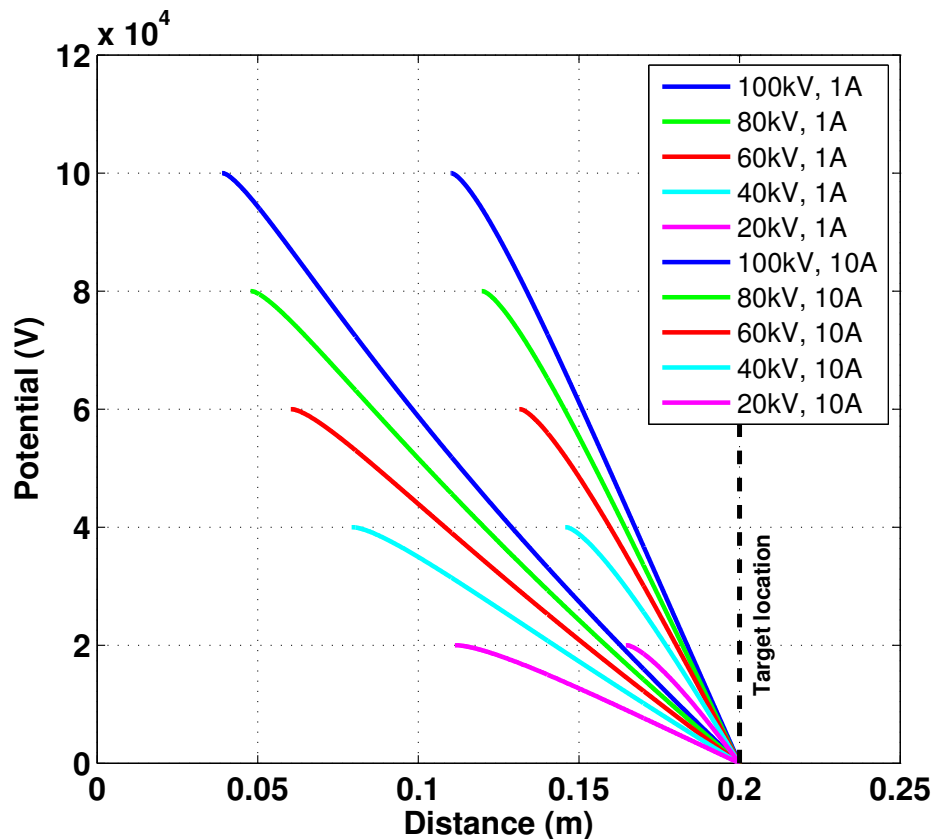


Figure 3.4: Numerical results from the radial shooting method. Curves show the variation in potential with distance away from the inner plasma free boundary (to the left) to the target (to the right). Solutions for a number of differing sets of initial conditions are shown.

Figure 3.4 shows results from two current (1 Amp and 10 Amps) régimes calculated by the radial shooting method just described. As is expected, calculated plasma boundaries within the device carrying the smaller 1 Amp ion current are located nearer the origin than those within the device carrying the larger 10 Amp ion current, for a given external electric field. This is due to the larger ion flux in the 10 Amp case causing the boundary to bulge into the accelerating region (and conversely for the smaller 1 Amp case) as described previously in §1.1.1. The effect of radial location on the solution can be clearly seen in the 1 Amp case, particularly for solutions with a (relatively) high applied potential difference. The combination of a strong electric field and relatively low ion flux causes the plasma boundary to be located near to the origin, where the circular boundary begins to resemble a point source. This is in contrast to the planar case and is manifested in the presence of s on the right-hand side of (3.33), in addition to the more complex derivative term on the left-hand side of (3.33). For certain sets of boundary conditions, these terms cause the solution curvature to change sign (from negative to positive) some distance away from the plasma boundary.

In the planar case (3.6), the electric field gradient (and hence curvature) is always less than or equal to zero, irrespective of the location of the free plasma boundary. However, in the radial case (3.33), the electric field gradient is given by

$$\frac{d^2\phi}{dr^2} = \frac{1}{r} \left(\frac{sJ_0}{\varepsilon_0 v_i} \left(\frac{2q}{mv_i^2} (\phi_S - \phi(r)) + 1 \right)^{-\frac{1}{2}} + \frac{d\phi}{dr} \right),$$

where, since $\frac{d\phi}{dr} < 0$, $r \in (s, r_T]$ (from (3.35) and (3.36)), we conclude that the solution curvature changes sign where

$$\frac{sJ_0}{\varepsilon_0 v_i} \left(\frac{2q}{mv_i^2} (\phi_S - \phi(r)) + 1 \right)^{-\frac{1}{2}} + \frac{d\phi}{dr} = 0. \quad (3.51)$$

Referring to the 100KV, 1 Amp case in Figure 3.4, the solution gradient is roughly constant, taking a value of $\sim -6.25 \times 10^5 \text{ Vm}^{-1}$. In combination with the constants

$$\begin{aligned} \frac{2q}{mv_i^2} &= \frac{1}{I_E} \\ &= 0.02 \text{ C J}^{-1}, \end{aligned}$$

and,

$$\begin{aligned} \frac{sJ_0}{\varepsilon_0 v_i} &= \frac{I_0}{\pi s \varepsilon_0 v_i} \\ &\approx 1.29 \times 10^7 \text{ C}^2(\text{Jm})^{-1}, \end{aligned}$$

where I_E is the initial particle energy in electron-volts ($I_E = 50 \text{ eV}$ in this case), the current density J_0 is calculated as the density over the circular area of the emission boundary ($J_0 = I_0/(\pi s^2) \simeq 210 \text{ Am}^{-2}$), and s is the plasma boundary location ($\sim 0.04 \text{ m}$ in this case); (3.51) indicates that the solution curvature will change sign where

$$\phi_S - \phi(r) \lesssim 21500\text{V}. \quad (3.52)$$

A simple visual inspection of the 100KV, 1 Amp trace in Figure 3.4 indicates that the solution curvature changes from sign when the solution potential is at $\sim 80000\text{V}$ (or where $\phi_S - \phi(r) \sim 20000\text{V}$), corresponding to (3.52) to a first approximation.

Chapter 4

The One-dimensional Time-dependent Solution.

4.1 Introduction to the One-dimensional Time- dependent Problem

As mentioned in §1.1.1, two distinct timescales exist during the operation of the neutron tube, and the previous chapter described (in one dimension) the stable steady state to which the system settles over the relatively long timescale. In this chapter we examine (in one dimension) the relatively short timescales involved with the passage of the charged particle beam across the tube accelerating gap, and the consequent settling of the plasma-vacuum boundary.

Prior to the creation of the deuterium plasma, a state exists within the operation of the neutron tube, where no charged particle flow takes place. In this state a stable electric field is generated by the application of the main

acceleration voltage to the tube electrodes. As the deuterium plasma is released, ions begin to accelerate across the tube accelerating gap separating the solution region into two states. In the part of the region ahead of the advancing charge front there is clearly no charge (i.e. the charge density and velocity fields are zero), but behind it the region is charge *infused*, where by charge infused, we mean that this part of the region contains charged particles, with the charge density and velocity fields being non-zero. Since two states exist within the solution region as the charge front is accelerated across it, the solution of the time-dependent (short timescale) problem can be analysed differently in these two areas. The charge free region ahead of the charge front can be analysed analytically, as we shall see, with it being effectively separated from the charge infused region by a characteristic curve of the problem. This “separation” characteristic is defined by the time-dependent location of the charge front itself. A partial time-dependent analytic solution can be also obtained for the charge infused region behind the charge front, but to obtain a full time-dependent solution both behind and ahead of the charge front, we appeal to a numerical method.

Two numerical approaches are proposed for determining the solution of the time-dependent problem, where the first numerical method, that uses a standard difference approach, required, in hindsight, a parameter to be introduced to overcome stability issues that are inherent to the method and that lead to its failure. A new, second numerical approach, was devised to overcome the difficulties experienced with the first method, and this is detailed in Section §4.3.3.

4.1.1 Fields Pertinent to the Problem

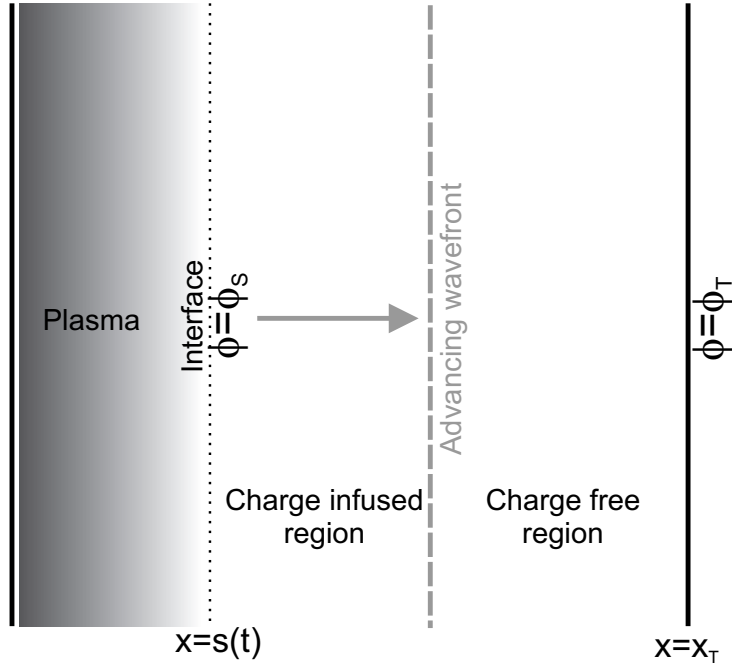


Figure 4.1: One-dimensional planar solution region showing (in the short timescale) the rapidly advancing charge wavefront. Plasma expands from some location to the left of the time-dependent plasma boundary (at $x = s(t)$) and is accelerated away from the boundary by the electric field arising from the applied potential difference. The region to the left of the wavefront has non-zero charge density, whilst that to the right has zero charge density. The target is fixed and located at $x = x_T$, as before.

At this point it is valuable to summarise the various vector and scalar fields pertinent to the time-dependent problem before restating the solution region and time-dependent system of equations in a one-dimensional form. We assumed in §2.3.1 that magnetic field effects can be ignored and so the relevant variables are as follows.

The charge density scalar field is represented by $\rho(\mathbf{x}, t)$, and represents the charge per unit volume within an enclosed region. It is related to both the current density and velocity vector fields via the definition (2.16), where the current density $\mathbf{J}(\mathbf{x}, t)$ is the time-dependent rate of flow of charge per unit cross sectional area at \mathbf{x} and the velocity $\mathbf{v}(\mathbf{x}, t)$ is the time-dependent rate and direction of movement of charge at \mathbf{x} . Finally, the electric field $\mathbf{E}(\mathbf{x}, t)$, defined by (2.18), is the time-dependent force acting on a unit of charge at \mathbf{x} .

In one dimension, all fields are spatially dependent upon only one variable, x say, and Figure (4.1) shows the one-dimensional solution region with the charge front (separating the two charge infused and charge free regions) advancing in a positive x direction, from the plasma boundary on the left at $s(t)$, to the target on the right at x_T .

4.1.2 The One-dimensional Time-dependent System

The time-dependent system, (2.17), is now restated in one spatial dimension (the spatial independent variable being x) as

$$v \frac{\partial v}{\partial x} + \frac{\partial v}{\partial t} = \frac{q}{m} E, \quad (4.1a)$$

$$\frac{\partial(\rho v)}{\partial x} = -\frac{\partial \rho}{\partial t}, \quad (4.1b)$$

$$\frac{\partial^2 \phi}{\partial x^2} = -\frac{\rho}{\epsilon_0}, \quad (4.1c)$$

in addition to the one-dimensional conservative electric field definition,

$$E = -\frac{\partial \phi}{\partial x}. \quad (4.1d)$$

The required time-dependent solution is generated by solving these equations on the region $s(t) \leq x \leq x_T$ and $t \geq 0$, in conjunction with the conditions

$$\phi(x_T, t) = \phi_T = \text{const}, \quad t \geq 0 \quad (4.2a)$$

$$\phi(s(t), t) = \phi_S = \text{const}, \quad t \geq 0 \quad (4.2b)$$

$$\frac{\partial \phi(s(t), t)}{\partial x} = 0, \quad t > 0 \quad (4.2c)$$

$$v(s(t), t) = v_i = \text{const}, \quad t \geq 0 \quad (4.2d)$$

$$v(x, 0) = 0, \quad x \in (s_0, x_T] \quad (4.2e)$$

$$\rho(s(t), t) = \rho_s(t), \quad t \geq 0 \quad (4.2f)$$

$$\rho(x, 0) = 0, \quad x \in (s_0, x_T]. \quad (4.2g)$$

Here $s(t)$ is the, as yet, undetermined time-dependent plasma boundary location with $s_0 = s(0) = 0$ (s_0 is set to zero in this chapter, but need not be so); ϕ_T , ϕ_S , and v_i are known constants with $\phi_S > \phi_T$; the function $\rho_s(t)$ is a known time-dependent function, which could take any physically realistic¹ form, but is known from experiment to be a function ramping from zero to a constant value over a relatively short period of time (being constant for the majority of the neutron tube operation time).

The advancing charge density wavefront is represented by the coupled hyperbolic equations (4.1a) and (4.1b), whilst the electric field in both charge infused and charge free regions is coupled to these equations by the elliptic equation (4.1c). The electric field, in the absence of time varying magnetic fields is defined as (4.1d), the gradient of some scalar potential ϕ , as in (2.18).

¹By physically realistic, we mean a function that can be driven by an experimental procedure; one that is not discontinuous.

4.2 Analytic Solution

By analysing the time-dependent system, (4.1), inroads can be made in to an analytic time-dependent solution. Initially, we examine the solution ahead of the advancing charge front, and follow with further analysis that gives rise to the analytic form of one variable, within the full time-dependent problem, upon characteristic curves pertinent to the hyperbolic equations, (4.1a) and (4.1b). This analysis reveals, by manipulating the original system of equations, a second order Riccati equation that can be linearised and solved yielding the explicit form of the variable $\partial v/\partial x$ upon characteristic curves spanning the solution region behind the charge front.

4.2.1 Analytic Solution Ahead of the Advancing Charge Front and Associated Separating Characteristic

As previously described, when charged particles are introduced into the accelerating region, they propagate across it in a wavelike manner, effectively partitioning the region into two areas that can be considered separately.

The part of the solution region ahead of the propagating charge front is charge free, whilst that behind it is charge infused. Within the charge infused part of the solution region, the electric field is inherently dependent upon the charge density field as a consequence of Gauss' Law, (4.1c), and is therefore time-dependent, since the charge density is time-dependent as a consequence of the conservation law (4.1b). However, ahead of the advancing wavefront the electric field is considered to be constant as a consequence of the absence of charged particles². The electric field and consequently the charge density

²Strictly, as a consequence of the infinite range of the electromagnetic field and of its

field are coupled to the velocity field via the Lorentz force equation, (4.1a).

At $t = 0$, no charge exists within the acceleration region as no particles have been introduced at this time; this is formalised with condition (4.2g). Clearly, due to the absence of charge across the acceleration region at $t = 0$, (4.1b) is automatically satisfied. Furthermore, with $\rho = 0$, (4.1c) becomes

$$\frac{\partial^2 \phi}{\partial x^2} = 0,$$

which upon integrating and applying the conditions (4.2a) and (4.2b) gives the expression

$$\phi(x, 0) = \left(\frac{\phi_S - \phi_T}{x_T - s_0} \right) (x_T - x) + \phi_T \quad (4.3)$$

for the electric scalar potential within the acceleration region at $t = 0$. Also, from the definition (4.1d) and (4.3), the electric field $E(x, 0)$ must be the constant

$$\begin{aligned} E(x, 0) &= E_0 \\ &= - \left(\frac{\phi_S - \phi_T}{x_T - s_0} \right). \end{aligned} \quad (4.4)$$

An expression for the velocity of particles emitted from the $t = 0$ boundary can now be obtained by firstly writing (4.1a) as the ordinary differential equation

$$\frac{dv}{dt} = \frac{q}{m} E, \quad (4.5)$$

where the time, t , can be measured along characteristic curves in the (x, t) plane.

speed of propagation, c (the speed of light), it is conceivable that the low density presence of charge at the advancing wavefront could influence the electric field ahead of it, with this influence decaying with distance from the charge front. Such an influence is believed to be very small and is therefore assumed to be zero, with the electric field ahead of the advancing front assumed to be constant.

Integrating (4.5) we have

$$\int \frac{dv}{dt} dt = \frac{q}{m} \int E dt,$$

or

$$v = \frac{q}{m} E_0 t + c_2, \quad (4.6)$$

from (4.4), giving rise to the following expressions for the velocity field along curves originating at $t = 0$. Applying the conditions (4.2d) and (4.2e) we have

$$v = \frac{q}{m} E_0 t + v_i, \quad (s_0, 0), \quad (4.7)$$

$$v = \frac{q}{m} E_0 t, \quad (x_p, 0), \quad (4.8)$$

where $(s_0, 0)$ represents the origin of the curve at $(x = s_0, t = 0)$, and $(x_p, 0)$ the origin of the curves at $(x = x_p, t = 0)$, and where $x_p \in (s_0, x_T]$. Expressions for the family of characteristic curves can now be determined by writing (4.6) as

$$\frac{dx}{dt} = \frac{q}{m} E_0 t + c_2,$$

which, upon integration, gives rise to the curves

$$x = \frac{q}{2m} E_0 t^2 + v_i t + s_0, \quad (s_0, 0), \quad (4.9a)$$

$$x = \frac{q}{2m} E_0 t^2 + x_p, \quad (x_p, 0), \quad (4.9b)$$

from (4.7) and (4.8); here, as before, $(s_0, 0)$ and $(x_p, 0)$ represent the origins of the curves.

Equations (4.7) and (4.9a) are simply the expected speed and position at time t of a single particle (within the acceleration gap) with a charge-mass ratio of (q/m) under a uniform acceleration of magnitude $\frac{q}{m} E_0$, emitted from

the initial plasma boundary (located at s_0). Additionally, whilst (4.9b) and (4.8) represent the location and gradient (respectively) of characteristics in the charge free part of the solution region, they also represent the expected speeds and positions of single particles, if they were emitted from differing locations (x_p) between the initial plasma boundary (s_0) and the fixed target (x_T). The characteristic curve (4.9a) also separates the charge free and charge infused parts of the solution region, and represents the location of the advancing particle wavefront. Figure 4.2 shows the curve (4.9a) and family of traces (4.9b) for single deuterons within an acceleration region bounded by a fixed target located 0.01m from the initial plasma boundary, and with an applied potential difference of 120kV. The part of the solution region enclosed by the separation characteristic, the lower $t = 0$ boundary, and the right hand fixed target is charge free, with the electric field being constant (E_0) everywhere within it.

4.2.2 Analytic Solution Behind the Advancing Charge Front

A further analysis of the time dependent system, (4.1), has been developed and is now described. This new analytic approach to the problem, once again, considers suitable characteristic curves giving rise to a partial analytic solution to the full time-dependent problem; it yields the closed form of the variable $\partial v / \partial x$ on characteristic curves behind the advancing charge front. The analysis is as follows.

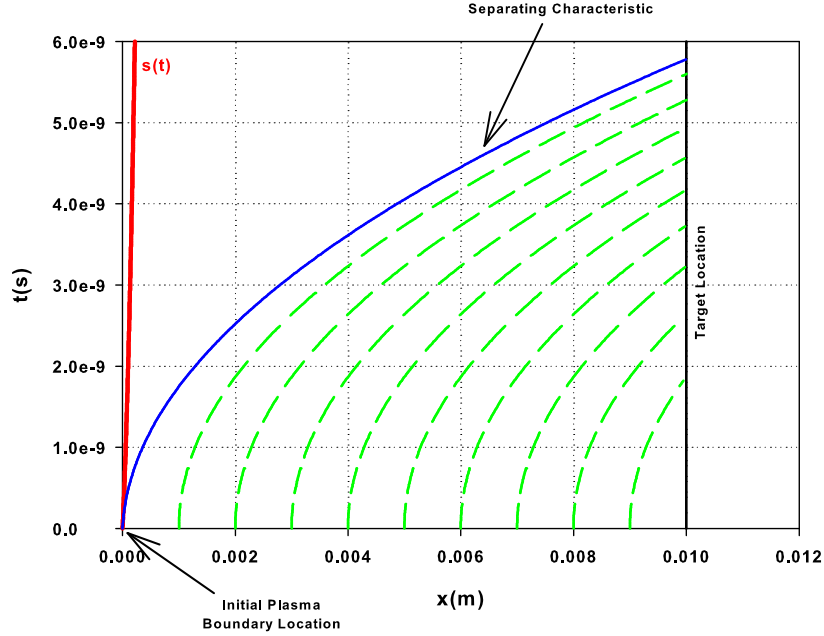


Figure 4.2: Actual characteristic curves spanning the charge free part of the solution region enclosed by the separation characteristic, the lower $t = 0$ boundary and the right hand fixed target. An impression of the moving plasma boundary is shown (marked $s(t)$).

By taking the derivative of (4.1a) with respect to x , we have

$$\left(\frac{\partial v}{\partial x}\right)^2 + v \frac{\partial}{\partial x} \left(\frac{\partial v}{\partial x}\right) + \frac{\partial}{\partial x} \left(\frac{\partial v}{\partial t}\right) = \frac{q}{m} \frac{\partial E}{\partial x}. \quad (4.10)$$

Once again, introducing a family of characteristics, where in this case it is useful to introduce the coordinate σ , so that $x = x(\sigma)$, $t = t(\sigma)$, with σ being measured along the characteristics and being defined by

$$\frac{dx}{d\sigma} = v, \quad (4.11)$$

$$\frac{dt}{d\sigma} = 1, \quad (4.12)$$

allows (4.10) to be written on the characteristics as

$$\frac{d}{d\sigma} \left(\frac{\partial v}{\partial x} \right) = \frac{q}{m\varepsilon_0} \rho - \left(\frac{\partial v}{\partial x} \right)^2 \quad (4.13)$$

from (4.1c); here it is assumed that

$$\frac{\partial}{\partial x} \left(\frac{\partial v}{\partial t} \right) = \frac{\partial}{\partial t} \left(\frac{\partial v}{\partial x} \right).$$

Defining the function

$$\begin{aligned} \alpha(\sigma) &= \alpha(x(\sigma), t(\sigma)) \\ &= \frac{\partial v}{\partial x}, \end{aligned}$$

and writing (4.13) in terms of α gives

$$\frac{d\alpha}{d\sigma} = \frac{q}{m\varepsilon_0} \rho - \alpha^2. \quad (4.14)$$

Now expanding (4.1b) we have

$$v \frac{\partial \rho}{\partial x} + \frac{\partial \rho}{\partial t} = -\rho \frac{\partial v}{\partial x}, \quad (4.15)$$

and when similarly defining $\rho(\sigma) = \rho(x(\sigma), t(\sigma))$ on the characteristics we have

$$\frac{d\rho}{d\sigma} = -\rho\alpha, \quad (4.16)$$

for (4.15). Taking the derivative of (4.14) with respect to σ gives

$$\begin{aligned} \frac{d}{d\sigma} \left(\frac{d\alpha}{d\sigma} + \alpha^2 \right) &= \frac{q}{m\varepsilon_0} \frac{d\rho}{d\sigma} \\ &= -\frac{q}{m\varepsilon_0} \rho\alpha, \end{aligned}$$

from (4.16), or,

$$\frac{1}{\alpha} \frac{d^2\alpha}{d\sigma^2} + 2 \frac{d\alpha}{d\sigma} + \frac{q}{m\varepsilon_0} \rho = 0. \quad (4.17)$$

Substituting (4.14) into (4.17) gives the second order non-linear ordinary differential equation for $\alpha(\sigma)$

$$\frac{d^2\alpha}{d\sigma^2} + 3\alpha\frac{d\alpha}{d\sigma} + \alpha^3 = 0. \quad (4.18)$$

on the characteristics.

4.2.2.1 Linearisation of the Riccati equation

The non-linear ordinary differential equation (4.18) is a Riccati equation of order two³, and can be linearised by making the substitution ([25], [35], [43])

$$\alpha(\sigma) = \frac{1}{z(\sigma)} \frac{dz(\sigma)}{d\sigma}, \quad (4.19)$$

whereby

$$\frac{d\alpha}{d\sigma} = \frac{1}{z} \frac{d^2z}{d\sigma^2} - \frac{1}{z^2} \left(\frac{dz}{d\sigma} \right)^2, \quad (4.20)$$

and

$$\frac{d^2\alpha}{d\sigma^2} = \frac{1}{z} \frac{d^3z}{d\sigma^3} - \frac{3}{z^2} \frac{dz}{d\sigma} \frac{d^2z}{d\sigma^2} + \frac{2}{z^3} \left(\frac{dz}{d\sigma} \right)^3. \quad (4.21)$$

Substituting (4.19), (4.20) and (4.21) into (4.18) reduces it to the particularly simple third order equation

$$\frac{d^3z}{d\sigma^3} = 0,$$

which can be immediately integrated giving

$$z(\sigma) = A\sigma^2 + B\sigma + C,$$

³It also known as a modified Emden-type equation, or modified Painlevé-Ince equation.

where A , B , and C are integration constants. The variable $\alpha(\sigma)$ can now be recovered giving

$$\begin{aligned}\alpha(\sigma) &= \left. \frac{\partial v}{\partial x} \right|_{\sigma} \\ &= \frac{2A\sigma + B}{A\sigma^2 + B\sigma + C} \\ &= \frac{2\sigma + B_1}{\sigma^2 + B_1\sigma + C_1},\end{aligned}\tag{4.22}$$

from (4.19), where $B_1 = B/A$ and $C_1 = C/A$. From (4.12), we see that $\sigma = t - t_0$, where t_0 is a parameter representing the origin of that particular characteristic on the $s(t)$ boundary, so that $\alpha(\sigma)$ can be written

$$\begin{aligned}\tilde{\alpha}(t) &= \alpha(\sigma(t)) \\ &= \left. \frac{\partial v}{\partial x} \right|_t \\ &= \frac{2t + B_2}{t^2 + B_2t + C_2},\end{aligned}\tag{4.23}$$

where $B_2 = B_1 - 2t_0$, and $C_2 = C_1 + t_0^2 - B_1t_0$, from (4.22).

4.2.2.2 Determination of $\partial v/\partial x$ at the plasma boundary.

Since $v = v_i$ at the plasma boundary (from (4.2d)), then its derivative (following the boundary) is zero there, or

$$\left[s'(t) \frac{\partial v}{\partial x} + \frac{\partial v}{\partial t} \right]_{x=s(t)} = 0.\tag{4.24}$$

Additionally, we have from (4.1a)

$$\left[v_i \frac{\partial v}{\partial x} + \frac{\partial v}{\partial t} \right]_{x=s(t)} = 0,\tag{4.25}$$

since $E(s(t), t) = 0$ from (4.2c), and again noting $v(s(t), t) = v_i$. Subtracting (4.24) from (4.25),

$$\left[(v_i - s'(t)) \frac{\partial v}{\partial x} \right]_{x=s(t)} = 0,$$

and since $v_i > s'(t)$ (or particles would never be able to leave the plasma boundary), we conclude

$$\left[\frac{\partial v}{\partial x} \right]_{x=s(t)} = 0. \quad (4.26)$$

By defining the time t_s to be the time when the plasma boundary is at the location $s(t_s)$, then $(s(t_s), t_s)$ is the origin of a particular characteristic on the plasma boundary. It is possible to deduce that characteristics originating at the plasma boundary monotonically increase without crossing each other, so that $t = t_s$ once, and only once, on a particular characteristic. With this in mind, we can apply the boundary condition (4.26) to (4.23), thereby determining the constant B_2 in terms of t_s .

It is also possible that the constant C_2 can be determined, although the resulting equation for $\partial v / \partial x$ is likely to be very implicit.

4.3 Numerical Schemes for the Determination of the Time-dependent Solution

Progression to a full analytic time-dependent solution appears difficult, and so we now appeal to numerical algorithms for the determination of the full time-dependent solution of the system, describing the two numerical approaches mentioned above.

Sets of results have been chosen to highlight features of the two methods, which were both implemented in MATLAB.

The physical conditions generally applied to the problem are listed as fol-

lows:

- **General Physical Conditions for the Problem**

- Target potential $\phi_T = 100 \text{ kV}$;
- Source emission potential $\phi_S = 0 \text{ V}$;
- Particle emission velocity $v_i = 69181.8 \text{ ms}^{-1}$ (deuterons emitted with an energy of 50eV);
- Source current density $J_0 = 1.88 \times 10^4 \text{ Am}^{-2}$;
- Initial region size $L = 0.01 \text{ m}$.

4.3.1 Reduction of the Time-dependent System to Dimensionless Form

Before the numerical methods are developed, the system, (4.1), and associated boundary conditions, (4.2), are re-written in dimensionless form. To do this, we can define the dimensionless variables

$$\tilde{\phi} = \frac{\phi}{\phi_m}, \quad (4.27a)$$

$$\tilde{\rho} = \frac{\rho}{\rho_m}, \quad (4.27b)$$

$$\tilde{v} = \frac{v}{v_m}, \quad (4.27c)$$

$$\tilde{x} = \frac{x}{L}, \quad (4.27d)$$

$$\tilde{E} = \frac{E}{E_0}, \quad (4.27e)$$

$$\text{and, } \tilde{t} = \frac{t}{t_m}, \quad (4.27f)$$

where $\phi_m = \phi_S - \phi_T$ is the potential difference across the region, ρ_m is the maximum charge density (naturally located at the moving emission boundary), v_m is the maximum particle speed (located at the target boundary), $L = x_T - s_0$ is the initial region size, $E_0 = \phi_m/L$ is the constant initial electric field magnitude, and t_m the estimated time taken for a particle to traverse the region. For the purposes of developing the dimensionless set of equations, it is convenient to assume that particles are emitted from the emission plasma boundary with no initial energy, even though this is not true in reality. With this in mind, a particle reaching the target, having undergone linear acceleration across the region from an initial speed of zero, will have a final, maximum speed

$$v_m = \sqrt{\frac{2q\phi_m}{m}}, \quad (4.28)$$

where q is the particle charge and m its mass, as usual. At this speed, a particle will then take the time

$$t_m = \frac{L}{v_m} \quad (4.29)$$

to cross the initial region, and we shall use t_m as the time scale.

Using these variables, the system, (4.1), can now be written in dimensionless form. To do this, initially, the variables (4.27a), (4.27d), and (4.27e) are substituted into the electric scalar potential definition, (4.1d), giving

$$\begin{aligned} \tilde{E} &= -\frac{\phi_m}{LE_0} \frac{\partial \tilde{\phi}}{\partial \tilde{x}} \\ &= -\frac{\partial \tilde{\phi}}{\partial \tilde{x}}. \end{aligned} \quad (4.30)$$

Also, substituting the variables (4.27b), (4.27d) and (4.27e) into (4.1c) gives

$$\begin{aligned}\frac{\partial \tilde{E}}{\partial \tilde{x}} &= \frac{L\rho_m}{E_0\varepsilon_0}\tilde{\rho} \\ &= -\frac{\partial^2 \tilde{\phi}}{\partial \tilde{x}^2},\end{aligned}$$

from (4.30), or

$$\frac{\partial^2 \tilde{\phi}}{\partial \tilde{x}^2} = -\alpha_1 \tilde{\rho}, \quad (4.31)$$

where the dimensionless parameter,

$$\alpha_1 = \frac{L^2 \rho_m}{\phi_m \varepsilon_0}, \quad (4.32)$$

has a typical value of $O(10)$.

Additionally, substituting (4.27c), (4.27d), (4.27e), and (4.27f) into (4.1a), we have

$$\frac{\partial \tilde{v}}{\partial \tilde{t}} = \frac{\tilde{E}}{2} - \tilde{v} \frac{\partial \tilde{v}}{\partial \tilde{x}}, \quad (4.33)$$

and finally, substituting (4.27b), (4.27c), (4.27d), and (4.27f) into (4.1b) we have

$$\begin{aligned}\frac{\partial \tilde{\rho}}{\partial \tilde{t}} &= -\frac{v_m t_m}{L} \left(\tilde{\rho} \frac{\partial \tilde{v}}{\partial \tilde{x}} + \tilde{v} \frac{\partial \tilde{\rho}}{\partial \tilde{x}} \right) \\ &= -\left(\tilde{\rho} \frac{\partial \tilde{v}}{\partial \tilde{x}} + \tilde{v} \frac{\partial \tilde{\rho}}{\partial \tilde{x}} \right).\end{aligned} \quad (4.34)$$

Grouping the derived dimensionless equations together, we have

$$\frac{\partial^2 \tilde{\phi}}{\partial \tilde{x}^2} = -\alpha_1 \tilde{\rho}, \quad (4.35a)$$

$$\frac{\partial \tilde{v}}{\partial \tilde{t}} = \frac{\tilde{E}}{2} - \tilde{v} \frac{\partial \tilde{v}}{\partial \tilde{x}}, \quad (4.35b)$$

$$\frac{\partial \tilde{\rho}}{\partial \tilde{t}} = -\left(\tilde{\rho} \frac{\partial \tilde{v}}{\partial \tilde{x}} + \tilde{v} \frac{\partial \tilde{\rho}}{\partial \tilde{x}} \right), \quad (4.35c)$$

which are to be solved on the region $\tilde{s}(\tilde{t}) \leq \tilde{x} \leq \tilde{x}_T$, where

$$\tilde{s}(\tilde{t}) = \frac{s(t)}{L}$$

and, $\tilde{x}_T = \frac{x_T}{L}$.

The equations, (4.35), are to be solved in conjunction with the dimensionless boundary conditions

$$\begin{aligned} \tilde{\phi}(\tilde{x}_T, \tilde{t}) &= \frac{\phi_T}{\phi_m} \\ &= \tilde{\phi}_T = \text{const}, \quad \tilde{t} \geq 0 \end{aligned} \quad (4.36a)$$

$$\begin{aligned} \tilde{\phi}(\tilde{s}(\tilde{t}), \tilde{t}) &= \frac{\phi_S}{\phi_m} \\ &= \tilde{\phi}_S = \text{const}, \quad \tilde{t} \geq 0 \end{aligned} \quad (4.36b)$$

$$\left. \frac{\partial \tilde{\phi}}{\partial \tilde{x}} \right|_{(\tilde{s}(\tilde{t}), \tilde{t})} = 0, \quad \tilde{t} > 0 \quad (4.36c)$$

$$\begin{aligned} \tilde{v}(\tilde{s}(\tilde{t}), \tilde{t}) &= \frac{v_i}{v_m} \\ &= \tilde{v}_i = \text{const}, \quad \tilde{t} \geq 0 \end{aligned} \quad (4.36d)$$

$$\tilde{v}(\tilde{x}, 0) = 0, \quad \tilde{x} \in (\tilde{s}_0, \tilde{x}_T] \quad (4.36e)$$

$$\begin{aligned} \tilde{\rho}(\tilde{s}(\tilde{t}), \tilde{t}) &= \frac{\rho_s(t)}{\rho_m} \\ &= \tilde{\rho}_s(\tilde{t}), \quad \tilde{t} \geq 0 \end{aligned} \quad (4.36f)$$

$$\tilde{\rho}(\tilde{x}, 0) = 0 \quad \tilde{x} \in (\tilde{s}_0, \tilde{x}_T], \quad (4.36g)$$

where $\tilde{s}_0 = \tilde{s}(0)$. It is noted that if $\phi_T = 0$ (which is often the case in experiment), then $\tilde{\phi}_T = 0$ and $\tilde{\phi}_S = 1$.

4.3.2 Numerical Method 1 for the Determination of the Time-dependent Solution

The three dimensionless, coupled equations, (4.35), can be used in a time stepping algorithm to attempt to determine the time-dependent solution to the plasma boundary problem in one dimension. The proposed algorithm is broadly as follows:

1. The initial solution region is set with the initial plasma boundary location being defined as $\tilde{s}(0) = \tilde{s}_0$;
2. Set $\tilde{\rho}(\tilde{x}, 0) = \tilde{v}(\tilde{x}, 0) = 0$, where $\tilde{x} \in (\tilde{s}, \tilde{x}_T]$;
3. Set $\tilde{\rho}(\tilde{s}, \tilde{t}) = \tilde{\rho}_s(\tilde{t})$ and $\tilde{v}(\tilde{s}, \tilde{t}) = \tilde{v}_i$, from (4.36d) and (4.36f), where $\tilde{\rho}_s(\tilde{t})$ is the dimensionless time-dependent function representing the time-dependent variation in current density at the plasma boundary during tube operation, and \tilde{v}_i the initial dimensionless particle velocity (a constant in this case, although not necessarily so);
4. Calculate the potential field $\tilde{\phi}(\tilde{x}, \tilde{t}^k)$ from (4.35a), using the conditions (4.36a) and (4.36b), and the most recent value of the charge density field (\tilde{t}^k refers to the time at the k^{th} time step with \tilde{t}^0 being the initial time step; this is detailed later);
5. Calculate the electric field $\tilde{E}(\tilde{x}, \tilde{t}^k)$ from the potential field $\tilde{\phi}(\tilde{x}, \tilde{t}^k)$, using (4.30);
6. Calculate the updated velocity field, $\tilde{v}(\tilde{x}, \tilde{t}^{k+1})$, from (4.35b), using $\tilde{E}(\tilde{x}, \tilde{t}^k)$, and $\tilde{v}(\tilde{x}, \tilde{t}^k)$;

7. Calculate the updated charge density field, $\tilde{\rho}(\tilde{x}, \tilde{t}^{k+1})$, from (4.35c), using $\tilde{\rho}(\tilde{x}, \tilde{t}^k)$ and $\tilde{v}(\tilde{x}, \tilde{t}^{k+1})$ from Step 5;
8. Investigate the electric field magnitude $\tilde{E}(\tilde{s}, \tilde{t}^{k+1})$ at the present location of the emission boundary. If this is not zero, by calculating the electric field gradient and curvature at this point, predict the location of the boundary where it is likely to be zero and adjust the boundary location accordingly;
9. Return to step (3) and repeat until the solutions in successive time steps are identical to within a small assigned parameter.

4.3.2.1 Mapping from the Moving Physical Domain to a Fixed Logical Domain

As a consequence of the moving plasma boundary, $\tilde{s}(t)$, the solution region is time-dependent. If the system of equations, (4.35), is to be discretised using differences (as is proposed here), then nodal spacing in the spatial domain will be time dependent, introducing a variation in accuracy at each time-step. In order to avoid this, we can map the differential equations, (4.35), to a fixed, logical region with a logical spatial independent variable $\xi \in [0, 1]$, and logical time variable $\tau \in [0, \infty)$. By doing this, since the physical domain is time-dependent, the mapped differential equations will change in form with time, such that a different system is solved in logical space at each point in time. However, since the logical region is fixed, equally spaced differences can be used to solve the different differential equations arising as a consequence of the mapping at each time step, with the physical solution being reconstructed subsequently.

To perform the mapping, the dimensionless physical independent variables are now written $\tilde{x} = \tilde{x}(\xi, \tau)$, and $\tilde{t} = \tilde{t}(\xi, \tau)$, and in order to introduce a method of varying the physical spatial variable \tilde{x} with the logical variable in a non-linear, time-dependent way, we introduce the mapping function $M(\xi, \tau)$. Here, we choose

$$\begin{aligned} M(\xi, \tau) &= \frac{\partial \tilde{x}}{\partial \xi} \\ &= \frac{\kappa_s(\tau)}{\sqrt{1 + \mu(\hat{f}_\xi)^2}}, \end{aligned} \tag{4.37}$$

where the function $\hat{f}(\xi, \tau) = \hat{f}(\tilde{x}(\xi, \tau), \tilde{t}(\xi, \tau))$ is a chosen required physical solution variable mapped to the logical region (the subscript variable denoting a partial derivative with respect to it and two subscripted variables denoting the second partial derivative etc.); μ is a chosen parameter. The mapping function, $M(\xi, \tau)$, is similar to *monitor* functions that are commonly employed in moving mesh methods (see [33], for example); a detailed analysis of their use can be found in [42]. By using a mapping function of the form (4.37), the spatial nodal density can be made to adapt to the solution at the previous time step and so the use of (4.37) provides a mechanism for adaptively controlling the spatial nodal density (also used in [30]).

The scaling parameter, $\kappa_s(\tau)$, is a time-dependent normalisation parameter used to define the physical region size (since the physical region size is time-dependent); it must be extracted as part of the solution, to determine the physical nodal density at a particular time. Clearly, where $\hat{f}(\xi, \tau)$ varies rapidly with ξ , then depending upon the magnitude of the parameter μ , the mapping function $M(\xi, \tau)$ (and hence the rate of change of physical variable with logical variable) is small (thus in a discrete scheme, nodes will be

concentrated in this area). Where $\hat{f}(\xi, \tau)$ varies very slowly (or not at all) with ξ , the mapping function $M(\xi, \tau)$ is approximately constant in ξ , and is equal to the scaling parameter $\kappa_s(\tau)$. The parameter μ can be chosen to offer further control over the rate of change of physical variable with logical variable.

Similarly, in addition to (4.37), and since we expect the plasma boundary position and hence the solution region to be rapidly changing, we control the rate of change physical time \tilde{t} with logical time τ by introducing the time step controlling function $G(\tau)$ given by

$$\begin{aligned} \frac{\partial \tilde{t}}{\partial \tau} &= G(\tau) \\ &= \frac{c_t}{\sqrt{1 + \nu(\hat{g}_\tau)^2}}, \end{aligned} \quad (4.38)$$

where c_t and ν are chosen constants, and $\hat{g}(\tau)$ is a suitably chosen time-dependent function, the derivative of which, \hat{g}_τ , is significant during times where the region size is changing rapidly. When the region size and consequently the function $\hat{g}(\tau)$ varies rapidly with time, the function $G(\tau)$, and hence the rate of change of physical time with logical time, is small. During periods of time where the region size is not changing rapidly, the rate of change of physical time with logical time will reduce to the constant c_t . Again, the parameter ν can be chosen to offer further control over the rate of change of physical variable with logical variable.

We can now re-write the system of equations (4.1a) to (4.1d) in terms of the logical variables ξ and τ , by firstly noting that we choose the physical time variable \tilde{t} to be independent of the logical spatial variable, ξ , or that $\tilde{t} = \tilde{t}(\tau)$ only. With this in mind, the derivatives within the system are transformed as follows.

Using the chain rule

$$\begin{aligned}\frac{\partial}{\partial \xi} &= \frac{\partial \tilde{x}}{\partial \xi} \frac{\partial}{\partial \tilde{x}} + \frac{\partial \tilde{t}}{\partial \xi} \frac{\partial}{\partial \tilde{t}} \\ &= M \frac{\partial}{\partial \tilde{x}},\end{aligned}\tag{4.39}$$

from (4.37), noting that $\partial \tilde{t} / \partial \xi = 0$, or

$$\frac{\partial}{\partial \tilde{x}} = \frac{1}{M} \frac{\partial}{\partial \xi}.\tag{4.40}$$

Also

$$\frac{\partial}{\partial \tau} = \frac{\dot{\tilde{x}}}{M} \frac{\partial}{\partial \xi} + G \frac{\partial}{\partial \tilde{t}},$$

from (4.38) and (4.39), or

$$\frac{\partial}{\partial \tilde{t}} = \frac{1}{G} \left(\frac{\partial}{\partial \tau} - \frac{\dot{\tilde{x}}}{M} \frac{\partial}{\partial \xi} \right).\tag{4.41}$$

Furthermore

$$\frac{\partial^2}{\partial \tilde{x}^2} = \frac{1}{M^2} \frac{\partial^2}{\partial \xi^2} - \frac{1}{M^3} \frac{\partial M}{\partial \xi} \frac{\partial}{\partial \xi},\tag{4.42}$$

from (4.40). The system of equations can now be restated in the logical domain as follows.

Using the above transformations, the non-dimensional definition (4.30) can be written as

$$\begin{aligned}\tilde{E}(\tilde{x}(\xi, \tau), \tilde{t}(\xi, \tau)) &= \hat{E}(\xi, \tau) \\ &= -\frac{1}{M} \frac{\partial \hat{\phi}}{\partial \xi},\end{aligned}\tag{4.43}$$

from (4.40), whilst (4.35a) can be rewritten

$$\begin{aligned}\frac{\partial^2 \tilde{\phi}}{\partial \tilde{x}^2} &= \frac{1}{M^2} \frac{\partial^2 \hat{\phi}}{\partial \xi^2} - \frac{1}{M^3} \frac{\partial M}{\partial \xi} \frac{\partial \hat{\phi}}{\partial \xi} \\ &= -\alpha_1 \hat{\rho},\end{aligned}\tag{4.44}$$

from (4.42), where $\hat{\phi}(\xi, \tau) = \tilde{\phi}(\tilde{x}(\xi, \tau), \tilde{t}(\xi, \tau))$.

Furthermore, using both (4.40) and (4.41), the time-dependent equations, (4.35b) and (4.35c) can be similarly transformed giving

$$\begin{aligned}\tilde{v} \frac{\partial \tilde{v}}{\partial \tilde{x}} + \frac{\partial \tilde{v}}{\partial \tilde{t}} &= \frac{1}{M} \left(\hat{v} - \frac{\dot{\hat{x}}}{G} \right) \frac{\partial \hat{v}}{\partial \xi} + \frac{1}{G} \frac{\partial \hat{v}}{\partial \tau} \\ &= \frac{\hat{E}}{2},\end{aligned}\tag{4.45}$$

or

$$\frac{\partial \hat{v}}{\partial \hat{t}} = G \left\{ \frac{\hat{E}}{2} + \frac{1}{M} \left(\frac{\dot{\hat{x}}}{G} - \hat{v} \right) \frac{\partial \hat{v}}{\partial \xi} \right\},\tag{4.46}$$

and

$$\frac{\partial(\tilde{\rho}\tilde{v})}{\partial \tilde{x}} = \frac{1}{G} \left(\frac{\dot{\hat{x}}}{M} \frac{\partial \hat{\rho}}{\partial \xi} - \frac{\partial \hat{\rho}}{\partial \tau} \right),\tag{4.47}$$

or, on expanding and rearranging

$$\frac{G}{M} \left\{ \hat{\rho} \frac{\partial \hat{v}}{\partial \xi} + \left(\hat{v} - \frac{\dot{\hat{x}}}{G} \right) \frac{\partial \hat{\rho}}{\partial \xi} \right\} = -\frac{\partial \hat{\rho}}{\partial \tau},\tag{4.48}$$

where $\tilde{v}(\tilde{x}(\xi, \tau), \tilde{t}(\xi, \tau)) = \hat{v}(\xi, \tau)$.

Now that the system of equations has been rewritten in terms of the logical variables ξ and τ , it can be solved on the fixed logical domain by noting that the conditions at the boundaries of the non-dimensional physical domain, (4.36a) to (4.36g), also apply at the boundaries of the logical domain. This is because, for example,

$$\begin{aligned}\hat{\phi}(\xi, \tau) &= \tilde{\phi}(\tilde{x}(\xi, \tau), \tilde{t}(\xi, \tau)) \\ &= \tilde{\phi}(\tilde{x}, \tilde{t}),\end{aligned}\tag{4.49}$$

and thus the potential condition (4.36a) on the target at \tilde{x}_T is then

$$\begin{aligned}\tilde{\phi}(\tilde{x}_T, \tilde{t}) &= \tilde{\phi}(\tilde{x}(1), \tilde{t}) \\ &= \hat{\phi}(1, \tau) \\ &= \tilde{\phi}_T = \text{const.}\end{aligned}$$

It is noted that the derivative condition (4.36c), applied to the plasma boundary in the physical region, is not explicitly applied in the logical region. This condition is utilised in Step 8 of the algorithm above, where it is used to determine the time-dependent location of the plasma boundary in the *physical* region. Since the plasma boundary location is adjusted in the physical region at each point in time, the physical region size and hence the forms of (4.43), (4.44), (4.47) and (4.48) are time-dependent, due to $\kappa_s(\tau)$ in (4.37) (as previously mentioned).

4.3.2.2 Numerical Implementation of the Time-stepping Algorithm Using Differences

In order to solve the system (4.43) to (4.48) on the logical solution domain using the algorithm above, we initially split the domain into n discrete, equally spaced subregions, giving rise to the $n + 1$ nodes $\{\xi_j\} \in [0, 1]$ separating the subregions. Each logical subregion has the size $\Delta\xi = 1/n$, so that the j^{th} node has the logical location $\xi_j = (j - 1)\Delta\xi$, where $j \in [1, n + 1]$ and $j \in \mathbb{Z}$. Additionally, within the problem, the time τ must fall in the range $\tau \in [0, \infty)$, with $\tau = 0$ indicating the point at which ions are first accelerated away from the emission plasma boundary. Representing time in a similarly discrete way, the k^{th} time step (with $k \in [1, \infty)$ and $k \in \mathbb{Z}$) can then be written τ^k , where $\{\tau^k\} \in [0, \infty)$. By choosing a fixed time step size $\Delta\tau$, the

k^{th} time step is then at the time $\tau^k = (k - 1)\Delta\tau$. Using this notation, the value $\hat{\rho}_j^k$ is the value of the charge density, say, within the logical region at the location $(j - 1)\Delta\xi$ and time $(k - 1)\Delta\tau$.

To determine solutions to (4.43), (4.44), (4.46), and (4.48) on the logical domain, we must first determine an expression for the time-dependent scaling parameter $\kappa_s(\tau)$. This can be done by integrating (4.37) to give

$$\begin{aligned}\tilde{x}_T &= \tilde{s}(\tilde{t}) + \int_0^1 M(\xi, \tau) \, d\xi \\ &= \tilde{s}(\tilde{t}) + \kappa_s(\tau) \sum_{j=1}^n \int_{\xi_j}^{\xi_{j+1}} \frac{d\xi}{\sqrt{1 + \mu(\hat{f}_\xi)^2}}\end{aligned}\quad (4.50)$$

for the $n + 1$ nodal points $\{\xi_j\}$, where $\tilde{s}(\tilde{t})$ is the time-dependent plasma boundary location; \tilde{x}_T is the fixed target location. Rearranging (4.50) gives the required expression for $\kappa_s(\tau)$ as

$$\kappa_s(\tau) = (\tilde{x}_T - \tilde{s}(\tilde{t})) \cdot \left(\sum_{j=1}^n \int_{\xi_j}^{\xi_{j+1}} \frac{d\xi}{\sqrt{1 + \mu(\hat{f}_\xi)^2}} \right)^{-1}.\quad (4.51)$$

Physical node locations (and hence the solution in the physical domain) can then be recovered from (4.50), with the p^{th} nodal location being given by

$$\tilde{x}_p = \tilde{s}(\tilde{t}) + \kappa_s(\tau) \sum_{j=1}^p \int_{\xi_j}^{\xi_{j+1}} \frac{d\xi}{\sqrt{1 + \mu(\hat{f}_\xi)^2}},\quad (4.52)$$

with $\kappa_s(\tau)$ being given by (4.51).

Similarly, discrete time points in the physical domain corresponding to time steps in the logical domain, can be recovered from (4.38) by integrating with respect to τ , with the q^{th} physical time point being given by

$$\begin{aligned}\tilde{t}(\tau^q) &= \tilde{t}(0) + c_t \int_0^{\tau^q} G(\tau) \, d\tau \\ &= c_t \sum_{k=1}^q \int_{\tau^k}^{\tau^{k+1}} \frac{d\tau}{\sqrt{1 + \nu(\hat{g}_\tau)^2}},\end{aligned}\quad (4.53)$$

where $\tilde{t}(0) = 0$ (time starts when particles are first emitted from the plasma boundary).

Before numerically approximating the algorithm listed above by discretising the logical solution domain as described (using finite differences to represent derivatives), it is useful to list some standard derivative difference approximations.

- **Second order difference approximations** for the derivative $\partial f_j^k / \partial \xi$, at the nodal point $(j\Delta\xi, k\Delta\tau)$ for some function $f(\xi, \tau)$:

- Second order forward difference approximation

$$\frac{\partial f_j^k}{\partial \xi} \approx \frac{-3f_j^k + 4f_{j+1}^k - f_{j+2}^k}{2\Delta\xi} + O(\Delta\xi^2) \quad (4.54a)$$

- Second order central difference approximation

$$\frac{\partial f_j^k}{\partial \xi} \approx \frac{f_{j+1}^k - f_{j-1}^k}{2\Delta\xi} + O(\Delta\xi^2) \quad (4.54b)$$

- Second order backward difference approximation

$$\frac{\partial f_j^k}{\partial \xi} \approx \frac{3f_j^k - 4f_{j-1}^k + f_{j-2}^k}{2\Delta\xi} + O(\Delta\xi^2) \quad (4.54c)$$

- **Second order central difference approximation** for the derivative $\partial^2 f_j^k / \partial \xi^2$, at the nodal point $(j\Delta\xi, k\Delta\tau)$ for some function $f(\xi, \tau)$:

$$\frac{\partial^2 f_j^k}{\partial \xi^2} \approx \frac{f_{j+1}^k - 2f_j^k + f_{j-1}^k}{\Delta\xi^2} + O(\Delta\xi^2). \quad (4.55)$$

4.3.2.3 Detailed Numerical Algorithm

We now list a more detailed description of the steps in the implementation of the numerical time-stepping algorithm described above.

Step 1

- Set the initial physical region size by defining the initial plasma boundary location $s^1 = s(0) = s_0$ (noting that $\hat{s}^1 = 0$) and the target location x_T .
- Set the scaling parameters ϕ_m , ρ_m , and L ; consequently define the scaling parameters v_m , E_0 and t_m .
- Create the initial solution vectors $\{\hat{\rho}_j^1\} = \{\hat{v}_j^1\} = \{0\}$, where $j \in (1, n+1]$ and $j \in \mathbb{Z}$.

Step 2

- Set $\{\hat{v}_1^k\} = \tilde{v}_i$, where $k \in [1, m+1]$ and $k \in \mathbb{Z}$ (with m being the desired number of time steps).
- Set $\{\hat{\rho}_1^k\} = \tilde{\rho}_s(\tilde{t}^k)$, where $k \in [1, m+1]$ and $k \in \mathbb{Z}$, and where

$$\begin{aligned}\tilde{\rho}_s(\tilde{t}) &= \frac{h}{2} (1 + \tanh(b(t_m \tilde{t} - c))) \\ &= \frac{h}{(1 + e^{2b(c - t_m \tilde{t})})},\end{aligned}\tag{4.56}$$

for a ramped (in time) charge density at the plasma boundary, from (4.36f). In (4.56), the constants h , b , and c are parameters determining the shape of the ramp (see figure 4.3); in this case, $h = 1$ so that $\tilde{\rho}_s(\tilde{t}) \in (0, 1)$.

We choose a ramped (in time) charge density profile to represent the real physical situation, where the charge density is *switched on*, having a finite switch-on time (or ramp).

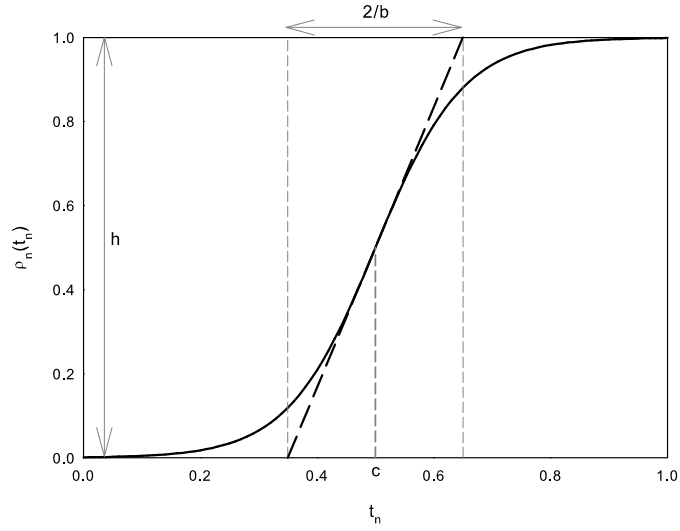


Figure 4.3: Function used to represent time-dependent charge density ramp. The parameters h , b , and c in (4.56) are indicated. The subscript n in the axis titles indicates a non-dimensional variable.

Step 3

- Choose the form of $\hat{f}(\xi, \tau)$ in (4.37).
- Choose the form of $\hat{g}(\tau)$ in (4.38).
- Select the parameters μ and ν in (4.37) and (4.38).

Step 4

- Determine $\{\hat{f}_{\xi_j}^k\}$ as follows:
 - When $j = 1$, calculate $\hat{f}_{\xi_1}^k$ from (4.54a);
 - When $1 < j < (n + 1)$, calculate $\hat{f}_{\xi_j}^k$ from (4.54b);
 - When $j = (n + 1)$, calculate $\hat{f}_{\xi_j}^k$ from (4.54c).

- Determine \hat{g}_τ^k as follows:
 - If $k = 1$, set $\hat{g}_\tau^k = 0$;
 - If $k > 1$, calculate \hat{g}_τ^k using the first order difference approximation

$$\hat{g}_\tau^k \approx \frac{\hat{g}^k - \hat{g}^{k-1}}{\Delta\tau}.$$

Step 5

- Using $\{\hat{f}_{\xi_j}^k\}$ from Step 4, calculate κ_s^k (κ_s at the current time step) from (4.51) making use of a simple trapezium rule approximation. For example, for some function $\hat{\theta}(\xi, \tau)$, then

$$\int_{\xi_j}^{\xi_{j+1}} \hat{\theta}(\xi, \tau) d\xi \approx \frac{\Delta\xi}{2} (\hat{\theta}_{j+1}^k + \hat{\theta}_j^k),$$

where $\hat{\theta}_j^k = \hat{\theta}((j-1)\Delta\xi, (k-1)\Delta\tau)$.

- From (4.37), and using the value κ_s^k just calculated with $\{\hat{f}_{\xi_j}^k\}$ from Step 4, determine the mapping function vector $\{M_j^k\}$ for the current (k^{th}) time step.
- From (4.38), and using \hat{g}_τ^k from Step 4, determine the scalar time step controlling function value G^k for the current (k^{th}) time step.

Step 6

- Recover the dimensionless physical nodal locations $\{\tilde{x}_j\}$ from (4.52), using $\{\hat{f}_{\xi_j}^k\}$ and κ_s^k from Steps 4 and 5. The simple trapezium rule approximation shown in Step 5 is used for evaluating the integral in (4.52). The dimensional, physical nodal locations are determined from $\{\tilde{x}_j\}$ by multiplying by the constant L , established in Step 1.

- Calculate the vector of physical nodal speeds $\{\dot{\tilde{x}}_j^k\} = \partial\tilde{x}/\partial\tau$ from the current and previous physical nodal locations.
 - If $k = 1$ then $\{\dot{\tilde{x}}_j^k\} = \{0\}$.
 - If $k > 1$ then calculate nodal speeds using the first order difference approximation

$$\dot{\tilde{x}}_j^k \approx \frac{\tilde{x}_j^k - \tilde{x}_j^{k-1}}{\Delta\tau}.$$

- From (4.53), recover the current, dimensionless physical time $\tilde{t}(\tau^k)$, using the vector of previous time step controlling function values $\{G^q\}$, where $q \in [1, k]$, $q \in \mathbb{Z}$. The dimensional, physical time is determined from $\tilde{t}(\tau^k)$ by multiplying by the value t_m , calculated in Step 1.

Step 7 Using $\{M_j^k\}$ from Step 5, solve

$$\frac{1}{M^2} \frac{\partial^2 \hat{\phi}^k}{\partial \xi^2} - \frac{1}{M^3} \frac{\partial M}{\partial \xi} \frac{\partial \hat{\phi}^k}{\partial \xi} = -\alpha_1 \hat{\rho}^k \quad (4.57)$$

in logical space, where $\hat{\rho}^k$ is the current charge density solution, and where α_1 is given by (4.32). To solve (4.57), we use the boundary conditions

$$\begin{aligned} \hat{\phi}_1^k &= \tilde{\phi}_T, \quad \text{and} \\ \hat{\phi}_{n+1}^k &= \tilde{\phi}_S \end{aligned}$$

for $\forall k \in [1, m+1]$, where $\tilde{\phi}_T$ and $\tilde{\phi}_S$ are the given conditions (4.36a) and (4.36b), noting (4.49). Since $\hat{\phi}$ is known at the boundaries of the logical domain, we need only determine the solution to (4.57) at interior nodal points (i.e. for $1 < j < (n+1)$). Thus we need only use the second order central difference approximations (4.54b) and (4.55) for the derivatives in (4.57). Using these approximations we arrive at the following system of equations for $\hat{\phi}_j^k$.

- When $j = 2$,

$$\begin{aligned} & -\frac{2}{(M_2^k)^2 \Delta \xi^2} \hat{\phi}_2^k + \left\{ \frac{1}{(M_2^k)^2 \Delta \xi^2} - \frac{M_{2\xi}^k}{2\Delta \xi (M_2^k)^3} \right\} \hat{\phi}_3^k \\ & = -\alpha_1 \hat{\rho}_2^k - \left\{ \frac{1}{(M_2^k)^2 \Delta \xi^2} + \frac{M_{2\xi}^k}{2\Delta \xi (M_2^k)^3} \right\} \phi_T. \end{aligned}$$

- When $2 < j < n$,

$$\begin{aligned} & \left\{ \frac{1}{(M_j^k)^2 \Delta \xi^2} + \frac{M_{j\xi}^k}{2\Delta \xi (M_j^k)^3} \right\} \hat{\phi}_{j-1}^k - \frac{2}{(M_j^k)^2 \Delta \xi^2} \hat{\phi}_j^k \\ & + \left\{ \frac{1}{(M_j^k)^2 \Delta \xi^2} - \frac{M_{j\xi}^k}{2\Delta \xi (M_j^k)^3} \right\} \hat{\phi}_{j+1}^k = -\alpha_1 \hat{\rho}_j^k. \end{aligned}$$

- When $j = n$,

$$\begin{aligned} & \left\{ \frac{1}{(M_n^k)^2 \Delta \xi^2} + \frac{M_{n\xi}^k}{2\Delta \xi (M_n^k)^3} \right\} \hat{\phi}_{n-1}^k - \frac{2}{(M_n^k)^2 \Delta \xi^2} \hat{\phi}_n^k \\ & = -\alpha_1 \hat{\rho}_n^k - \left\{ \frac{1}{(M_n^k)^2 \Delta \xi^2} - \frac{M_{n\xi}^k}{2\Delta \xi (M_n^k)^3} \right\} \hat{\phi}_1. \end{aligned}$$

Step 8 Using $\{\hat{f}_{\xi_j}^k\}$, $\{M_j^k\}$, and κ_s^k from Steps 4 and 5, calculate the electric field $\{\hat{E}_j^k\}$ in logical space from (4.1d) and (4.39), by determining

$$\hat{E}_j^k = -\frac{1}{M_j^k} \frac{\partial \hat{\phi}_j^k}{\partial \xi}. \quad (4.58)$$

As in Step 4, the three cases

- When $j = 1$ calculate the derivative $\partial \hat{\phi}_j^k / \partial \xi$ using (4.54a).
- When $1 < j < n + 1$ calculate the derivative $\partial \hat{\phi}_j^k / \partial \xi$ using (4.54b).
- When $j = n + 1$ calculate the derivative $\partial \hat{\phi}_j^k / \partial \xi$ using (4.54c).

apply for calculating the derivative in (4.58).

Step 9 Calculate the updated velocity field $\{\hat{v}_j^{k+1}\}$ at the next time step from (4.46), using $\{\hat{v}_j^k\}$, with $\{\hat{x}_j^k\}$, $\{M_j^k\}$, and G^k from Steps 5 and 6. By rearranging (4.45), an expression for the updated velocity at the node $(j\Delta\xi, k\Delta\tau)$ can be found using a forward difference approximation for the time derivative; this gives rise to the following:

- Using a first order forward difference approximation for the time derivative in (4.46) we have

$$\hat{v}_j^{k+1} = \hat{v}_j^k + \Delta\tau G^k \left\{ \frac{\hat{E}_j^k}{2} + \frac{1}{M_j^k} \left(\frac{\dot{\hat{x}}_j^k}{G^k} - \hat{v}_j^k \right) \frac{\partial \hat{v}_j^k}{\partial \xi} \right\}, \quad (4.59)$$

for the updated velocity field $\{\hat{v}_j^{k+1}\}$, where $\dot{\hat{x}}_j^k$ is the speed of the j^{th} physical node at the k^{th} time step, where

$$\frac{\partial \hat{v}_j^k}{\partial \xi} \approx \frac{\hat{v}_j^k - \hat{v}_{j-1}^k}{\Delta\xi}$$

for calculating the derivative in (4.59) also applies.

Step 10 Calculate the updated charge density field $\{\hat{\rho}_j^{k+1}\}$ at the next time step from (4.48), using the most recent velocity field, $\{\hat{v}_j^{k+1}\}$ from Step 9, with $\{M_j^k\}$, $\{\hat{x}_j^k\}$ and G^k from Steps 5 and 6. Rearranging (4.48), an expression for the updated charge density at the node $(j\Delta\xi, (k+1)\Delta\tau)$ can be found, again using a forward difference approximation for the time derivative; this gives rise to the following:

- Using a first order forward difference approximation for the time derivative in (4.48) we have

$$\hat{\rho}_j^{k+1} = \hat{\rho}_j^k - \frac{G^k \Delta\tau}{M_j^k} \left(\left(\hat{v}_j^{k+1} - \frac{\dot{\hat{x}}_j^k}{G^k} \right) \frac{\partial \hat{\rho}_j^k}{\partial \xi} + \hat{\rho}_j^k \frac{\partial \hat{v}_j^{k+1}}{\partial \xi} \right) \quad (4.60)$$

for the updated charge density field $\{\hat{\rho}_j^{k+1}\}$, where

$$\frac{\partial \hat{\rho}_j^k}{\partial \xi} \approx \frac{\hat{\rho}_j^k - \hat{\rho}_{j-1}^k}{\Delta \xi}$$

for calculating the derivative in (4.60) also applies.

Step 11

- Update the plasma boundary location by examining the electric field at the boundary $\tilde{E}(\tilde{s}^k, \tilde{t}^k) = \hat{E}_1^k$ from Step 8, where $\tilde{s}^k = \tilde{s}(\tilde{t}^k)$; the electric field gradient at the boundary

$$\frac{\partial \tilde{E}(\tilde{s}^k, \tilde{t}^k)}{\partial \tilde{x}} = \tilde{\rho}_s(\tilde{t}^k), \quad (4.61)$$

from (4.1c) and Step 2, and the electric field curvature at the boundary

$$\frac{\partial \tilde{E}_{\tilde{x}}(\tilde{s}^k, \tilde{t}^k)}{\partial \tilde{x}} = \frac{1}{M_0^k} \frac{\partial \hat{\rho}_0^k}{\partial \xi},$$

from (4.61) and (4.39), where the derivative $\partial \hat{\rho}_0^k / \partial \xi$ is calculated using the forward difference (4.54a).

An expression for the size of the boundary displacement at the time \tilde{t}^k can be found by determining a perturbation, $\Delta \tilde{s}(\tilde{t}^k) = \Delta \tilde{s}^k$, to the boundary using the Taylor expansion

$$\begin{aligned} \tilde{E}(\tilde{s}^k + \Delta \tilde{s}^k, \tilde{t}^k) &= \tilde{E}(\tilde{s}^k, \tilde{t}^k) + \Delta \tilde{s}^k \tilde{E}_{\tilde{x}}(\tilde{s}^k, \tilde{t}^k) \\ &\quad + \frac{(\Delta \tilde{s}^k)^2}{2} \tilde{E}_{\tilde{x}\tilde{x}}(\tilde{s}^k, \tilde{t}^k) + O(\Delta \tilde{s}_k^3). \end{aligned}$$

Truncating the expansion at the second order term, and making the assumption that the perturbation $\Delta \tilde{s}^k$ moves the boundary to its correct

location (i.e. where $\tilde{E}(\tilde{s}(\tilde{t}^k) + \Delta\tilde{s}^k, \tilde{t}^k) = 0$ from the condition (4.2c)), gives the expression

$$\Delta\tilde{s}^k = \frac{-\tilde{E}_{\tilde{x}}(\tilde{s}^k, \tilde{t}^k) \pm \sqrt{\tilde{E}_{\tilde{x}}(\tilde{s}^k, \tilde{t}^k)^2 - 2\tilde{E}(\tilde{s}^k, \tilde{t}^k)\tilde{E}_{\tilde{x}\tilde{x}}(\tilde{s}^k, \tilde{t}^k)}}{\tilde{E}_{\tilde{x}\tilde{x}}(\tilde{s}^k, \tilde{t}^k)} \quad (4.62)$$

for $\Delta\tilde{s}^k$. If the system is allowed to settle to an equilibrium state of particle flow⁴, we would expect that as $k \rightarrow \infty$ the plasma boundary will converge to the constant location $\tilde{s}(\tilde{t}^\infty) = \tilde{s}$, and hence also expect that $\Delta\tilde{s}^k \rightarrow 0$ as $k \rightarrow \infty$. Additionally, from the condition (4.2c), the term $2\tilde{E}(\tilde{s}^k, \tilde{t}^k)\tilde{E}_{\tilde{x}\tilde{x}}(\tilde{s}^k, \tilde{t}^k) \rightarrow 0$ as $k \rightarrow \infty$ in (4.62), indicating that we must take the positive square root (or $\Delta\tilde{s}^k \rightarrow 0$ as $k \rightarrow \infty$).

– If $(\tilde{E}_{\tilde{x}}(\tilde{s}^k, \tilde{t}^k)^2 - 2\tilde{E}(\tilde{s}^k, \tilde{t}^k)\tilde{E}_{\tilde{x}\tilde{x}}(\tilde{s}^k, \tilde{t}^k)) < 0$ then set $\Delta\tilde{s}^k = 0$.

Step 12

- Recover the dimensional solution variables from the dimensionless definitions (4.27a) to (4.27f).
- Increment k and return to Step 4.

The Boundary Perturbation Stabilisation Parameter. After implementing the algorithm, it was observed that execution would proceed to relatively long times only if the calculated boundary perturbation at each time-step was small. Therefore, to prevent the algorithm failing and thus obtain analysable results, an additional parameter, δ , was introduced, which pre-multiplies the calculated boundary perturbation, thus reducing its magnitude at each step; this allowed the numerical algorithm to proceed unhin-

⁴As in the time independent case.

dered, but with the unwanted payoff of the predicted boundary movement being un-physical.

To update the boundary location at each time-step, the calculated boundary perturbation, $\Delta\tilde{s}^k$, (given by (4.62)) is multiplied by the small parameter δ in that the updated boundary location at the $(k+1)^{\text{th}}$ time step is given by

$$\tilde{s}^{k+1} = \tilde{s}^k + \delta\Delta\tilde{s}^k.$$

The introduction of δ in this way allows the boundary perturbation to be reduced to a level that allows the numerical method to proceed without failure, although the calculated time-dependent boundary location is unlikely to be representative of the true physical case.

The algorithm detailed above has been coded in MATLAB, and we now present results from its operation on a test case chosen, in hindsight, to not only represent experimental operation of a neutron tube, but to also offer physically representative results within a reasonable computational time frame. In this test case, the charge density at the plasma boundary is ramped to a maximum over a period of tens of nanoseconds. However, prior to detailing these results, we derive a CFL condition ([26], [24]) applicable to the scheme employed; this ensures stable choices of logical spatial and time step size.

4.3.2.4 CFL condition

Implementation of the algorithm developed in Section §4.3.1 required experimentation, as one would expect. The logical spatial and temporal step size must be chosen to avoid numerical instability caused by violation of the CFL

condition ([26], p87) appropriate to the first order, upwinded difference approximations, (4.59) and (4.60). To determine the condition, and due to the dynamic nature of nodal point locations in the moving physical region, an explicit expression for it is now evaluated on the logical, fixed region, being initially given by

$$\hat{v}_w \leq \frac{\Delta\xi}{\Delta\tau}, \quad (4.63)$$

where $\Delta\xi$ is the logical nodal spacing and $\Delta\tau$ is the logical time step. The wave-speed \hat{v}_w is deemed to be the maximum speed of the initial particle wavefront as it crosses the logical region, and can be determined by considering the maximum wavefront speed in the non-dimensional physical region, as follows.

Particles initially released from the plasma boundary form a wavefront, which undergoes uniform acceleration across the non-dimensional physical region, caused by the initial charge free uniform electric field . Using the familiar expression for the distance travelled by a particle under uniform acceleration, the time \tilde{t}_c taken for the wavefront to traverse this region is found by determining the positive root of

$$1 = \tilde{v}_i \tilde{t}_c + \frac{1}{2} \tilde{a} \tilde{t}_c^2, \quad (4.64)$$

where \tilde{v}_i is the initial non-dimensional particle speed, and \tilde{a} is the non-dimensional uniform acceleration of the wavefront, with the 1 on the left hand side of (4.64) being the region size. Thus

$$\tilde{t}_c = \frac{1}{\tilde{a}} \left(-\tilde{v}_i + \sqrt{\tilde{v}_i^2 + 2\tilde{a}} \right). \quad (4.65)$$

The maximum wavefront speed in the non-dimensional physical region is

therefore given by

$$\begin{aligned}\tilde{v}_w &= \tilde{a}\tilde{t}_c + \tilde{v}_i \\ &= \sqrt{\tilde{v}_i^2 + 2\tilde{a}},\end{aligned}\tag{4.66}$$

from (4.65), where the non-dimensional acceleration \tilde{a} can be determined from (4.35b), since

$$\begin{aligned}\frac{d\tilde{v}}{d\tilde{t}} &= \tilde{v}\frac{\partial\tilde{v}}{\partial\tilde{x}} + \frac{\partial\tilde{v}}{\partial\tilde{t}} = \tilde{a}, \\ &= \frac{\tilde{E}}{2}.\end{aligned}$$

By applying the boundary conditions (4.36b) and (4.36c), the initial uniform electric field strength formed within the charge free non-dimensional region is

$$\begin{aligned}\tilde{E}_0 &= (\tilde{\phi}_S - \tilde{\phi}_T)/(\tilde{x}_T - \tilde{s}(0)) \\ &= 1,\end{aligned}$$

so that the maximum wave-speed (4.66) can be written

$$\tilde{v}_w = \sqrt{\tilde{v}_i^2 + 1}.\tag{4.67}$$

The mapping of physical non-dimensional time \tilde{t} to logical time τ , using the controlling function (4.38), indicates that the maximum rate of change of \tilde{t} with τ is given by

$$\left.\frac{\partial\tilde{t}}{\partial\tau}\right|_{\max} = c_t,$$

or by

$$\tilde{t} = c_t\tau.\tag{4.68}$$

If the time taken for the wavefront to cross the non-dimensional region is given by

$$\tilde{t}_w = \frac{1}{\tilde{v}_w}, \quad (4.69)$$

then the minimum time taken for the wavefront to cross the logical region will be

$$\begin{aligned} \hat{T}_w &= \frac{1}{\hat{v}_w} \\ &= \frac{1}{c_t} \tilde{t}_w, \end{aligned} \quad (4.70)$$

from (4.68), so that the maximum wave-speed in the logical region is

$$\hat{v}_w = c_t \sqrt{\tilde{v}_i^2 + 1} \quad (4.71)$$

from (4.67), (4.69) and (4.70). Additionally,

$$\begin{aligned} \tilde{v}_i &= \frac{v_i}{v_m} \\ &= \sqrt{\frac{m}{2q\phi_m}} v_i, \end{aligned}$$

from (4.28) and (4.36d), and when combined with (4.71), this gives rise to the condition

$$c_t \sqrt{\frac{m}{2q\phi_m} v_i^2 + 1} \leq \frac{\Delta\xi}{\Delta\tau},$$

from (4.63); this is applied to the logical spatial and time step sizes.

4.3.2.5 Test Case

To test the algorithm, the initial conditions listed at the start of §4.3, above, were applied. Here, the potential difference applied across the solution region was held constant in time, with particles emerging with a constant initial velocity (or energy); this was to represent an experimental setup, although

numerically, these conditions could have been time-dependent. The initial region size was adjusted in successive runs to accelerate convergence (towards the steady state solution) as numerical experiments progressed. Additionally, the maximum charge density ($\rho_m = J_0/v_i$) at the plasma boundary was selected to represent a typical value within an actual device, and the functions

$$\hat{f}(\xi, \tau) = \hat{\rho}(\xi, \tau) \quad (4.72a)$$

$$\hat{g}(\tau) = \tilde{s}(\tilde{t}(\tau)), \quad (4.72b)$$

were chosen as the governing functions in the mapping function, (4.37), and time step controlling function, (4.38), respectively.

Source Charge Density Ramp. In this case, as a representation of an experimental increase in charge density at the plasma boundary, the applied ramp is increased from zero to the constant value

$$\begin{aligned} \rho_s(t) &= J_0/v_i \\ &= \rho_m \\ &= \text{const} \end{aligned} \quad (4.73)$$

with the increase occurring over a period of time of the order of tens of nanoseconds⁵. Within the algorithm, this is effected using the function (4.56) shown in Figure 4.3, where the non-dimensional charge density is increased

⁵In comparison with experiment, this is actually at the short end of the ramp time frame, but was chosen this way after the necessary inclusion of the parameter, δ . The inclusion of δ causes the numerical method to execute very slowly and so to be able to examine the effects of a ramped increase in charge density reminiscent of any kind of experiment, the shortest applicable ramp time frame was chosen.

from zero to one over a period of non-dimensional time of maximum order ten. In this case (by referring to (4.56) and Figure 4.3) the constants b , c , and h are chosen to be

$$\begin{aligned} b &= 1 \times 10^8 \text{ s}^{-1}, \\ c &= \frac{3}{b} \\ &= 3 \times 10^{-8} \text{ s} \\ h &= \rho_m, \end{aligned}$$

where ρ_m is given by (4.73). These parameters cause a ramp rise time of ~ 6.88 non-dimensional units, or 20 ns; the value $t_m = 2.91$ ns follows from (4.28) and (4.29) (with $L = 0.009\text{m}$ from table 4.1).

4.3.2.6 Results

Application of the physical conditions listed in §4.3 above, including the short-timescale charge density ramp (detailed above) along with a logical time-step size of 5.5×10^{-3} non-dimensional units (corresponding to ~ 182 non-dimensional time steps per unit t_m , or an initial physical time step of 1.6×10^{-11} s), yielded results with a number of differing features; some of these are explained in the following paragraphs. Results are displayed in physical space.

It is pointed out here, that in order to obtain a suitable set of results, a number of numerical experiments were performed and these resulted in the set of parameters listed in Table 4.1 that allowed the algorithm to execute for ≥ 20000 time steps. Here, the time step size shown was chosen for stability, and allowed the procedure to proceed without failure to a final physical time

Parameter	Value	Description
m	20000	Number of time steps.
n	60	Number of spatial steps.
$d\tau$	5.42×10^{-3} units	Logical time step size.
μ	0.015	Parameter to adjust adaptive physical nodal density (see (4.37)).
ν	1×10^{-6}	Parameter to adjust adaptive physical time step size (see (4.38)).
c_t	1.0	Parameter to adjust physical time step size outside of adaptive regions (see (4.38)).
δ	1×10^{-3}	Parameter to adjust amount of boundary movement at each time step.
L	0.009 m	Region start size - final run.

Table 4.1: Numerical parameters for the one-dimensional time-dependent numerical method 1 test problem.

of 320 ns; at this time the applied source charge density ramp has stabilised. Numerical experiments showed that the number of nodes chosen ($n = 60$) was a compromise between speed and accuracy, with higher numbers of nodes significantly increasing execution time and significantly fewer nodes (<30) causing a violation of the CFL condition, (4.72), or other instability; these results are not detailed here. The initial region size of $L = 0.009$ m is typical

of a neutron tube source shield to target separation distance. The parameter c_t was set to a default value of 1. The parameters μ and ν in (4.37) and (4.38) were adjusted to aid speed of execution with the particular set of initial conditions used over a number of experiments. The resulting values chosen caused the most efficient execution of the algorithm in conjunction with the other parameters listed in Table 4.1.

The following Figures detail features from the calculated solution, and include comparisons between the time-dependent solution and known analytic solutions.

Figure 4.4 shows the calculated surface $\rho(x, t)$. The ramped increase in charge density at the plasma boundary is visible, as is the adaptive time stepping procedure, with widely spaced time steps to the left of the surface being due to zero boundary movement over this region of time; this is caused by the discriminant in (4.62) being negative, invoking the error trap condition detailed in Step 11 of the difference algorithm, above. Figure 4.5 shows level curves of charge density over the first ~ 93 ns. The plasma boundary is identified by the solid black line to the left of the Figure, and the time at which boundary movement begins (~ 33 ns) is clearly visible⁶. At this point, the sudden, rapid boundary movement is propagated within $\rho(x, t)$, and this is likely to be due to sudden changes in the time step controlling function G (which is dependent upon the rate of change of boundary position, (4.72b) and (4.38)). A reduction in the logical time step size would reduce this effect. The separation characteristic separating the charge free region (ahead of the

⁶It is pointed out that this time is largely a numerical artefact of the method employed and not necessarily a reflection of the true, physical situation.

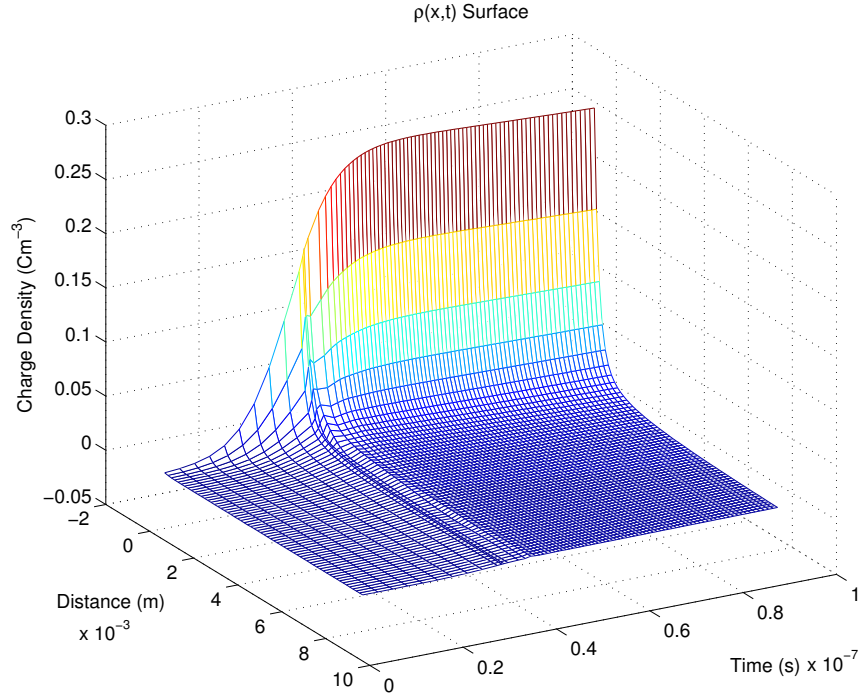


Figure 4.4: The charge density surface $\rho(x, t)$. Output is shown at every 200 time steps.

advancing wavefront) from the charge infused region behind it, is superimposed. The entire solution region is charge infused within ~ 6 ns, although due to the ramped initial condition at the plasma boundary, the charge density within the region is relatively low at this time. To identify a level curve close to the separation characteristic, a total of twenty logarithmically spaced levels are displayed in the range $10^{-4.5} \leq \rho(x, t) \leq 10^b$, where

$$b = \log \left(\max_{x, 0 \leq t \leq t_{\max}} [\rho(x, t)] \right),$$

and $t_{\max} = 93$ ns. This is further demonstrated by examining the solution up to the earlier time of ~ 10 ns in more detail, shown in Figure 4.6. Again,

similarly calculated level curves of charge density are displayed, where the curve towards the base of the Figure follows the superimposed separation characteristic closely. Figure 4.7, shows solutions extracted from the electric

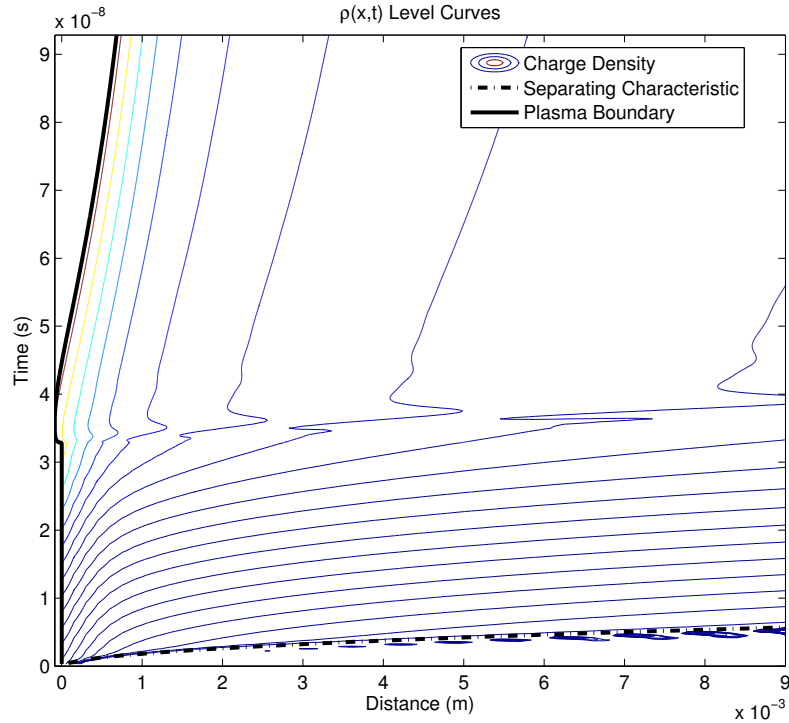


Figure 4.5: Logarithmically spaced level curves of constant charge density over the first ~ 93 ns.

scalar potential (voltage) surface $\phi(x, t)$ at different times. The progression from the initial charge free voltage solution (at 0 ns) towards the curved steady state solution is apparent, with the 93.08 ns curve appearing to be very close to the analytic (black “dash-dot”) steady state solution. Finally, Figure 4.8 shows the variation in plasma boundary location $s(t)$ with time. The red curve is the calculated plasma boundary location, whereas the green

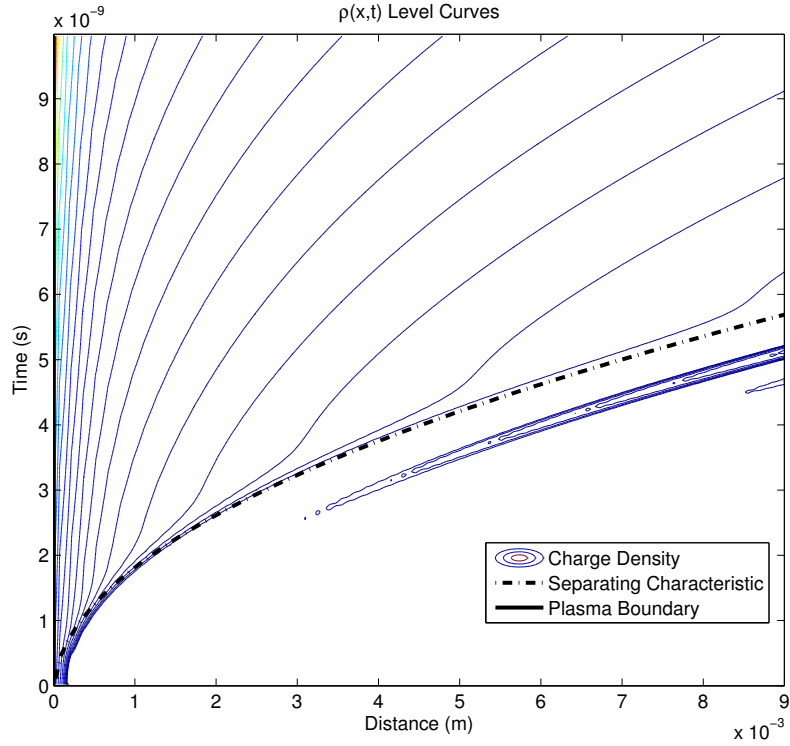


Figure 4.6: Logarithmically spaced level curves of constant charge density over the first ~ 10 ns.

“dash-dot” curve is the calculated plasma boundary perturbation $\Delta s(t)$; this function has been multiplied by the reciprocal of the parameter δ to increase its magnitude to enable display within the same graph as $s(t)$. By setting the initial region size to 0.09m, the numerical algorithm has taken ~ 93 ns for the calculated boundary position to reach the analytic steady state location; the algorithm was terminated at this point. Clearly, from the gradient of $s(t)$ as it reaches the steady-state boundary location, it is apparent that the calculated plasma boundary does not settle at this location and will overshoot somewhat as time progresses. By observing that after about ~ 50 ns, the perturbation

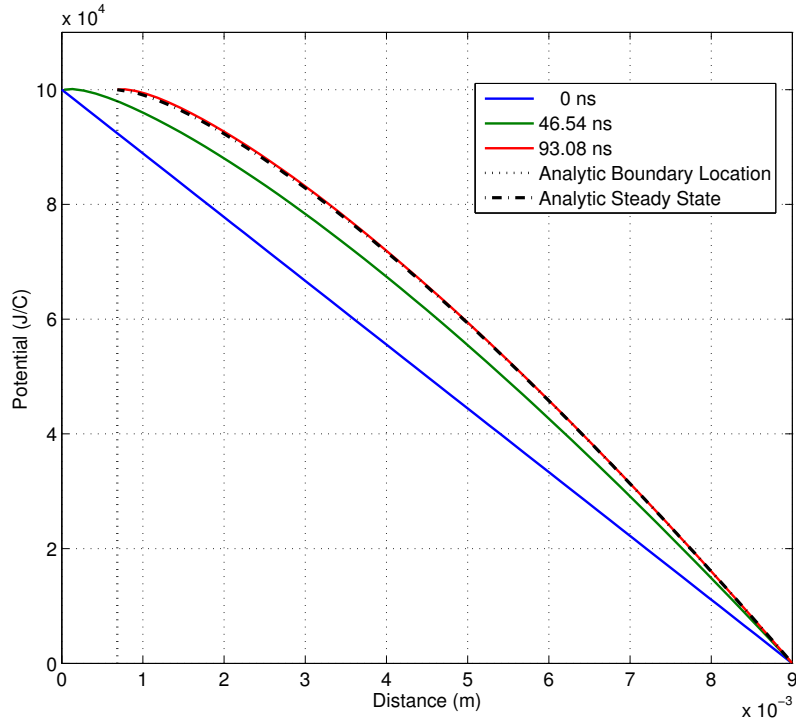


Figure 4.7: The variation of electric scalar potential (voltage) with distance across the region at different solutions times. The analytic steady state solution and steady boundary location are shown.

$\Delta s(t)$ is approximately linear, an estimate of when the boundary will begin to recede again can be made. Performing a linear regression on the linear portion of the function $\Delta s(t)$ allows the point at which perturbations become negative to be estimated; this is calculated to be ~ 219.6 ns, as shown in Figure 4.9. However, the increased electric field magnitude throughout the region, caused by the boundary movement and consequent reduced region size, may cause the boundary to begin to settle at an earlier time than this. Having observed calculation times for differing numbers of time-steps (Figure

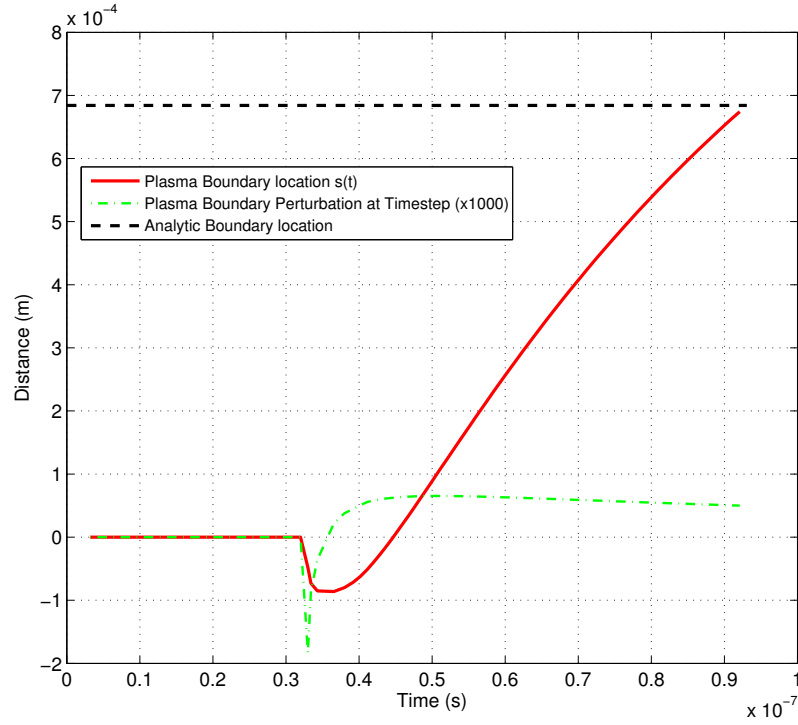


Figure 4.8: Variation in plasma boundary location $s(t)$, and plasma boundary perturbation $\Delta s(t)$, with time.

4.10), it is estimated that to reach a physical solution time of ~ 219.6 ns using the algorithm (in its current form) on the fastest desktop computer available, execution times will be ~ 8 hours, taking ~ 35000 time-steps (Figure 4.11). Due to arrangements surrounding the use of the computer, execution times of this size have not been possible. However, reaching this point in the calculated solution is largely academic as a consequence of the introduction of δ ; the predicted boundary movement is unlikely to be an accurate representation of the actual physical process.

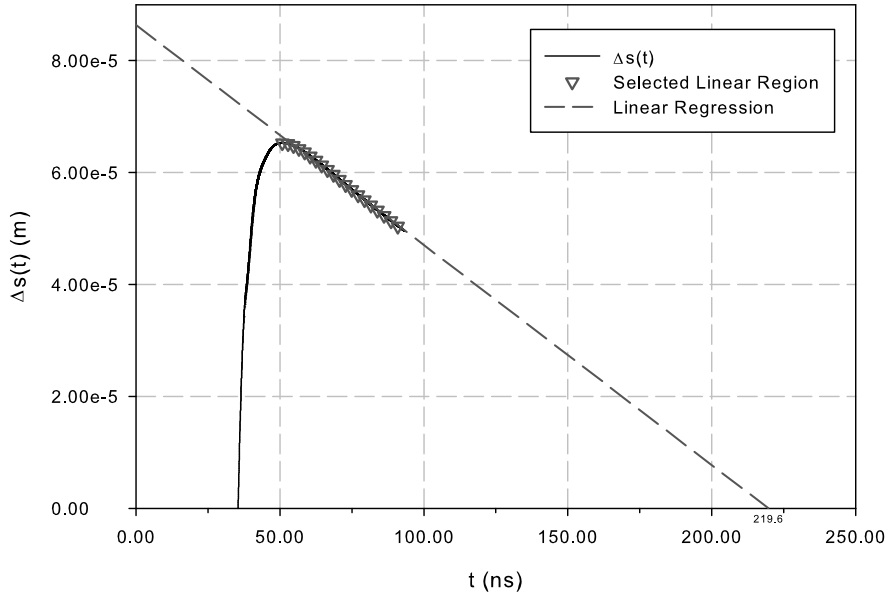


Figure 4.9: Estimated time at which the boundary perturbation $\Delta s(t)$ becomes negative.

Adaptive Nodal Density Procedure. To test the adaptive nodal density procedure, a number of runs were conducted for each case with differing values of the parameter μ . If μ was set to be of order ten, or greater, problems in calculating derivatives at the plasma boundary were observed. An example of this is shown in Figure 4.12, where the electric field (in physical space), derived from the calculated potential field via (4.58), has an apparent discontinuity at the plasma boundary. The failure is a consequence of the mapping function M_j^k (from (4.37)) becoming relatively small at the boundary and is caused by the gradient of the controlling function (4.72a) becoming very large there.

However, the relatively gentle increase in charge density (and hence con-

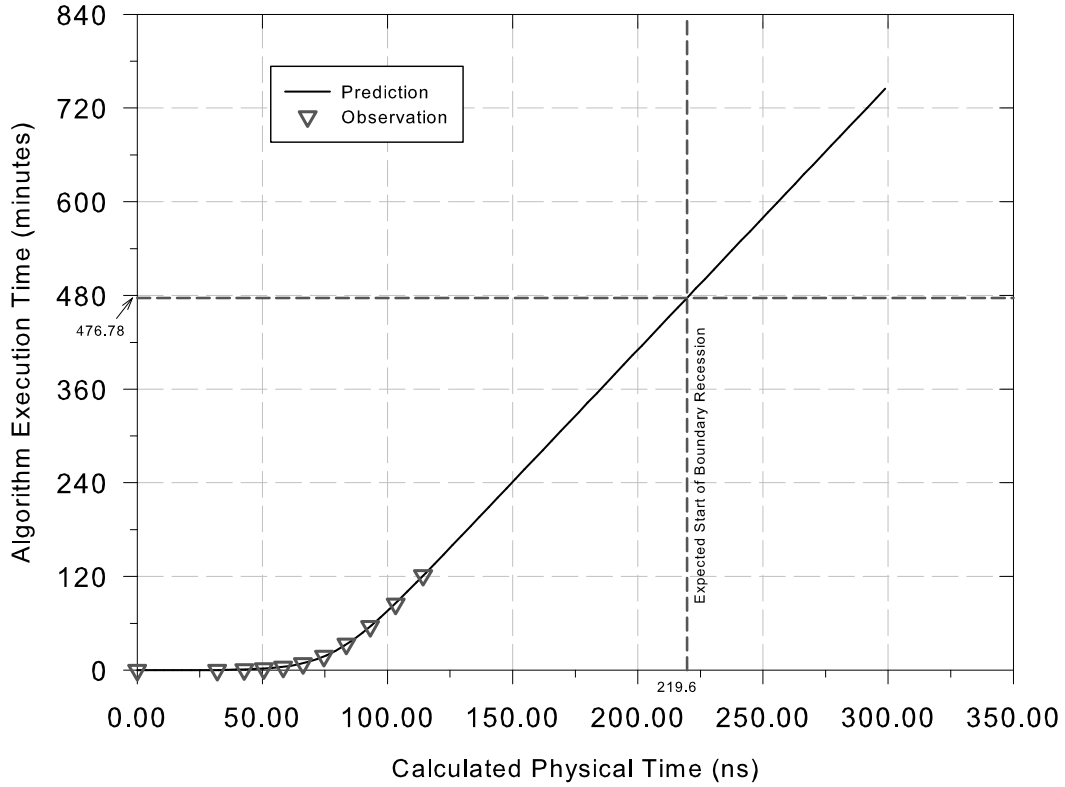


Figure 4.10: Estimated algorithm execution time to reach the point at which the boundary perturbation $\Delta s(t)$ becomes negative. Points marked “observation” were taken from the current Case.

trolling function) at the boundary allows the procedure to work without failure, and setting $\mu = 10$ causes the nodal density near the plasma boundary, and hence the effect of the calculated derivative $\hat{\rho}_\xi$, to be high. This can be seen in Figure 4.13, where the calculated physical potential, $\phi(x, t)$, across the acceleration region is shown at three different solution times. Nodal locations are highlighted by markers situated along each curve, and at the later time, these points coalesce towards the plasma boundary location to the left

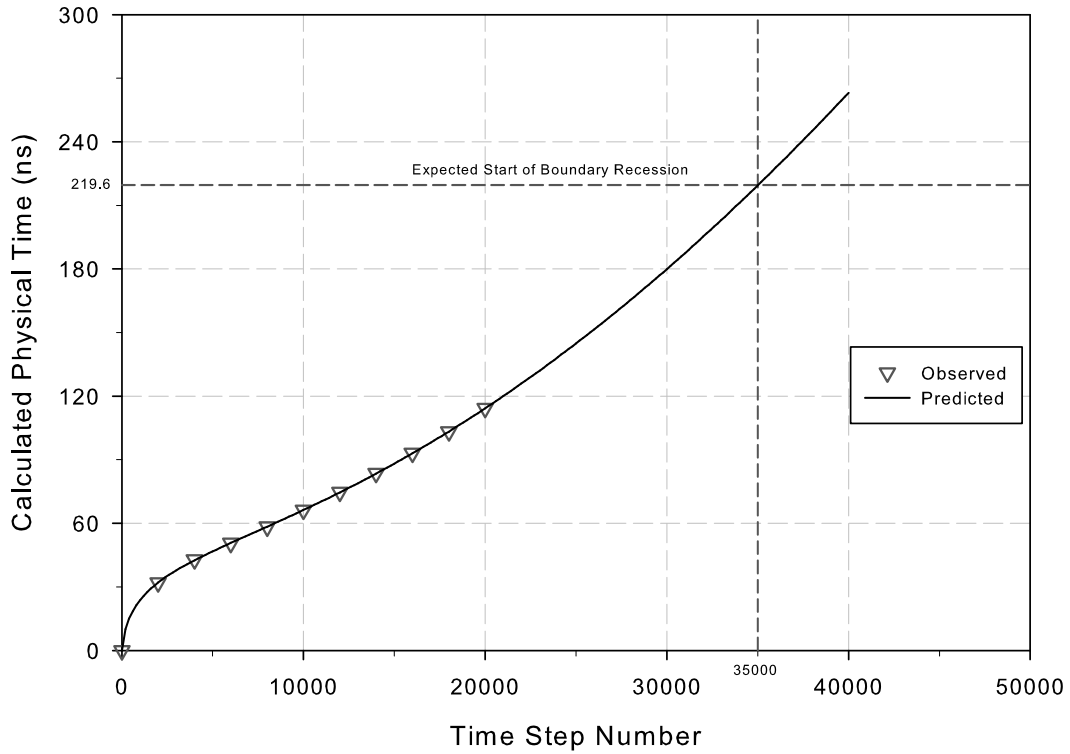


Figure 4.11: Estimated number of time-steps to reach the point at which the boundary perturbation $\Delta s(t)$ becomes negative. Points marked “observation” were taken from the current Case.

of the graph; this is a consequence of the spatial adaptive nodal density procedure.

A further demonstration of the adaptive procedure can be seen in Figures 4.14 and 4.15. Here, the locations of the first fifteen nodes, in physical space, are displayed as a function of time and the variation in physical nodal separation is displayed at varying solution times. In both graphs, nodes are

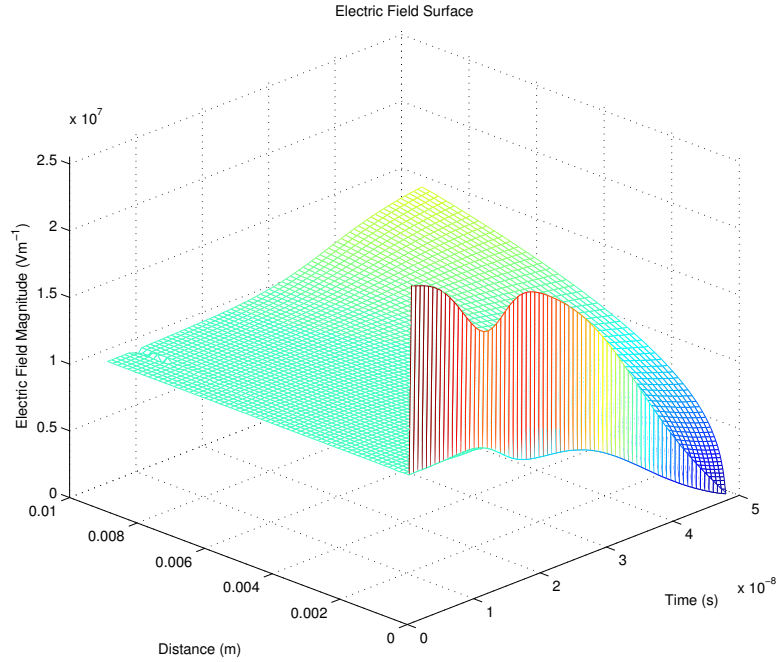


Figure 4.12: The electric field surface $E(x, t)$, with adaptive parameter $\mu = 100$ (region start size of $L = 0.009$ m). Output is shown at every 40 time steps.

initially equally spaced, seen to the left of Figure 4.14 and by the blue line in Figure 4.15, but as time progresses they become rapidly concentrated towards the plasma boundary location, again highlighting the adaptive nodal density controlling. In Figure 4.15, this is manifested at later times by the nodal separation rapidly decreasing towards node 1 at the left. Additionally, away from the plasma boundary at the left, the nodal spacing remains constant as a consequence of the function $\hat{\rho}_{\xi}^2(\xi, \tau)$, being effectively zero there (this is $\hat{f}(\xi, \tau)$ in (4.37)). The green (3.6ns) curve in Figure 4.15 shows some instability, although this decreases with time and has disappeared after a solution time of about 6ns.

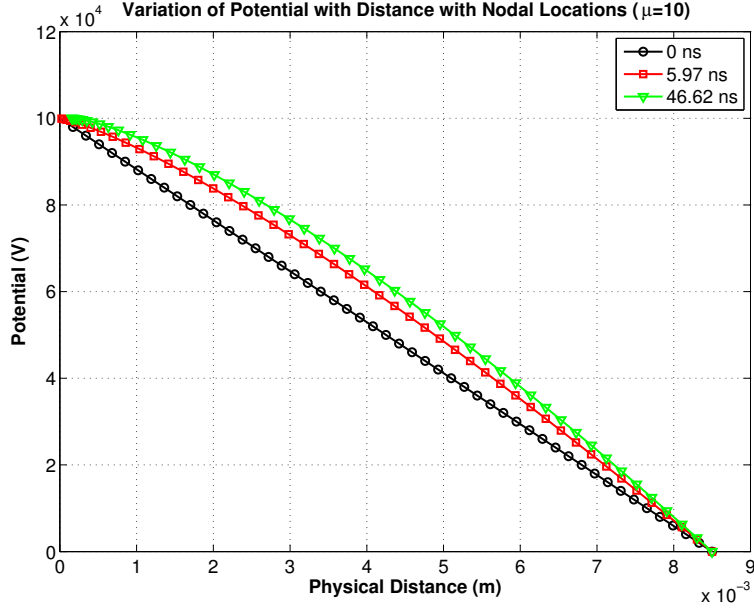


Figure 4.13: Variation in potential $\phi(x, t)$, with x at three specific times. Setting the adaptive parameter, μ , to be equal to ten leads to increased nodal density towards the left of the curves, as time increases.

4.3.2.7 Method 1 - Summary and Conclusion

Whilst the algorithm presented here offers an apparently viable solution, in that the advancing wavefront follows the analytic separation characteristic closely (See Figure 4.6, for example), in order to offer stability to the method the small, multiplicative parameter, δ , must be introduced into the plasma boundary calculation thus rendering the predicted boundary movement unphysical. Without such a parameter, the boundary movement calculated by (4.62) causes rapid failure of the numerical method, with this being due to the presence of $\tilde{E}_{\tilde{x}\tilde{x}}(\tilde{s}^k, \tilde{t}^k)$ on the denominator of (4.62). Particularly at early solution times, the calculated potential, $\tilde{\phi}(\tilde{x})$, across the solution re-

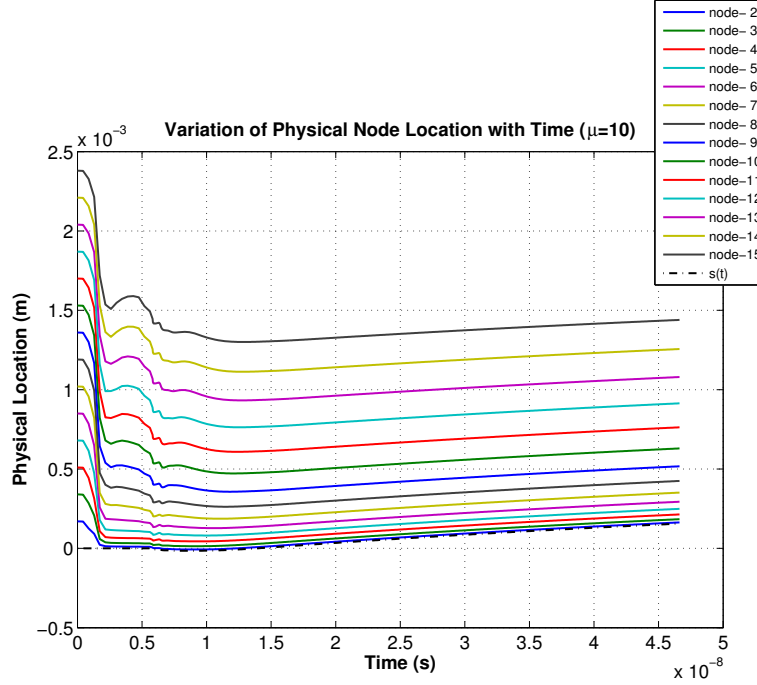


Figure 4.14: Variation in nodal location for the first fifteen nodes in physical space. Nodes rapidly move from an equally spaced distribution to being concentrated near the plasma boundary (where the charge density gradient is greatest).

gion has little curvature. Consequently, the term $\tilde{E}_{\tilde{x}\tilde{x}}(\tilde{s}^k, \tilde{t}^k)$, corresponding to the third derivative of the solution potential at the plasma boundary, is very small, in turn causing $\Delta\tilde{s}^k$ to be large. Such large changes in boundary location cause the solution region to become distended, with the consequent effect being that the mapping function, M , becomes large rendering the dimensionless, logical version of Gauss' law, (4.44), imbalanced at successive time steps; this is manifested as a rapid onset of instability within the numerical procedure, causing it to fail.

A further consequence of the necessity of δ is that the algorithm executes very slowly. Indeed, in order to examine the effects of an applied source

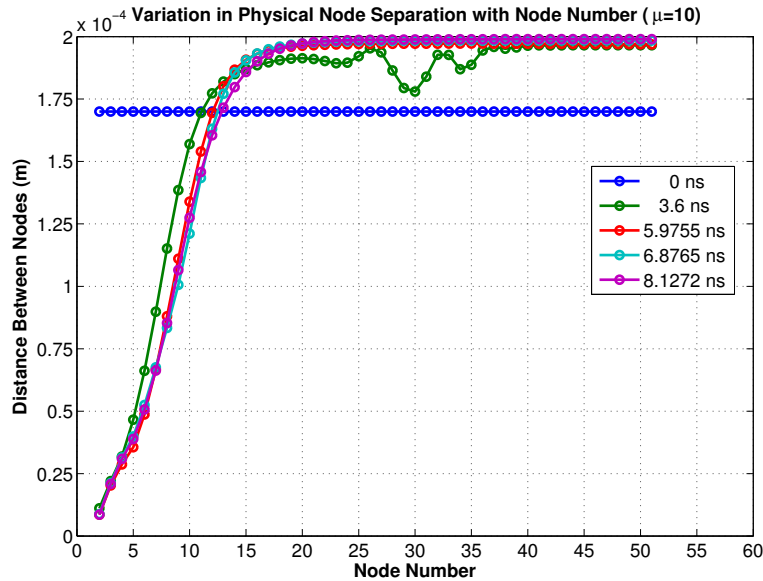


Figure 4.15: The variation in nodal separation with node number at different solution times. The ordinate value at node 2, for instance, refers to the distance $x_2^k - x_1^k$ (for time-step k).

charge density ramp that can be replicated at all by experiment, a relatively rapidly increasing ramp must be applied. Whilst this is (just about) experimentally viable, it is not typical of a normal neutron tube operation.

In order to avoid the issues within the first method, a new approach is now proposed, where an expression for the rate of change of boundary movement is determined in an entirely different way. This new approach does not suffer the same problems experienced here, and thus allows a more experimentally representative charge density profile to be applied within the model.

4.3.3 Numerical Method 2 for the Determination of the Time-dependent Solution

As mentioned above, a new approach to the time dependent problem has been developed to avoid the problems experienced in the original method; this is now described along with an associated time-stepping algorithm. We begin by first manipulating the original one-dimensional, dimensionless system of equations, (4.35), to reduce their number by one and then further manipulate the system to yield an analytic integral expression for the rate of change of dimensionless plasma boundary location, $\tilde{s}'(t)$. The approach is described as follows, beginning by first recalling (4.30) and (4.35a), which are

$$\tilde{E} = -\frac{\partial \tilde{\phi}}{\partial \tilde{x}},$$

and

$$\frac{\partial^2 \tilde{\phi}}{\partial \tilde{x}^2} = -\alpha_1 \tilde{\rho},$$

respectively.

By noting (4.30), we can integrate (4.35a) to observe that

$$\tilde{E}(\tilde{x}, \tilde{t}) = \alpha_1 \int_{\tilde{s}(\tilde{t})}^{\tilde{x}} \tilde{\rho}(\xi, \tilde{t}) \, d\xi, \quad (4.74)$$

using the condition, (4.36c). Then, substitution of (4.74) into (4.35b) gives rise to the coupled pair of equations,

$$\frac{\partial \tilde{v}}{\partial \tilde{t}} = \frac{\alpha_1}{2} \int_{\tilde{s}(\tilde{t})}^{\tilde{x}} \tilde{\rho}(\xi, \tilde{t}) \, d\xi - \tilde{v} \frac{\partial \tilde{v}}{\partial \tilde{x}}, \quad (4.75a)$$

$$\frac{\partial \tilde{\rho}}{\partial \tilde{t}} = -\frac{\partial(\tilde{\rho}\tilde{v})}{\partial \tilde{x}}, \quad (4.75b)$$

for the dependent variables $\tilde{\rho}(\tilde{x}, \tilde{t})$ and $\tilde{v}(\tilde{x}, \tilde{t})$, with the boundary condition, (4.36c), being used in (4.74).

An expression for the rate of change of plasma boundary location, $\tilde{s}'(\tilde{t})$, can also be determined by initially integrating (4.74), over the solution domain, giving

$$\begin{aligned} \int_{\tilde{s}(\tilde{t})}^{\tilde{x}_T} \tilde{\phi}_{\tilde{x}} \, d\tilde{x} &= \tilde{\phi}_T - \tilde{\phi}_S \\ &= -\alpha_1 \int_{\tilde{s}(\tilde{t})}^{\tilde{x}_T} \int_{\tilde{s}(\tilde{t})}^{\tilde{x}} \tilde{\rho}(\xi, \tilde{t}) \, d\xi \, d\tilde{x} \\ &= -\alpha_1 \int_{\tilde{s}(\tilde{t})}^{\tilde{x}_T} (\tilde{x}_T - \tilde{x}) \tilde{\rho}(\tilde{x}, \tilde{t}) \, d\tilde{x}, \end{aligned} \quad (4.76)$$

by the *replacement lemma* ([38], p6).

Taking the time derivative of (4.76), we find

$$\begin{aligned} 0 &= -\alpha_1 \frac{\partial}{\partial \tilde{t}} \int_{\tilde{s}(\tilde{t})}^{\tilde{x}_T} (\tilde{x}_T - \tilde{x}) \tilde{\rho}(\tilde{x}, \tilde{t}) \, d\tilde{x} \\ &= -\alpha_1 \left\{ \int_{\tilde{s}(\tilde{t})}^{\tilde{x}_T} (\tilde{x}_T - \tilde{x}) \frac{\partial \tilde{\rho}}{\partial \tilde{t}} \, d\tilde{x} - (\tilde{x}_T - \tilde{s}(\tilde{t})) \tilde{\rho}_s \tilde{s}'(\tilde{t}) \right\}, \end{aligned} \quad (4.77)$$

by Leibnitz Integral Rule ([36]), and since

$$-\frac{\partial(\tilde{\rho}\tilde{v})}{\partial \tilde{x}} = \frac{\partial \tilde{\rho}}{\partial \tilde{t}},$$

from (4.35c), the integral on the right hand side of (4.77) can be expanded, giving

$$\begin{aligned} \int_{\tilde{s}(\tilde{t})}^{\tilde{x}_T} (\tilde{x}_T - \tilde{x}) \frac{\partial \tilde{\rho}}{\partial \tilde{t}} \, d\tilde{x} &= (\tilde{x}_T - \tilde{x}) \tilde{\rho}\tilde{v} \Big|_{\tilde{s}(\tilde{t})}^{\tilde{x}_T} - \int_{\tilde{s}(\tilde{t})}^{\tilde{x}_T} (\tilde{\rho}\tilde{v}) \, d\tilde{x} \\ &= (\tilde{x}_T - \tilde{s}(\tilde{t})) \tilde{\rho}_s \tilde{s}'(\tilde{t}). \end{aligned} \quad (4.78)$$

Evaluating the boundary term on the right of (4.78), we arrive at the equation

$$\tilde{s}'(\tilde{t}) = \tilde{v}_i - \frac{1}{\tilde{\rho}_s(\tilde{x}_T - \tilde{s}(\tilde{t}))} \int_{\tilde{s}(\tilde{t})}^{\tilde{x}_T} (\tilde{\rho}\tilde{v}) \, d\tilde{x} \quad (4.79)$$

for the rate of change of dimensionless plasma boundary location at \tilde{t} .

4.3.3.1 Detailed Numerical Algorithm

The equations, (4.75), in addition to (4.79) can now be used in a time stepping algorithm for the determination of the solution of the time-dependent plasma boundary problem in one dimension. The new proposed algorithm is as follows:

Step 1 The initial solution region is set with the initial plasma boundary location being defined as $\tilde{s}(0) = \tilde{s}_0$;

Step 2 Set $\tilde{\rho}(\tilde{x}, 0) = \tilde{v}(\tilde{x}, 0) = 0$, where $\tilde{x} \in (\tilde{s}, \tilde{x}_T]$;

Step 3 Set $\tilde{\rho}(\tilde{s}, \tilde{t}) = \tilde{\rho}_s(\tilde{t})$ and $\tilde{v}(\tilde{s}, \tilde{t}) = \tilde{v}_i$, from (4.36d) and (4.36f), where $\tilde{\rho}_s(\tilde{t})$ is the dimensionless time-dependent function (in this case given by the ramped function, (4.56)) representing the time-dependent variation in current density at the plasma boundary during tube operation, and \tilde{v}_i the initial dimensionless particle velocity (a constant in this case, although not necessarily so);

Step 4 Calculate the updated velocity field, $\tilde{v}(\tilde{x}, \tilde{t}^{k+1})$, from (4.75a), using the current velocity field, $\tilde{v}(\tilde{x}, \tilde{t}^k)$, and the current charge density field, $\tilde{\rho}(\tilde{x}, \tilde{t}^k)$. This is done by discretising (4.75a) as

$$\tilde{v}_j^{k+1} = \tilde{v}_j^k + \Delta\tilde{t} \left\{ \frac{\alpha_1}{2} \int_{\tilde{s}^k}^{\tilde{x}_j^k} \tilde{\rho}^k d\tilde{x} - \tilde{v}_j^k \left(\frac{\partial \tilde{v}_j^k}{\partial \tilde{x}} \right) \right\},$$

where the integral is approximated by the trapezium rule,

$$\int_{\tilde{s}^k}^{\tilde{x}_j^k} \tilde{\rho}^k d\tilde{x} \approx \frac{\Delta\tilde{x}^k}{2} \left\{ (\tilde{\rho}_s^k + \tilde{\rho}_j^k) + 2 \sum_{i=2}^{j-1} \tilde{\rho}_i^k \right\},$$

with $\Delta\tilde{x}^k$ being the nodal spacing at t^k . Here, the spatial derivative $\partial\tilde{v}_j^k/\partial\tilde{x}$ is approximated by the first order difference

$$\frac{\partial\tilde{v}_j^k}{\partial\tilde{x}} \approx \frac{\tilde{v}_j^k - \tilde{v}_{j-1}^k}{\Delta\tilde{x}^k}.$$

Step 5 Calculate the updated charge density field, $\tilde{\rho}(\tilde{x}, \tilde{t}^{k+1})$, from (4.75b), using $\tilde{\rho}(\tilde{x}, \tilde{t}^k)$, and $\tilde{v}(\tilde{x}, \tilde{t}^{k+1})$ from Step 4. This is done by discretising (4.75b) as

$$\tilde{\rho}_j^{k+1} = \tilde{\rho}_j^k - \Delta\tilde{t} \frac{\partial(\tilde{\rho}_j^k \tilde{v}_j^{k+1})}{\partial\tilde{x}}.$$

Here, the spatial derivative $\partial(\tilde{\rho}_j^k \tilde{v}_j^{k+1})/\partial\tilde{x}$ is approximated by the first order difference

$$\frac{\partial\tilde{\rho}_j^k \tilde{v}_j^{k+1}}{\partial\tilde{x}} \approx \frac{\tilde{\rho}_j^k \tilde{v}_j^{k+1} - \tilde{\rho}_{j-1}^k \tilde{v}_{j-1}^{k+1}}{\Delta\tilde{x}^k}.$$

Step 6 Determine the rate of change of boundary movement at the current time-step, t^k . This is done by evaluating

$$\frac{d\tilde{s}^k}{dt} \approx \tilde{v}_i - \frac{\Delta\tilde{x}^k \left\{ \frac{1}{2} (\tilde{\rho}_s^k \tilde{v}_i + \tilde{\rho}_{n+1}^k \tilde{v}_{n+1}^{k+1}) + \sum_{j=2}^n \tilde{\rho}_j^k \tilde{v}_j^{k+1} \right\}}{\tilde{\rho}_s^k (\tilde{x}_T - \tilde{s}^k)}, \quad (4.80)$$

from (4.79), where $\tilde{s}^k = \tilde{s}(t^k)$. Here, the integral on the right hand side of (4.79) has been approximated in (4.80) by the trapezium rule, as in Step 4. An approximation to the boundary location at the $(k+1)^{\text{th}}$ time step can then be written

$$\tilde{s}^{k+1} \approx \tilde{s}^k + \Delta\tilde{t} \frac{d\tilde{s}^k}{dt};$$

Step 7 Return to step (4) and repeat until the solutions in successive time steps are identical to within a small tolerance.

4.3.3.2 Test Case

To test the new method, the physical conditions listed at the start of §4.3, above, were applied. As in the previous method the potential difference applied across the solution region was held constant in time, with particles emerging with a constant initial velocity (or energy). As a consequence of a significant increase in computational speed, a source charge density ramp that is more typical of experiment could be used and this is detailed as follows.

Source Charge Density Ramp. Owing to long algorithm execution times, in order to have any realistic representation of experiment the previous model used a source charge density ramp whose rate of increase was rapid enough that the effects of the ramp could be captured within a reasonable computational time frame. Such a rapidly increasing source charge density is at the short end of the experimental time frame, and is not typical of neutron tube operation. The new method presented here overcomes difficulties experienced in the previous case and so to test it, a more typically representative charge density ramp is applied here. Again, referring to the function (4.56) shown in Figure 4.3, the constants b , c , and h are chosen to be

$$b = 5.41 \times 10^6 \text{ s}^{-1},$$

$$c = 2 \times 10^{-7} \text{ s}$$

$$h = \rho_m,$$

where ρ_m is given by (4.73). These parameters cause a ramp rise time of ~ 114.4 non-dimensional units, or 370 ns; the value $t_m = 3.232$ ns follows from (4.28) and (4.29) (with $L = 0.01\text{m}$ from Table 4.2).

4.3.3.3 Results

The application of the physical conditions, including the more representative, longer timescale charge density ramp in addition to a logical time-step size of 4.64×10^{-3} non-dimensional units (corresponding to ~ 215 non-dimensional time steps per unit t_m , or an initial physical time step of 1.5×10^{-11} s) and a total time of 900ns, yielded results with a number of differing features; some of the more salient features are explained in the following paragraphs. Other parameters used are listed in Table 4.2, below, where it is noted that the adaptive features incorporated in method 1 are not implemented here. The algorithm executed to completion within a time frame that was of the order of minutes, rather than hours (as in the original algorithm). The pa-

Parameter	Value	Description
m	60000	Number of time steps.
n	75	Initial number of spatial steps.
$d\tau$	4.64×10^{-3} units	Logical time step size.
L	0.01 m	Region start size - final run.
t_{end}	900×10^{-9} s	Calculation termination physical time.

Table 4.2: Numerical parameters for the one-dimensional time-dependent numerical method 2 test problem.

rameters chosen allow a solution showing convergence towards the analytic steady-state solution to be generated, with the calculated location of the plasma boundary clearly asymptoting towards the steady state location; the

accuracy of the final solution increases with increasing numbers of spatial nodes. The time step size was chosen to facilitate this for differing numbers of spatial nodes without violating the CFL condition, (4.63) (which is also applicable in this case). Initially, 75 spatial nodes were used, with this number increasing in steps of 25 to 150 nodes. At the final solution time of $0.9\mu\text{s}$, a typical neutron tube source will have undergone switch-on with the source charge density being approximately constant at this time.

The following Figures detail features from the calculated solution, where results are displayed in physical space.

Figure 4.16 shows the surface $\rho(x, t)$, where the charge density ramp, increasing from right to left, is clearly visible. There is no obvious instability. Figure 4.17 shows level curves of charge density for the entire calculated solution. The plasma boundary is identified by the solid black line to the left of the Figure, where it can be seen that boundary movement begins immediately. The entire solution region is charge infused within ~ 7 ns.

Figure 4.18 shows the surface $\phi(x, t)$ (extracted from $\tilde{\rho}(\tilde{x}, t)$ via (4.35a) and re-dimensionalised). The change in plasma boundary location (at the top of the surface) with time (increasing from left to right) is visible, as is the gradual change in curvature of the potential across the solution region from the initial, linear solution at $t = 0$ (to the left of the surface) to the final curved solution at $t = 900\text{ns}$ (at the right of the surface). To examine the final solution, it is displayed in Figure 4.19 as the solid black line; it is surrounded by red circular markers, which represent the analytic steady-state

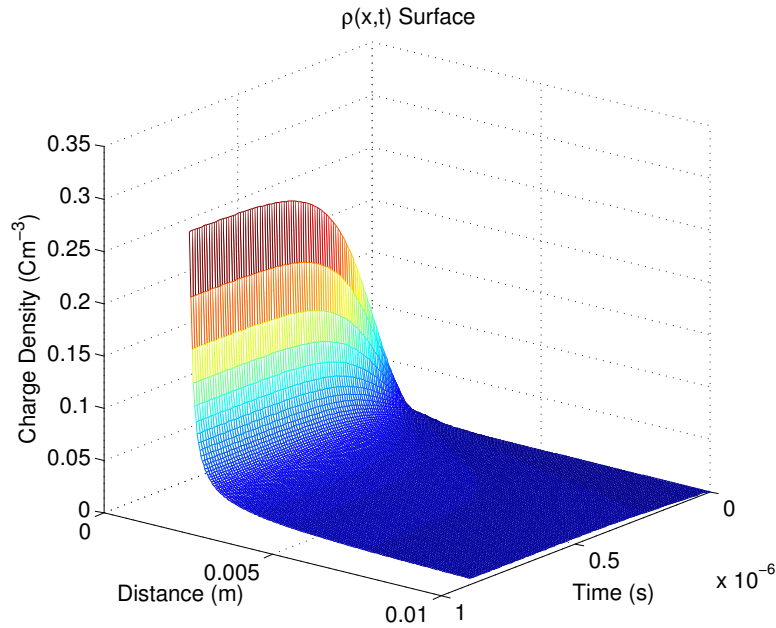


Figure 4.16: The charge density surface $\rho(x, t)$. Output is shown at every 600 time steps.

solution (extracted from (3.28)). The two curves (black line and markers) appear very close together, and so to further investigate the accuracy of the final time-dependent solution, a number of calculations were performed with differing numbers of nodes. For each calculation, the final calculated time-dependent potential solution (at $t = 900\text{ns}$) was compared to the exact steady-state solution calculated at the same nodal point locations (again using (3.28)). The error in calculated final solution (as a percentage of the maximum potential value, ϕ_m) for each of these calculations is shown in Figure 4.20. Here, it can be seen that the calculated solution error decreases with increasing numbers of nodes. It can also be seen that the largest error in solution occurs towards the plasma boundary (to the left of the graph)

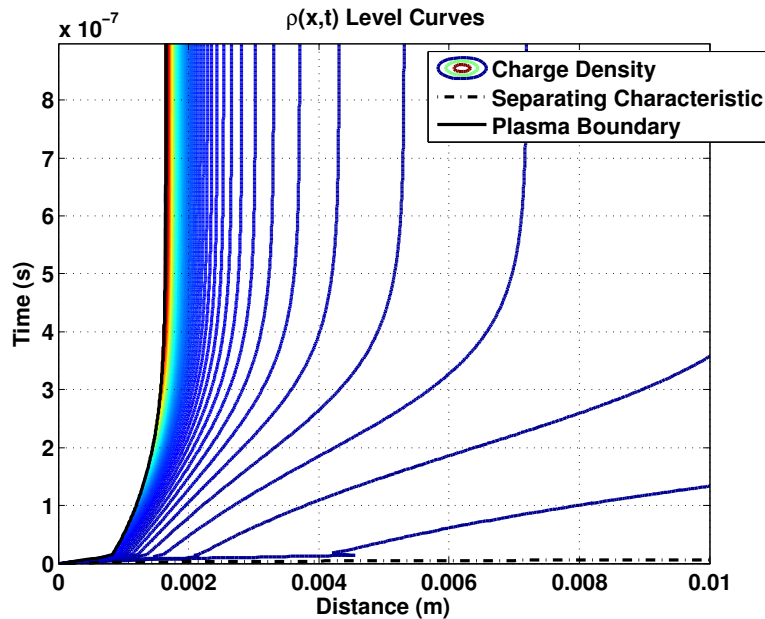


Figure 4.17: Equally spaced level curves of constant charge density for the entire solution (up to $0.9\mu\text{s}$).

where the solution curvature is at its greatest; this is to be expected and would be reduced if an adaptive scheme, such as that used in method 1, were used here. As expected, the error in the calculated solution is zero at the fixed target location to the right of Figure 4.20.

Finally, Figures 4.21 and 4.22 show the calculated boundary location and perturbation as functions of time. Figure 4.21 clearly shows the time dependent boundary, $s(t)$, asymptoting to the analytic steady-state plasma boundary location, with Figure 4.22 showing the boundary perturbation asymptoting to zero with time.

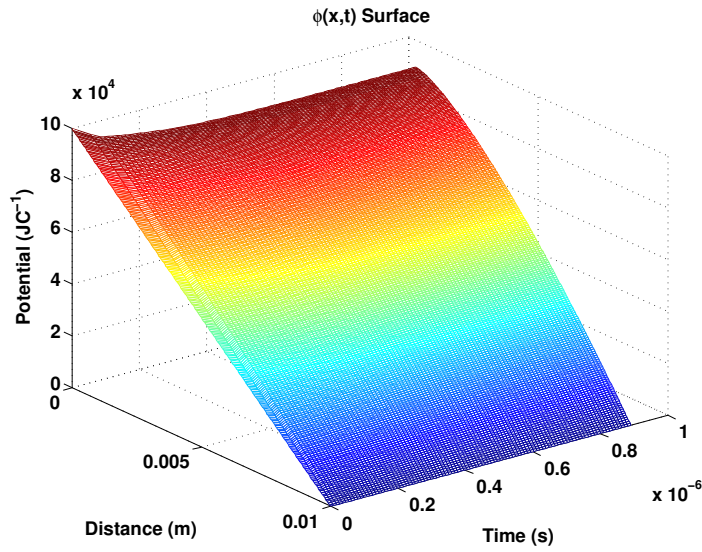


Figure 4.18: The potential surface $\rho(x, t)$. Output is shown at every 600 time steps.

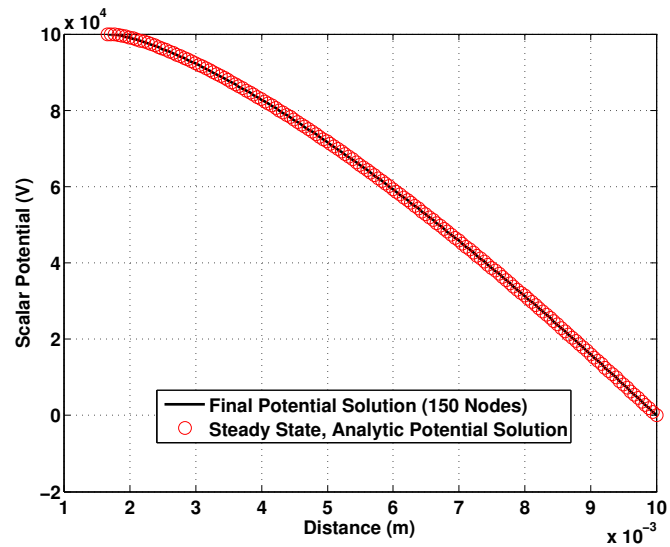


Figure 4.19: The analytic steady-state solution (red circles) with the calculated potential solution $\phi(x, t)$ at $t = 900\text{ns}$ (black solid line with 150 nodes).

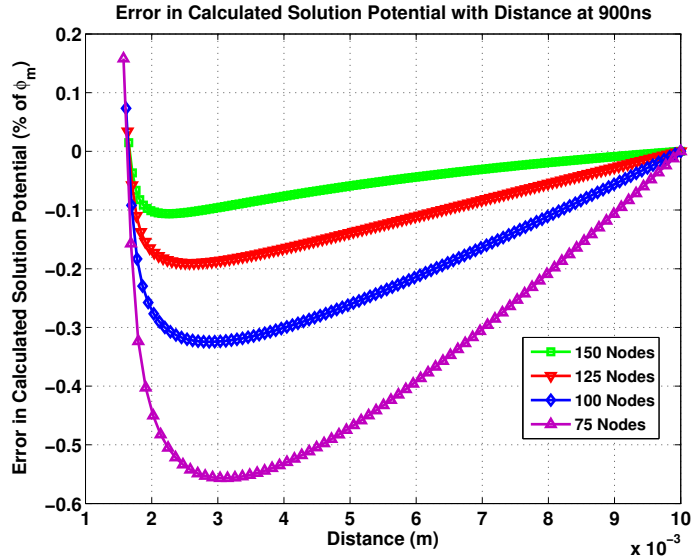


Figure 4.20: Error in final calculated solution potential as a function of distance. The error is calculated as $\text{error}\% = \frac{100 \times (\phi(x, t_e) - \phi_a(x))}{\phi_m}$, where t_e is the final time (900ns in this case) and $\phi_a(x)$ is the analytic steady-state solution.

4.3.3.4 Method 2 - Summary and Conclusion

The new approach detailed here, for the solution of the one-dimensional time-dependent problem, avoids solving Gauss' Law, (4.1c), numerically, which, in combination with the method used for the determination of the plasma boundary perturbation, is believed to be the source of the instability observed in the original method. Furthermore, a more robust, analytically based method for determining the plasma boundary location has been developed.

The new approach has been implemented as a numerical time-stepping scheme using MATLAB, and has been tested by applying conditions typically seen in a neutron tube application; this was barely possible with the original

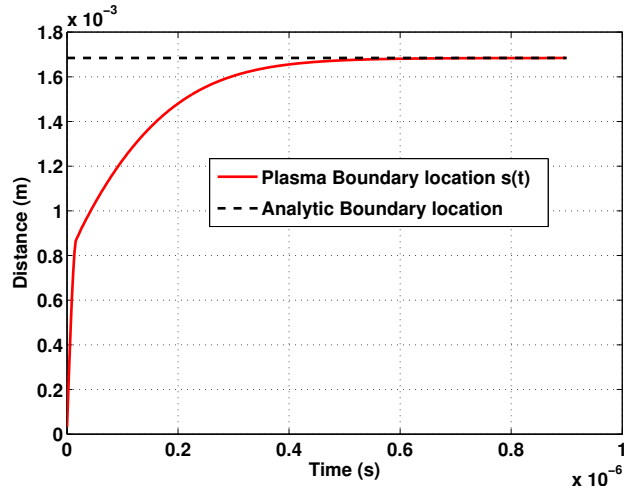


Figure 4.21: The variation in boundary location, $s(t)$, with time. The calculated boundary asymptotes to the analytic steady-state location as the source charge density ramp reaches its maximum value.

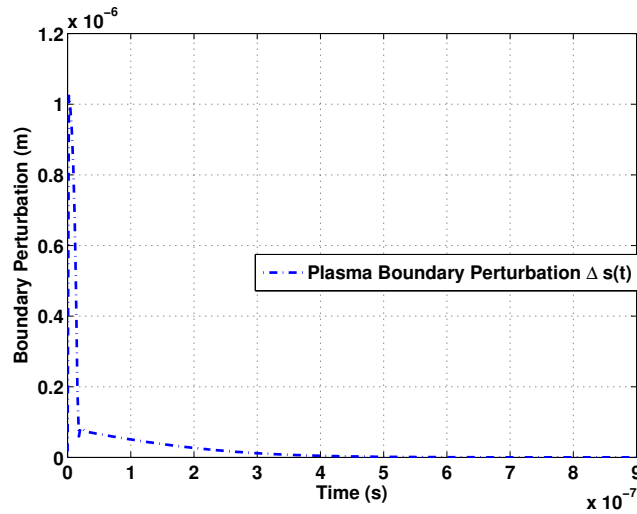


Figure 4.22: The variation in boundary perturbation, $\Delta s(t)$, with time. The perturbation, calculated from (4.79), asymptotes to zero as the source charge density ramp reaches its maximum value.

method, as a consequence of slow execution times. Results clearly indicate that, in this case, as the source charge density ramp settles to its peak height, time dependent solutions converge towards the analytic steady-state solution, as would be expected. The calculated plasma boundary location is seen to clearly converge upon the steady state plasma boundary location.

4.4 Summary and Conclusion to the One-dimensional Time-dependent Problem

Several attempts have been made at solving the one-dimensional system, (4.1) (subject to the conditions, (4.2)), with varying degrees of success. The problem was initially attacked analytically, yielding a solution that is valid in the charge free region separated from the charge infused region by a particular characteristic curve. Further analysis has also yielded the form of an analytic solution in the charge infused region, to within constants, although the determination of the constants appears difficult.

A first numerical approach, whereby the system, (4.1), is transformed to a fixed, logical grid (as a consequence of the physical solution region being time-dependent), upon which it is discretised in a standard way using finite differences, yielded an apparently viable solution. However, in order for the method to proceed without instability, an unphysical scaling parameter was introduced, dramatically reducing the the boundary movement at each time-step and causing the method to proceed very slowly. It was concluded that the unphysical nature of the calculated boundary movement was not acceptable and so a new method was devised to circumvent the difficulties.

The new method removed the observed source of difficulty by integrating Gauss' Law (as in (4.74)), and incorporating it into the Lorentz force equation, thus reducing the system of equations by one to the pair, (4.75). A different method for determining the boundary movement was also determined, and this was done by again integrating Gauss' Law. Manipulation of this, whilst utilising the continuity equation, (4.75b), yields the expression, (4.79), for the boundary velocity; the boundary movement at each time-step is determined from this expression.

We now move on to the more difficult two-dimensional case, where a method is proposed for the determination of the two-dimensional steady state solution. This method is based upon the more successful second one-dimensional numerical method, and splits the Lorentz, vector equation, (2.17a), into its two components, solving each one separately in alternating directions.

Chapter 5

A Planar Two-dimensional Steady-state Solution

One of the key assumptions within the study of the one-dimensional problem was that, within the acceleration region of a neutron tube, particle acceleration due to magnetic fields can be disregarded. As a result of the study of the one-dimensional time-dependent problem, an approach to the two-dimensional steady-state problem is now proposed. The proposed solution strategy has been implemented, giving results that are entirely plausible and which show convergence, with a little further work being required to perfect the method.

Within this chapter, we seek a two-dimensional steady-state solution to the plasma boundary problem introduced in §2.3, by solving the system of time-dependent equations, (2.17), on the region shown in Figure 2.3 (which is reproduced here for convenience and labelled Figure 5.1), with time being used in a pseudo manner (it not representing actual time) to advance an iterative method.

It is pointed out that the strategy adopted in this chapter calculates the deuteron beam entirely within the solution region. This is in contrast to the alternative approach of solving only within the beam itself, where the edge of the beam (which would correspond to the edge of the domain) would represent a free boundary. This discarded alternative is potentially more difficult, because of the need to locate a second moving boundary that represents the edge of the beam.

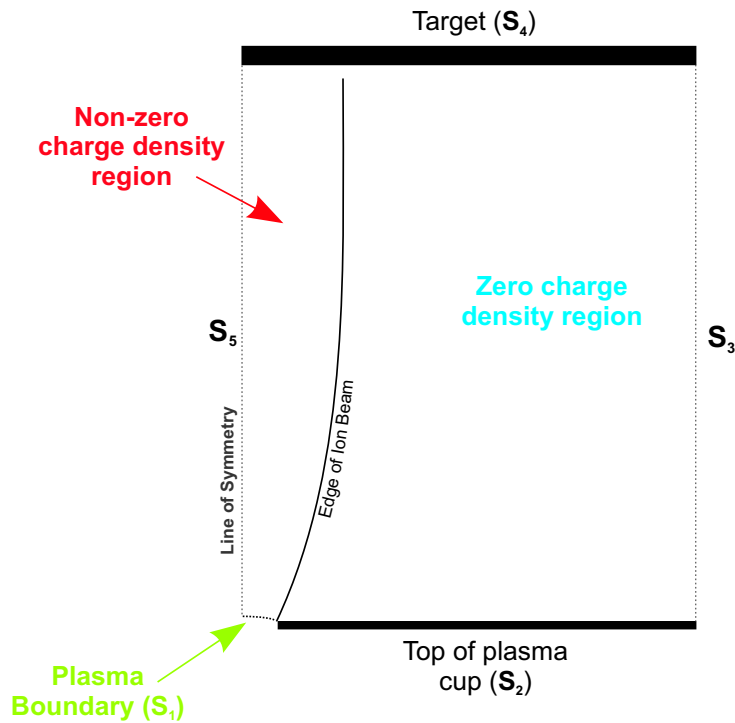


Figure 5.1: Region of interest, \mathbf{R} . The curved line is a representation of the edge of the ion beam, and separates the zero and non-zero charge density regions.

5.1 Two-dimensional Time-dependent System

In order to develop the two-dimensional steady-state solution to the plasma boundary problem, we firstly restate the original simplified (neglecting magnetic effects) system of equations as

$$m \left\{ (\mathbf{v} \cdot \nabla) \mathbf{v} + \frac{\partial \mathbf{v}}{\partial t} \right\} = q \mathbf{E}, \quad (5.1a)$$

$$\nabla \cdot (\rho \mathbf{v}) = -\frac{\partial \rho}{\partial t}, \quad (5.1b)$$

$$\nabla \cdot \nabla \phi = -\frac{\rho}{\epsilon_0}, \quad (5.1c)$$

and

$$\mathbf{E} = -\nabla \phi, \quad (5.1d)$$

from (2.17) and (2.18), where $t \geq 0$, say, and where the constants q , m , and ϵ_0 , along with the dependent and independent variables, are as defined in §2.1 and §2.3.1. We then write this system in a two-dimensional Cartesian form, utilising the fact that the electric field can be written as an integral, from (5.1d) and (5.1c), as in §4.3.3.

The time dependence within this system is to be used to iterate towards a steady-state solution on the planar region shown in Figure 5.1 (which is symmetric about the vertical axis). The system is solved in conjunction with appropriate extensions to two dimensions of the conditions (2.20) given in §2.3.2, namely

$$\phi(\mathbf{x}, t) = \phi_S, \quad t \geq 0, \mathbf{x} \in S_1 \cup S_2 \quad (5.2a)$$

$$\phi(\mathbf{x}, t) = \phi_T, \quad t \geq 0, \mathbf{x} \in S_4 \quad (5.2b)$$

$$\nabla \phi(\mathbf{x}, t) \cdot \mathbf{n}_1 = 0, \quad t > 0, \mathbf{x} \in S_1 \quad (5.2c)$$

$$\nabla \phi(\mathbf{x}, t) \cdot \mathbf{n}_5 = 0, \quad t > 0, \mathbf{x} \in S_5 \quad (5.2d)$$

$$\rho = \rho_s(\mathbf{x}), \quad t \geq 0, \mathbf{x} \in S_1 \quad (5.2e)$$

$$\rho = 0, \quad t \geq 0, \mathbf{x} \in S_2, \quad (5.2f)$$

$$\rho = 0, \quad t = 0, \mathbf{x} \in \mathbf{R}, \mathbf{x} \notin S_1 \cup S_2, \quad (5.2g)$$

$$\nabla \rho(\mathbf{x}, t) \cdot \mathbf{n}_5 = 0, \quad t > 0, \mathbf{x} \in S_5 \quad (5.2h)$$

$$\mathbf{v} = v_i(\mathbf{x})\mathbf{n}_1, \quad t \geq 0, \mathbf{x} \in S_1 \quad (5.2i)$$

$$\mathbf{v} = \mathbf{0}, \quad t = 0, \mathbf{x} \in \mathbf{R}, \mathbf{x} \notin S_1 \quad (5.2j)$$

$$\mathbf{v} \cdot \mathbf{n}_5 = 0, \quad t > 0, \mathbf{x} \in S_5 \quad (5.2k)$$

where $\{S_i\}$ are the boundary segments enclosing the region \mathbf{R} , shown in Figure 5.1. Here, S_1 is the (moving) plasma boundary, S_2 is the top of the plasma cup (held at the same electric scalar potential as the plasma boundary, (5.2a)), and S_4 is the target (held at the constant electric scalar potential (5.2b)). As explained in §2.3.2, the condition (5.2c) indicates that the electric field normal to the plasma boundary is zero, which implies that the electric field at the boundary is zero, since the electric field tangential to the boundary surface must be zero as a consequence of (5.2a).

The condition (5.2i) indicates that particle release speed is a function of spatial location only, and that particles are released in a direction normal to the plasma boundary surface (§2.3.2), whilst the condition (5.2e) indicates that the charge density at the plasma boundary surface is also a function in spatial location only; it is zero, (5.2f), on the metal plasma cup. These conditions are appropriate for the steady-state case. The conditions, (5.2j) and (5.2g), indicate that the region is initially charge free, and the final conditions, (5.2d), (5.2h) and (5.2k) state that there is no change in ϕ and ρ across the line of symmetry, S_5 , in addition to there being no velocity into

the boundary.

In this case, the vector $\mathbf{x} = \{x, y\}$ is the vector of independent variables, where $x \in [0, x_R]$, and where $y \in [0, y_T]$. The right hand boundary segment S_3 is located at (x_R, y) , and the segment S_4 is located at (x, y_T) . Clearly x_R must be sufficiently far away from S_1 that the beam, which is inclined to expand as it traverses the domain as a consequence of mutual charge repulsion within it, that it does not strike S_3 .

5.1.1 Two-dimensional Cartesian Form

To write the system of equations, (5.1), in a Cartesian form suitable for the solution strategy proposed in this chapter, we initially select the y axis to be parallel to the axis of symmetry in Figure 5.1, and then proceed to simplify the Lorentz equation, (5.1a). A simplification can be achieved by setting $\mathbf{p} = \mathbf{q} = \mathbf{v}$ in the vector identity

$$\nabla(\mathbf{p} \cdot \mathbf{q}) = (\mathbf{p} \cdot \nabla)\mathbf{q} + (\mathbf{q} \cdot \nabla)\mathbf{p} + \mathbf{p} \times (\nabla \times \mathbf{q}) + \mathbf{q} \times (\nabla \times \mathbf{p})$$

(see [29]), and writing (after rearranging)

$$\begin{aligned} (\mathbf{v} \cdot \nabla)\mathbf{v} &= \frac{1}{2}\nabla(\mathbf{v} \cdot \mathbf{v}) - \mathbf{v} \times (\nabla \times \mathbf{v}) \\ &= \frac{1}{2}\nabla(\mathbf{v} \cdot \mathbf{v}), \end{aligned} \tag{5.3}$$

since the assumption has been made that there are no magnetic effects and hence no vorticity exists within the particle flow (i.e. $\nabla \times \mathbf{v} = 0$). Substituting (5.1d) and (5.3) into (5.1a) gives

$$\frac{1}{2}\nabla(\mathbf{v} \cdot \mathbf{v}) + \left(\frac{\partial \mathbf{v}}{\partial t}\right) = -\frac{q}{m}\nabla\phi, \tag{5.4}$$

where for an iterative scheme to determine the steady-state solution, we could neglect the time dependence in velocity (using the time dependence in (5.1b) to progress the scheme), thus allowing (5.4) to be integrated to give

$$\begin{aligned}\frac{1}{2}|\mathbf{v}|^2 &= \frac{1}{2}(v_x^2 + v_y^2) \\ &= -\frac{q}{m}\phi + c_1,\end{aligned}\tag{5.5}$$

where v_x and v_y are the x and y components of the velocity vector, \mathbf{v} , respectively. The constant c_1 can be determined by noting that $\phi = \phi_S$ when $|\mathbf{v}| = v_i$ (on S_1), from (5.2a) and (5.2i). In practice, however, (5.5) proves difficult to use, particularly at early stages within the calculation, since the extraction of v_x , say, from it often gives complex results. As such, it is preferable to split (5.4) into its two Cartesian components,

$$v_x \frac{\partial v_x}{\partial x} + v_y \frac{\partial v_y}{\partial x} + \frac{\partial v_x}{\partial t} = -\frac{q}{m} \frac{\partial \phi}{\partial x},$$

and

$$v_x \frac{\partial v_x}{\partial y} + v_y \frac{\partial v_y}{\partial y} + \frac{\partial v_y}{\partial t} = -\frac{q}{m} \frac{\partial \phi}{\partial y}.$$

At this point, we can determine integral expressions for the right hand sides of (5.6) in a similar manner to the one-dimensional formulation given in §4.3.3.

By considering (5.1c) in two-dimensional Cartesian form and rearranging, we can write

$$\phi_{xx}(x, y) = -\left(\frac{\rho(x, y)}{\epsilon_0} + \phi_{yy}(x, y)\right),\tag{5.7}$$

where, by integrating (5.7) for a given y_0 location within the region, we can either write

$$\begin{aligned} \int_{s_x}^x \phi_{xx}(x, y_0) \, d\xi &= \phi_x(x, y_0) \\ &= - \int_{s_x}^x \left(\frac{\rho(x, y_0)}{\epsilon_0} + \frac{\partial^2 \phi}{\partial y^2} \Big|_{x, y_0} \right) \, d\xi, \quad 0 \leq y_0 \leq s_h, \end{aligned}$$

where s_x is the x location of the plasma boundary at y_0 , and where s_h is the maximum height of the plasma boundary above the source cup, or

$$\begin{aligned} \int_0^x \phi_{xx}(x, y_0) \, d\xi &= \phi_x(x, y_0) \\ &= - \int_0^x \left(\frac{\rho(x, y_0)}{\epsilon_0} + \frac{\partial^2 \phi}{\partial y^2} \Big|_{x, y_0} \right) \, d\xi, \quad s_h < y_0 \leq y_T, \end{aligned}$$

where $x = 0$ corresponds to the symmetry line to the left of Figure 5.1, with y_T being the target height (the height of the boundary S_4). Within both of these expressions, the value of $\phi_x(x, y_0)$, evaluated at the lower integration limit, is zero. This is since $\mathbf{E}(s_x)$ and hence $\phi_x(s_x, y_0) = 0$ on the plasma boundary itself and also $\phi_x(0, y_0) = 0$ on the symmetry line (S_5) from (5.2d).

A pair of analogous expressions for integration in the y direction can also be written down for a given x_0 location, and these are

$$\begin{aligned} \int_{s_y}^y \phi_{yy}(x_0, y) \, d\eta &= \phi_y(x_0, y) \\ &= - \int_{s_y}^y \left(\frac{\rho(x_0, y)}{\epsilon_0} + \frac{\partial^2 \phi}{\partial x^2} \Big|_{x_0, y} \right) \, d\eta, \quad 0 \leq x_0 \leq s_l, \end{aligned}$$

where s_y is the height of the plasma boundary above the source cup at x_0 , and where s_l is the maximum extent in x that the boundary extends into the

region, and

$$\begin{aligned} \int_0^y \phi_{yy}(x_0, y) \, d\eta &= \phi_y(x_0, y) \\ &= \phi_y(x_0, 0) - \int_0^y \left(\frac{\rho(x_0, y)}{\epsilon_0} + \frac{\partial^2 \phi}{\partial x^2} \Big|_{x_0, y} \right) \, d\eta, \quad s_l < x_0 \leq x_R, \end{aligned} \quad (5.9a)$$

where x_R is the location of the right hand boundary, S3. It is noted that the term, $\phi_y(x_0, 0)$ is present on the right hand side of (5.9a) because its value is not known there.

A minor drawback with using these integral expressions (that was absent in the one-dimensional case) is the presence of the second derivative terms, $\phi_{yy}(x, y_0)$ and $\phi_{xx}(x_0, y)$, on the right hand sides of (5.8) and (5.9), respectively. To successfully incorporate (5.7) and (5.9) into an iterative scheme, we must determine values for these terms. This was avoided in the one-dimensional formulation, but nevertheless does not present a problem in the strategy proposed here.

The system of equations, (5.1), written in the required two-dimensional Cartesian form can now grouped together as

$$v_x \frac{\partial v_x}{\partial x} + v_y \frac{\partial v_y}{\partial x} + \frac{\partial v_x}{\partial t} = \frac{q}{m} \int_a^x \left(\frac{\rho(x, y_0)}{\epsilon_0} + \frac{\partial^2 \phi}{\partial y^2} \Big|_{x, y_0} \right) \, d\xi, \quad (5.10a)$$

$$v_x \frac{\partial v_x}{\partial y} + v_y \frac{\partial v_y}{\partial y} + \frac{\partial v_y}{\partial t} = \frac{q}{m} \left[\int_b^y \left(\frac{\rho(x_0, y)}{\epsilon_0} + \frac{\partial^2 \phi}{\partial x^2} \Big|_{x_0, y} \right) \, d\eta - \frac{\partial \phi}{\partial y} \Big|_{x_0, b} \right], \quad (5.10b)$$

$$\frac{\partial(\rho v_x)}{\partial x} + \frac{\partial(\rho v_y)}{\partial y} = -\frac{\partial \rho}{\partial t}, \quad \text{and}, \quad (5.10c)$$

$$\frac{\partial^2 \phi}{\partial x^2} + \frac{\partial^2 \phi}{\partial y^2} = -\frac{\rho}{\epsilon_0}, \quad (5.10d)$$

where a and b refer to the integration starting locations in x and y , respectively. As described above, these are either s_x or 0, or s_y or 0 depending upon where the integral is to be determined from; the term $\phi_y(x_0, a)$ (in (5.10b)) is only present if $b = 0$. It is noted that the divergence terms in (5.1) have been expanded (in a Cartesian manner) to give (5.10c) and (5.10d).

5.1.1.1 Dimensionless Cartesian Form

The system, (5.10), is now written in a dimensionless form, and to do this, as in §4.3.1, we define the dimensionless variables

$$\tilde{\phi} = \frac{\phi}{\phi_m}, \quad (5.11a)$$

$$\tilde{\rho} = \frac{\rho}{\rho_m}, \quad (5.11b)$$

$$\tilde{v}_x = \frac{v_x}{v_m}, \quad (5.11c)$$

$$\tilde{v}_y = \frac{v_y}{v_m}, \quad (5.11d)$$

$$\tilde{x} = \frac{x}{L}, \quad (5.11e)$$

$$\tilde{y} = \frac{y}{L}, \quad (5.11f)$$

$$\text{and, } \tilde{t} = \frac{t}{t_m}. \quad (5.11g)$$

Here, L is the largest physical dimension (\tilde{x} and \tilde{y} are equally scaled) and ϕ_m , ρ_m , v_m and t_m are as defined in §4.3.1. In particular, we restate v_m and t_m as

$$v_m = \sqrt{\frac{2q\phi_m}{m}}, \quad (5.12)$$

$$t_m = \frac{L}{v_m}. \quad (5.13)$$

The Dimensionless Gauss' Law Since the integral expressions on the right hand side of (5.10a) and (5.10b) are determined from Gauss law, (5.10d), we write its dimensionless form first. The dimensionless variables particular to Gauss' Law, as written above, are those used in §4.3.1, and so we simply state its dimensionless form as

$$\frac{\partial^2 \tilde{\phi}}{\partial \tilde{x}^2} + \frac{\partial^2 \tilde{\phi}}{\partial \tilde{y}^2} = -\alpha_1 \tilde{\rho}, \quad (5.14)$$

where α_1 is given by (4.32) and similarly takes a typical value $O(10)$. The integrals, (5.7) and (5.9) can therefore be written in dimensionless form as

$$\begin{aligned} \left. \frac{\partial \tilde{\phi}}{\partial \tilde{x}} \right|_{\tilde{x}, \tilde{y}_0} &= - \int_{\tilde{a}}^{\tilde{x}} \left(\alpha_1 \tilde{\rho}(\tilde{x}, \tilde{y}_0) + \left. \frac{\partial^2 \tilde{\phi}}{\partial \tilde{y}^2} \right|_{\tilde{x}, \tilde{y}_0} \right) d\xi, \quad \text{and} \\ \left. \frac{\partial \tilde{\phi}}{\partial \tilde{y}} \right|_{\tilde{x}_0, \tilde{y}} &= - \int_{\tilde{b}}^{\tilde{y}} \left(\alpha_1 \tilde{\rho}(\tilde{x}_0, \tilde{y}) + \left. \frac{\partial^2 \tilde{\phi}}{\partial \tilde{x}^2} \right|_{\tilde{x}_0, \tilde{y}} \right) d\eta + \left. \frac{\partial \tilde{\phi}}{\partial \tilde{y}} \right|_{\tilde{x}_0, \tilde{b}}, \end{aligned}$$

where \tilde{a} and \tilde{b} are the dimensionless integration starting locations; these are analogous to a and b in (5.10a) and (5.10b).

The Dimensionless Lorentz Equations By substituting (5.15), along with the relevant dimensionless variables, into (5.10a) and (5.10b), we obtain

$$\tilde{v}_x \frac{\partial \tilde{v}_x}{\partial \tilde{x}} + \tilde{v}_y \frac{\partial \tilde{v}_y}{\partial \tilde{x}} + \frac{\partial \tilde{v}_x}{\partial \tilde{t}} = \alpha_2 \int_{\tilde{a}}^{\tilde{x}} \left(\alpha_1 \tilde{\rho}(\tilde{x}, \tilde{y}_0) + \left. \frac{\partial^2 \tilde{\phi}}{\partial \tilde{y}^2} \right|_{\tilde{x}, \tilde{y}_0} \right) d\xi, \quad (5.16a)$$

and

$$\tilde{v}_x \frac{\partial \tilde{v}_x}{\partial \tilde{y}} + \tilde{v}_y \frac{\partial \tilde{v}_y}{\partial \tilde{y}} + \frac{\partial \tilde{v}_y}{\partial \tilde{t}} = \alpha_2 \left[\int_{\tilde{b}}^{\tilde{y}} \left(\alpha_1 \tilde{\rho}(\tilde{x}_0, \tilde{y}) + \left. \frac{\partial^2 \tilde{\phi}}{\partial \tilde{x}^2} \right|_{\tilde{x}_0, \tilde{y}} \right) d\eta - \left. \frac{\partial \tilde{\phi}}{\partial \tilde{y}} \right|_{\tilde{x}_0, \tilde{b}} \right], \quad (5.16b)$$

where α_2 is given by

$$\alpha_2 = \frac{L}{2\phi_m}$$

from (5.12) and (5.13). The parameter α_2 has a typical value of $\sim 10^{-8}$ and will tend to remove the effects of the integrals on the right hand sides of (5.16a) and (5.16b), unless the second derivative terms are significant. This will tend to be true just away from the plasma boundary where the curvature in ϕ is at its greatest.

The Dimensionless Continuity Equation Substituting the relevant dimensionless variables into (5.10c), we obtain

$$\frac{\rho_m v_m}{L} \left(\frac{\partial(\tilde{\rho}\tilde{v}_x)}{\partial\tilde{x}} + \frac{\partial(\tilde{\rho}\tilde{v}_y)}{\partial\tilde{y}} \right) = -\frac{\rho_m}{t_m} \frac{\partial\tilde{\rho}}{\partial\tilde{t}}, \quad (5.17)$$

and by noting that t_m is given by (5.13), (5.17) can be written

$$\frac{\partial(\tilde{\rho}\tilde{v}_x)}{\partial\tilde{x}} + \frac{\partial(\tilde{\rho}\tilde{v}_y)}{\partial\tilde{y}} = -\frac{\partial\tilde{\rho}}{\partial\tilde{t}}. \quad (5.18)$$

Dimensionless Boundary Conditions To be consistent with the dimensionless system, (5.14), (5.16) and (5.18), the boundary conditions, (5.2), must also be restated in dimensionless form and these are

$$\begin{aligned} \tilde{\phi}(\tilde{\mathbf{x}}, \tilde{t}) &= \frac{\phi_S}{\phi_m} \\ &= \tilde{\phi}_S, & \tilde{t} \geq 0, \tilde{\mathbf{x}} \in \tilde{S}_1 \cup \tilde{S}_2 \end{aligned} \quad (5.19a)$$

$$\begin{aligned} \phi(\tilde{\mathbf{x}}, \tilde{t}) &= \frac{\phi_T}{\phi_m} \\ &= \tilde{\phi}_T, & \tilde{t} \geq 0, \tilde{\mathbf{x}} \in \tilde{S}_4 \end{aligned} \quad (5.19b)$$

$$\tilde{\nabla}\tilde{\phi}(\tilde{\mathbf{x}}, \tilde{t}) \cdot \tilde{\mathbf{n}}_1 = 0, \quad \tilde{t} > 0, \tilde{\mathbf{x}} \in \tilde{S}_1 \quad (5.19c)$$

$$\left. \frac{\partial\tilde{\phi}}{\partial\tilde{x}} \right|_{\tilde{\mathbf{x}}, \tilde{t}} = 0, \quad \tilde{t} > 0, \tilde{\mathbf{x}} \in \tilde{S}_5 \quad (5.19d)$$

$$\tilde{\rho}(\tilde{\mathbf{x}}) = \frac{\rho_s(\tilde{\mathbf{x}})}{\rho_m}, \quad \tilde{t} \geq 0, \tilde{\mathbf{x}} \in \tilde{S}_1 \quad (5.19e)$$

$$\tilde{\rho} = 0, \quad \tilde{t} \geq 0, \tilde{\mathbf{x}} \in \tilde{S}_2, \quad (5.19f)$$

$$\tilde{\rho} = 0, \quad \tilde{t} = 0, \tilde{\mathbf{x}} \in \tilde{R}, \tilde{\mathbf{x}} \notin \tilde{S}_1 \cup \tilde{S}_2, \quad (5.19g)$$

$$\left. \frac{\partial \tilde{\rho}}{\partial \tilde{x}} \right|_{\tilde{\mathbf{x}}, \tilde{t}} = 0, \quad \tilde{t} > 0, \tilde{\mathbf{x}} \in \tilde{S}_5 \quad (5.19h)$$

$$\begin{aligned} \tilde{\mathbf{v}} &= \frac{v_i}{v_m} \tilde{\mathbf{n}}_1 \\ &= \tilde{v}_i(\tilde{\mathbf{x}}) \tilde{\mathbf{n}}_1, \quad \tilde{t} \geq 0, \tilde{\mathbf{x}} \in \tilde{S}_1 \end{aligned} \quad (5.19i)$$

$$\tilde{\mathbf{v}} = \mathbf{0}, \quad \tilde{t} = 0, \tilde{\mathbf{x}} \in \tilde{R}, \tilde{\mathbf{x}} \notin \tilde{S}_1 \quad (5.19j)$$

$$\tilde{\mathbf{v}} \cdot \tilde{\mathbf{n}}_5 = 0, \quad \tilde{t} > 0, \tilde{\mathbf{x}} \in \tilde{S}_5. \quad (5.19k)$$

Here, \tilde{R} is the dimensionless region enclosed by the boundaries \tilde{S}_1 to \tilde{S}_5 ; the vectors $\tilde{\mathbf{n}}_1$ and $\tilde{\mathbf{n}}_5$ are the unit normals to \tilde{S}_1 and \tilde{S}_5 , respectively. The dimensionless gradient operator, $\tilde{\nabla}$, in (5.19c) has been written in Cartesian form in (5.19d) and (5.19h), where it is clear that potential or charge density do not change across the line of symmetry, at $\tilde{x} = 0$. Typically, $\tilde{\phi}_S = 1$ and $\tilde{\phi}_T = 0$, since $\phi_T = 0$ and $\phi_m = \phi_S$.

5.2 Strategy for the Determination of the Two-dimensional Steady-State Solution

In a vacuum tube, in which the emission boundary is fixed (such as a vacuum tube diode), high emission current densities accompanied by low acceleration voltages will give rise to a charge build-up immediately above the emission surface. This occurs because the high charge flux from the emission surface is not matched by the acceleration of charge away from the surface, as a consequence of the relatively low acceleration potential. The effect of such

a build-up of *space charge* is that a steady condition ensues in which charge leaving the emission surface behind the space charge build-up is repelled by it ([3], p191). This condition is known as space charge *limitation* and can be modelled in one dimension by the Child-Langmuir relationship¹ ([3], p171).

If the space charge limitation is severe, the electric field at the build-up of charge will be neutralised, effectively indicating the location of the new emission boundary ([3], p191). The numerical method presented in this chapter exploits this property to determine the location of the plasma boundary. It does this by calculating a fixed boundary solution, only terminating this calculation when either a maximum in potential exists within the solution region², or when the numerical method begins to become unstable, as a consequence of the space charge limitation. Instability is identified by examining the mean of the relative root mean square change in solution, of all solution variables (called MRMS in ensuing paragraphs), at each time-step. Generally convergence is observed in that there is a rapid decrease in MRMS with time-step, until space charge limitation becomes apparent when MRMS generally begins to increase. This is a phenomenon also observed when using other, off-the-shelf, fixed boundary ion beam codes (for example, OPERA2d), that calculate the fixed boundary solution in a slightly different way by tracking particles individually in a Lagrangian manner. When space charge limitation occurs with these codes, fixed boundary solution convergence is usually not

¹This relationship is effectively the fixed boundary equivalent solution to the planar free-boundary solution developed in Chapter 3.

²At this point the charge entering the region is not being accelerated away fast enough by the accelerating potential, resulting in space charge build-up and current limitation, and a consequent maximum in electrostatic potential ([3]).

achieved.

When either a potential maximum within the solution region or an increase in MRMS (or both) has been identified, the solution is examined and the new boundary location determined to be the location of the zero electric field level curve (satisfying (5.19c)) near the existing fixed boundary. Further iterations can then be performed, with the boundary location generated previously forming the new emission surface. This process can be repeated until either the boundary does not move any further, or until there is no further build-up of space charge immediately above the emission boundary; both conditions should occur at the same time. At this point, the free-boundary location has been determined.

This solution strategy has been implemented in Matlab (as with all previous models), and we now describe the solution algorithm, as implemented, in more detail.

5.2.1 Solution Algorithm for the Two-dimensional Steady-state Calculation

The method proposed in §5.2, as implemented, can be broken down into the following procedure. The algorithm steps are as follows.

Step 1

- Set up the fixed solution region with n_x equally spaced nodes in the \tilde{x} direction, and n_y equally spaced node in the \tilde{y} directions; the spacing in each direction is labelled $\Delta\tilde{x}$ and $\Delta\tilde{y}$, respectively, where $\Delta\tilde{x} = \tilde{x}_R/(n_x - 1)$ and $\Delta\tilde{y} = \tilde{y}_T/(n_y - 1)$. As in the one-dimensional time-

dependent model, the subscripts i and j are used to represent i^{th} node in \tilde{x} and the j^{th} node in \tilde{y} . Ensure the right hand edge (\tilde{x}_E) of the fixed emission region coincides with a nodal point.

- Set the time-step size $\Delta\tilde{t}$. As in the one-dimensional time-dependent model, the superscript k is used to represent a variable at the k^{th} time-step.
- The fixed emission boundary sits adjacent to the line of symmetry (S_5 in Figure 5.1), along the \tilde{x} axis; it is labelled $\tilde{s}_f = \tilde{s}_f(\tilde{x}, 0)$ here, with its right hand edge being located at $(\tilde{x}_s, 0)$.

Step 2

- Initialise the solution variable matrices for the variables $\tilde{\phi}$, $\tilde{\rho}$, \tilde{v}_x , and \tilde{v}_y . The solution is stored at each nodal point in matrices of dimension (n_y, n_x) , accounting for each nodal point within the region.
- Add any constant (in time) boundary conditions to these variables, prior to beginning calculations, as follows.
 - The charge density (at each time-step) is ramped, in space, along the emission boundary to avoid a discontinuity at the right hand edge; it takes the form

$$\tilde{\rho}(\tilde{x}) = \left\{ 1 + \exp \left(4 \frac{(L\tilde{x} - c_x)}{w_x} \right) \right\}^{-1},$$

where here, c_x/L is the midpoint of the ramp transition and w_x/L is a measure of the ramp transition width (previously described in §4.3.2.3). This gives rise to a curve similar to that shown in Figure 5.2.

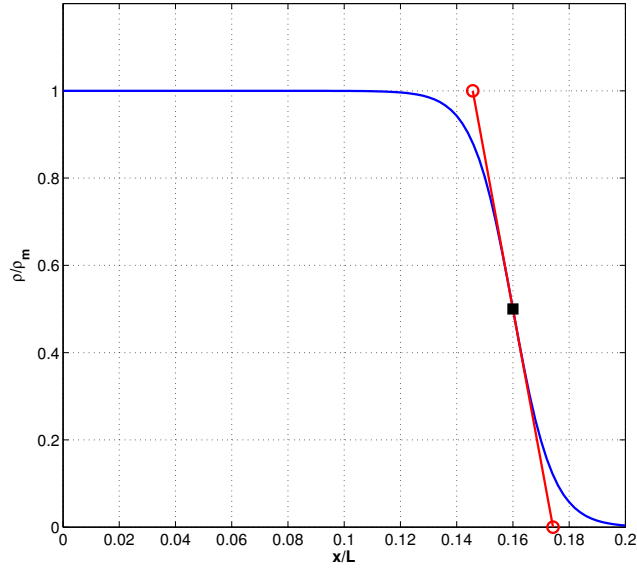


Figure 5.2: Constant charge density profile along the emission boundary. The region line of symmetry is located at $x/L = 0$, the midpoint of the ramp transition is at c_x/L (in this case at $x/L = 0.16$, shown by the black square marker) and a measure of the transition width (the distance between the two red, circular markers) is given by w_x/L ($w_x/L = 0.0286$ in this case).

- The velocity magnitude (at each time-step) along the boundary, $\tilde{v}_i(\tilde{x})$, has a similar ramp applied. In the fixed boundary case, since ions are emitted normally away from the emission boundary, only the component \tilde{v}_y is affected.
- The conditions, (5.19a) and (5.19b), are applied to the potential solution matrix.

Step 3

- As a starting point, calculate the equivalent one-dimensional steady-

state potential solution for the boundary conditions applied, using the analytic expression, (3.28); map this solution onto the line of symmetry in both the potential and charge density solution variables (the charge density being calculated from (4.1c).

- Using the one-dimensional solution along this boundary, in conjunction with the other boundary conditions already applied, perform relaxation on the potential and charge density solution variables. The relaxation process applied is effectively the same as seeking the solution of the Laplace equations,

$$\begin{aligned}\frac{\partial^2 \tilde{\phi}}{\partial \tilde{x}^2} + \frac{\partial^2 \tilde{\phi}}{\partial \tilde{y}^2} &= 0 \quad \text{and} \\ \frac{\partial^2 \tilde{\rho}}{\partial \tilde{x}^2} + \frac{\partial^2 \tilde{\rho}}{\partial \tilde{y}^2} &= 0,\end{aligned}$$

for the potential and charge density, respectively. It is done using a five point nodal averaging procedure, where for a general point, $\tilde{\phi}_{i,j}$, say, within the region, the $(k + 1)^{\text{th}}$ average would be given by

$$\tilde{\phi}_{i,j}^{k+1} = (\tilde{\phi}_{i-1,j}^k + \tilde{\phi}_{i+1,j}^k + \tilde{\phi}_{i,j+1}^k + \tilde{\phi}_{i,j-1}^k)/4.$$

Since we are only seeking a steady-state solution, the initial solutions in $\tilde{\phi}$ and $\tilde{\rho}$, generated by the relaxation procedure, are a suitable starting location for the steady state calculation;

Begin iterations on the fixed region, proceeding in the following order.

Step 4

- Calculate $\tilde{\phi}_{\tilde{y}\tilde{y}}$ from the most recent potential solution, using the second order central difference, (4.55). Calculate the updated \tilde{v}_x component,

$$\begin{aligned} \tilde{v}_x|_{i,j}^{k+1} = \tilde{v}_x|_{i,j}^k + \Delta\tilde{t} \left\{ \alpha_2 \int_0^{\tilde{x}_i} \left(\alpha_1 \tilde{\rho}_{i,j}^k + \tilde{\phi}_{\tilde{y}\tilde{y}}|_{i,j}^k \right) d\xi \right. \\ \left. - \left[\tilde{v}_x \frac{\partial \tilde{v}_x}{\partial \tilde{x}} \right]_{i,j}^k - \left[\tilde{v}_y \frac{\partial \tilde{v}_y}{\partial \tilde{x}} \right]_{i,j}^k \right\}, \end{aligned} \quad (5.21)$$

from (5.16a), using upwinded differences (as in the one-dimensional case) for the first order derivatives. The integral in (5.21) is calculated using the trapezium rule.

Step 5

- Calculate $\tilde{\phi}_{\tilde{x}\tilde{x}}$ from the most recent potential solution, using the second order central difference, (4.55). Calculate the updated \tilde{v}_y component,

$$\begin{aligned} \tilde{v}_y|_{i,j}^{k+1} = \tilde{v}_y|_{i,j}^k + \Delta\tilde{t} \left\{ \alpha_2 \int_0^{\tilde{y}_i} \left(\alpha_1 \tilde{\rho}_{i,j}^k + \tilde{\phi}_{\tilde{x}\tilde{x}}|_{i,j}^k \right) d\xi \right. \\ \left. - \left[\tilde{v}_x \frac{\partial \tilde{v}_x}{\partial \tilde{y}} \right]_{i,j}^{k+1} - \left[\tilde{v}_y \frac{\partial \tilde{v}_y}{\partial \tilde{y}} \right]_{i,j}^k \right\}, \end{aligned} \quad (5.22)$$

from (5.16b), using upwinded differences (as in the one-dimensional case) for the first order derivatives, and using the \tilde{v}_x component most recently calculated. The integral in (5.22) is calculated using the trapezium rule.

Step 6

- Calculate the updated charge density,

$$\tilde{\rho}_{i,j}^{k+1} = \tilde{\rho}_{i,j}^k - \Delta\tilde{t} \left\{ \frac{\partial}{\partial \tilde{x}} \left(\tilde{\rho}_{i,j}^k \tilde{v}_x|_{i,j}^{k+1} \right) + \frac{\partial}{\partial \tilde{y}} \left(\tilde{\rho}_{i,j}^k \tilde{v}_y|_{i,j}^{k+1} \right) \right\} \quad (5.23)$$

from (5.18), using the most recently calculated values for \tilde{v}_x and \tilde{v}_y . Derivatives in (5.23) are calculated using first order upwinded differences, as in the one-dimensional model.

Step 7

- Solve Gauss' Law, (5.14), using the most recently calculated values for $\tilde{\rho}$. This is done using a standard, second order five point difference stencil (as described in [26], Chp 6). Examine the resulting solution and if a potential maximum exists within the solution region (instead of at the plasma boundary), terminate the fixed-boundary calculation at the current time-step. The Matlab "find" command is a suitable tool for performing the examination.

Step 8

- Generate the MRMS at the current time-step. This is done by calculating the RMS change in solution (between the current and previous time-step) as a fraction of the RMS solution at the current time-step, for each of the four solution variables, \tilde{v}_x , \tilde{v}_y , $\tilde{\rho}$, and $\tilde{\phi}$. For $\tilde{\rho}$, for example, the relative RMS change in solution is calculated as

$$RMS(\tilde{\rho}) = \frac{\sqrt{\frac{1}{n_x n_y} \sum_i \sum_j (\tilde{\rho}_{i,j}^{k+1} - \tilde{\rho}_{i,j}^k)^2}}{\sqrt{\frac{1}{n_x n_y} \sum_i \sum_j (\tilde{\rho}_{i,j}^{k+1})^2}},$$

where the product $(n_x n_y)$ is the total number of nodes. Once this is known for all solution variables, the mean of all four (previously called the MRMS) is calculated.

Step 9

- Examine the rate of change of MRMS and if this has a positive mean over, say, the previous ten time-steps, terminate the fixed boundary calculation at the current time-step. If this condition is not true, continue the iterations by returning to Step 4, above.

Step 10

- Once the initial fixed boundary calculation has been concluded, examine the potential solution and calculate the electric field magnitude from

$$|\tilde{\mathbf{E}}| = \sqrt{\left(\frac{\partial\tilde{\phi}}{\partial x}\right)^2 + \left(\frac{\partial\tilde{\phi}}{\partial y}\right)^2}.$$

- Determine the level curve corresponding to an electric field magnitude of zero. This is done using the Matlab “contourc” command, with a requirement for a single contour at height zero.
- Identify those fixed nodes, within the solution domain, that are closest to the zero electric field magnitude level curve. These nodes form the location of the plasma boundary for the next stage of calculation. An example of the result of this process is shown in Figure 5.3. The most convenient tool for locating the nearest nodes is the Matlab “find” command.

Step 11

- Calculate the gradient of the new boundary at each node along it; from the gradient, calculate angle of the inward (into the region) directed

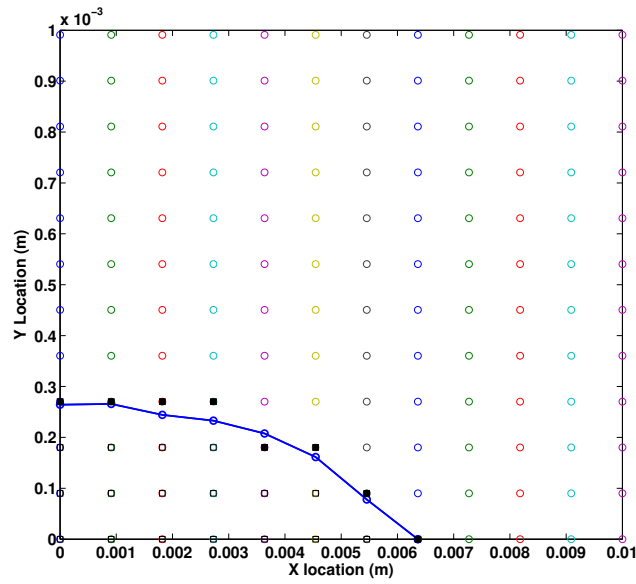


Figure 5.3: The location of the level curve corresponding to zero electric field magnitude, and nearest grid nodes. The blue line is the level curve, whilst the black, square markers are the nodes identified as being nearest this curve. Information is displayed in dimensional space, with the right hand edge of the flat emission boundary (x_E) being located at $x = 0.01\text{m}$. After the initial fixed boundary solution, nodes below the blue line are considered to be outside of the region.

normal at those nodes. If the angle of the inward normal at the p^{th} node on the new plasma boundary is labelled $\theta_s(\tilde{\mathbf{x}}_p)$, then the velocity boundary condition, (5.19i), as applied to the \tilde{v}_x and \tilde{v}_y velocity component solution variables along this boundary, is given by the pair of expressions

$$\tilde{v}_x(\tilde{\mathbf{x}}_p) = \tilde{v}_i \cos(\theta_s(\tilde{\mathbf{x}}_p)), \text{ and}$$

$$\tilde{v}_y(\tilde{\mathbf{x}}_p) = \tilde{v}_i \sin(\theta_s(\tilde{\mathbf{x}}_p)).$$

- Apply the charge density condition, (5.19e), along the new boundary.

Step 12

- Repeat the iterative process described above, but when necessary, integrate in the \tilde{x} and \tilde{y} directions from the expanding boundary (not including the nodes behind it); remove the rows and columns, corresponding to these nodes, from the matrix generated within the Gauss Law Poisson solver, moving those values on the new boundary to the source vector on the right hand side of the system of equations generated by the Poisson solver. Calculate MRMS at each time-step of the iterative procedure. Halt the procedure if a maximum in potential exists inside the region, or if MRMS begins to increase; re-examine the solution.

5.2.2 Test Case

To test the method, a set of conditions that will cause plasma to expand into the solution region, but not cause the emission region to become too distended, are applied. Generally, the application of a relatively high current density at the emission boundary for a normal operating voltage will cause this to happen. Indeed, usual operating conditions, applied to a neutron tube, should cause some bulging of the boundary into the solution region, and so we choose to apply a source potential of 120kV, a source current density of 18800Am^{-2} , and an initial particle energy of 50eV. The applied conditions detailed here are listed in Table 5.1, along with other numerical parameters.

Parameter	Value	Description
n_x	56	Number of nodes in x direction.
Δx	1/1100 m	Nodal spacing in x direction.
n_y	112	Number of nodes in y direction.
Δy	1/11100 m	Nodal spacing in y direction.
Δt	1×10^{-11} s	Time step size.
L	0.05 m	Region width (length scaling parameter).
y_T	0.01 m	Nominal source-target spacing.
x_E	0.01 m	Width of emission region.
ϕ_S	100 kV	Source potential.
ϕ_T	0 kV	Target potential.
J_0	18800 Am^{-2}	Source current density.
Ie	50 eV	Initial particle energy.

Table 5.1: Numerical parameters for the two-dimensional steady-state test problem.

5.2.2.1 Results

Selected results are displayed for three stages of calculation, in which the boundary is seen to advance from the initial fixed location.

Fixed boundary solution - stage 1 After exiting the initial calculation stage, the calculated boundary location was found and this is shown in Figure 5.4. Here, because the new calculated boundary location is so close to the initial, fixed emission region, the nodes within the region that are closest

to the new boundary, are still located along the initial fixed boundary. The calculated new boundary location is shown as the blue line, and the closest nodes as the black, square markers. Figure 5.5 shows the modified boundary

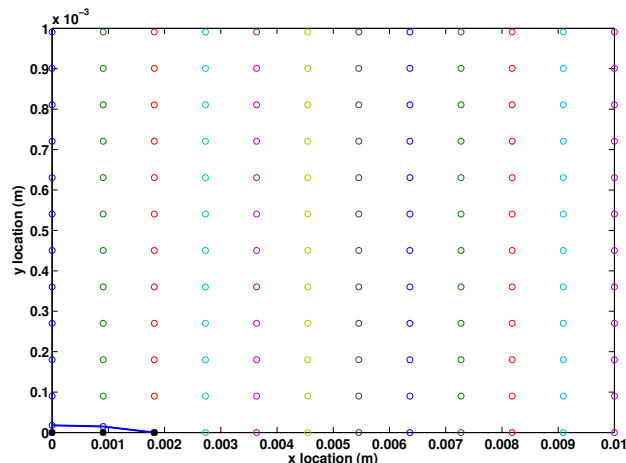


Figure 5.4: After the initial calculation stage, the new boundary location is calculated to be the blue line. The nodes within the fixed grid that are closest to this boundary are shown as the black, square markers. A small part of the underlying computational grid is also shown.

conditions applied to the v_x and v_y variables, respectively, as a result of the shape of the new boundary shown in Figure 5.4. Whilst, on the computational grid, the boundary isn't changed for the next stage of the calculation (since the nearest nodes are those on the existing fixed boundary), the v_x and v_y components, along the boundary, are updated. It can be seen that the y directed velocity component along the boundary is some one hundred times the magnitude of the x directed component. This (the v_x boundary condition) will have very little effect on the next stage of the calculation.

The potential solution at this stage is shown in Figures 5.6 and 5.7, where

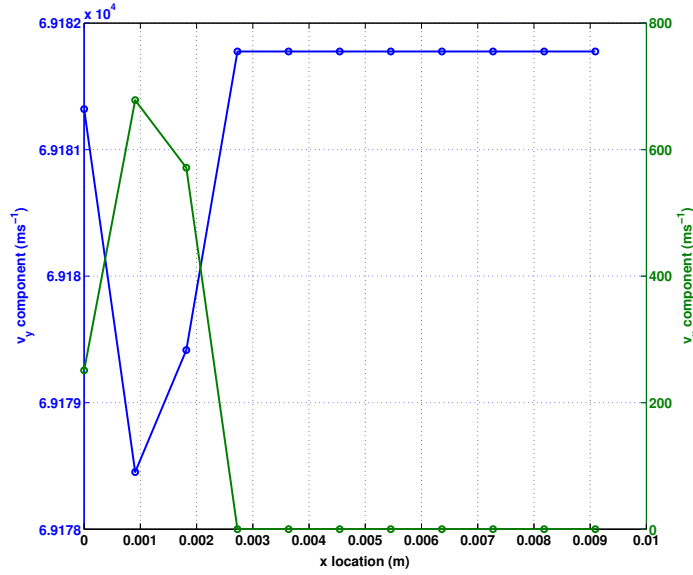


Figure 5.5: The modified boundary conditions for v_x and v_y as a consequence of the new boundary shown in Figure 5.4.

in Figure 5.6, the build-up of charge ahead of the fixed emission boundary is causing, what is now, typical curvature in the potential solution there. Figure 5.7 shows potential level curves (40 curves spaced 3kV apart), where a "bulge" immediately above the emission region is apparent.

Figures 5.8 and 5.9 show the charge density solution at this stage. In Figure 5.8, the ramped, constant charge density across the emission region can be seen; it changes from a maximum of $j_0/v_i = 0.2717 \text{ Cm}^{-3}$ to zero rapidly at 4/5 distance along (traversing from right to left in the upper right hand part of the figure). Figure 5.9 shows the corresponding charge density level curves (40 curves, equally spaced from 0 to 0.2717 Cm^{-3}).

Figures 5.10 and 5.11 show the x component of velocity, v_x . The sharp ridge in Figure 5.10 indicates that particles, in this location, are being accel-

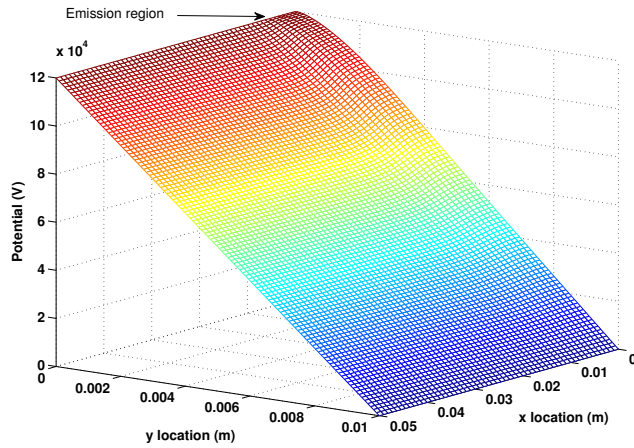


Figure 5.6: The initial potential solution surface.

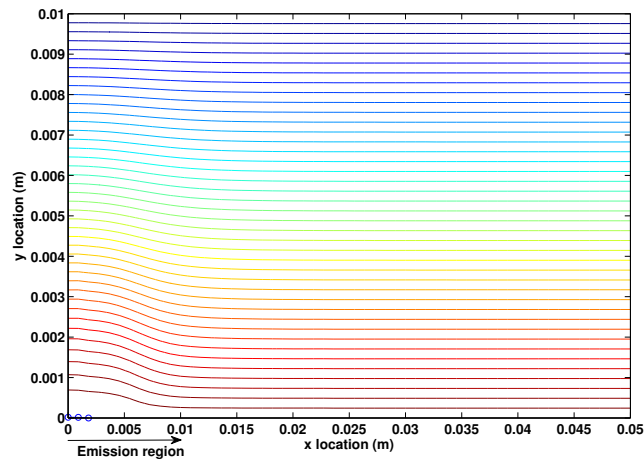


Figure 5.7: Initial potential solution level curves. The calculated, new plasma boundary is just visible and is shown as the blue line to the bottom left of the figure.

erated outwards as they travel towards the target. Physically, this is caused by mutual charge repulsion within the ion beam. A slight, overall beam

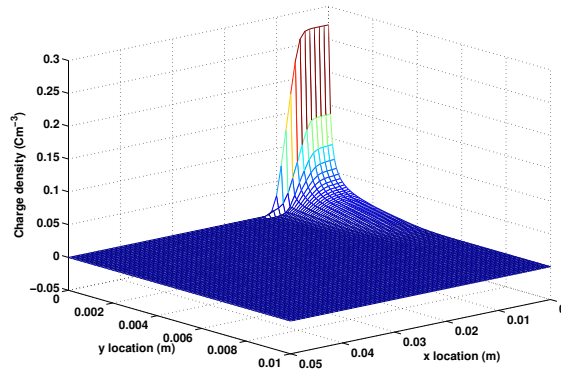


Figure 5.8: The initial charge density solution surface. The ramp along the emission surface (to the upper right of the figure) is visible, where the charge density at the emission surface decays rapidly from its maximum (j_0/v_i) to zero when at $4/5$ distance along.

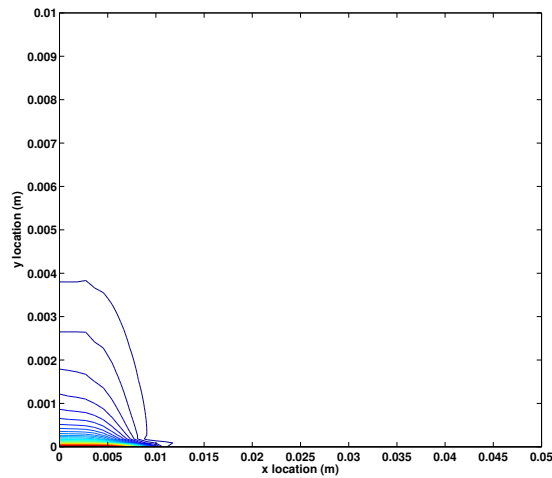


Figure 5.9: Initial charge density level curves. The highest charge density is shown in red, immediately above the emission region.

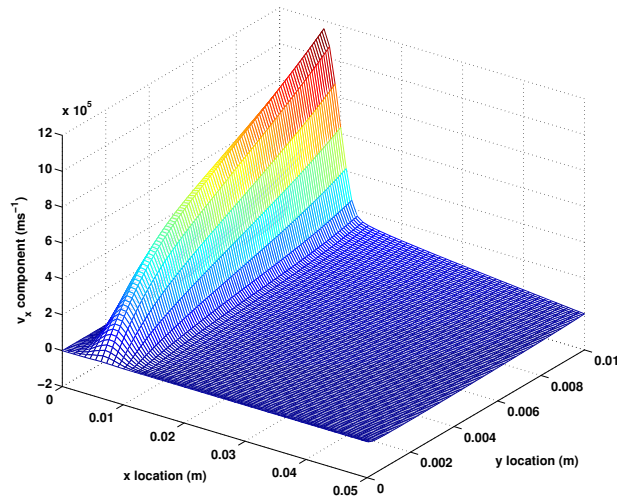


Figure 5.10: x component of velocity. The sharp ridge is evidence of mutual charge repulsion within the ion beam and shows evidence of lateral acceleration caused by this.

splaying is visible in Figure 5.11; at this accelerating voltage, experimental experience indicates that only a small degree of beam splaying would occur.

For completeness, Figure 5.12 shows the y component of velocity. The curved shape of v_y as a function of source-target distance was seen in the one-dimensional model; for comparison, the expected one-dimensional velocity of a deuteron under acceleration from the steady-state potential solution is shown in Figure 5.13, along with the two-dimensional v_y component, along the y -axis (or line of symmetry). In both cases, the same ultimate speed at the target is reached (indicating some consistency in calculation), but the two-dimensional curve is distinctly more curved.

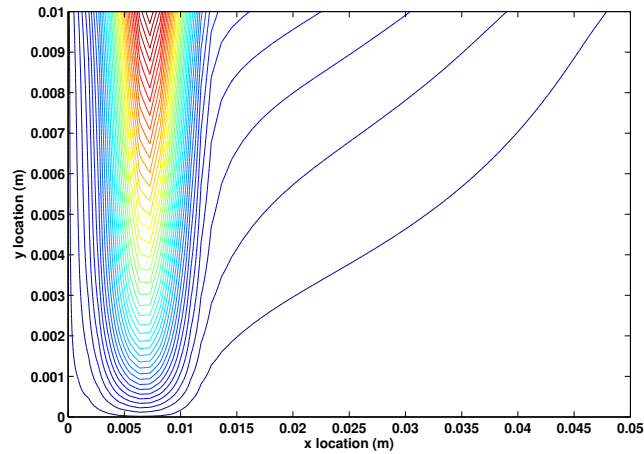


Figure 5.11: x component of velocity level curves. A small degree of beam splaying is evident.

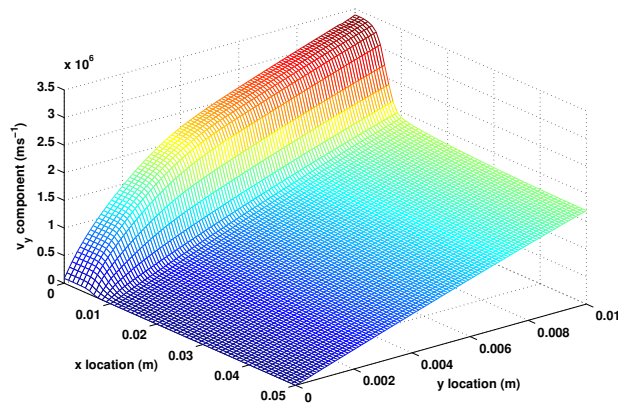


Figure 5.12: y component of velocity.

Figure 5.14 shows the MRMS (described above) for the 400 iterations of this stage of calculation. There is a clear reduction in MRMS as the calculation proceeds, indicating that until the stage was terminated, the solution was converging.

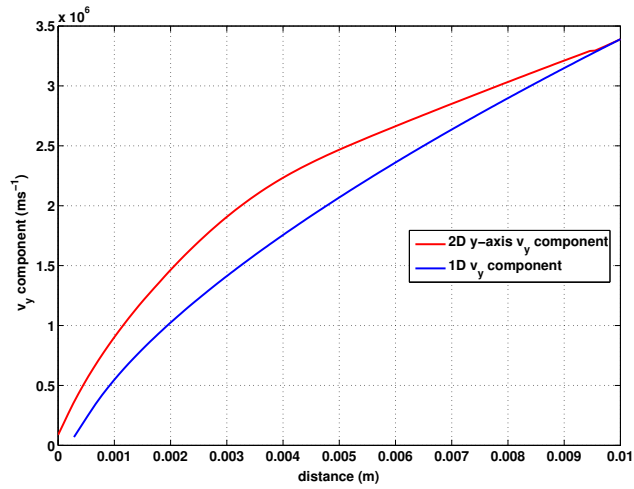


Figure 5.13: Comparison between two-dimensional v_y component (along the y -axis line of symmetry) and the one-dimensional calculated velocity of a deuteron under the acceleration caused by the calculated steady-state accelerating voltage. It is noted that the one-dimensional curve does not reach the source boundary, as a consequence of the steady-state reduced region size.

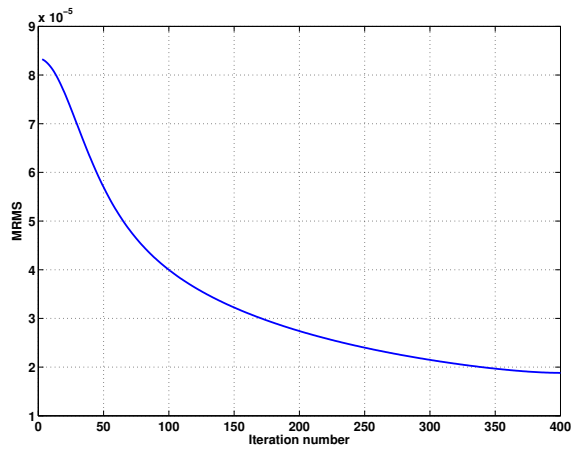


Figure 5.14: MRMS with iteration number - stage 1.

Modified boundary solution - stage 2 The next fixed boundary calculation stage proceeded for a further 375 iterations before termination. Whilst the boundary calculated in stage 1 did not result in any change in the region size, velocity components were modified as mentioned above. This, second stage, resulted in more significant change in boundary location as shown in Figure 5.15. Here, the new boundary is shown as the blue line, with the underlying region nodes that are nearest, shown as the black, square markers. For comparison, the red line indicates the location of the boundary from stage 1, above. Figure 5.16 shows the modified boundary conditions applied

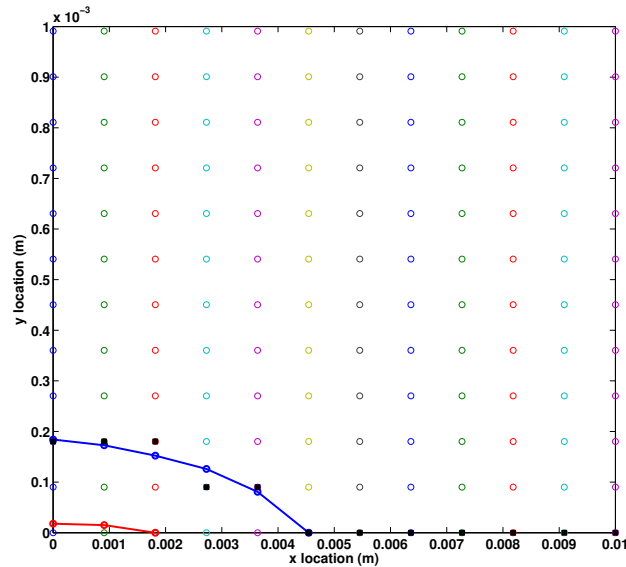


Figure 5.15: Calculated boundary location for stage 2. The blue line shows the new boundary location and the black, square markers are the nodes nearest the boundary on the underlying grid. The red line is the boundary location calculated from the previous stage.

to the v_x and v_y variables, respectively, as a result of the shape of the new

boundary shown in Figure 5.15. It can be seen that the y directed velocity component along the boundary is some one hundred times the magnitude of the x directed component. The peak x directed velocity component at the boundary is now some twenty times smaller than the y directed velocity component.

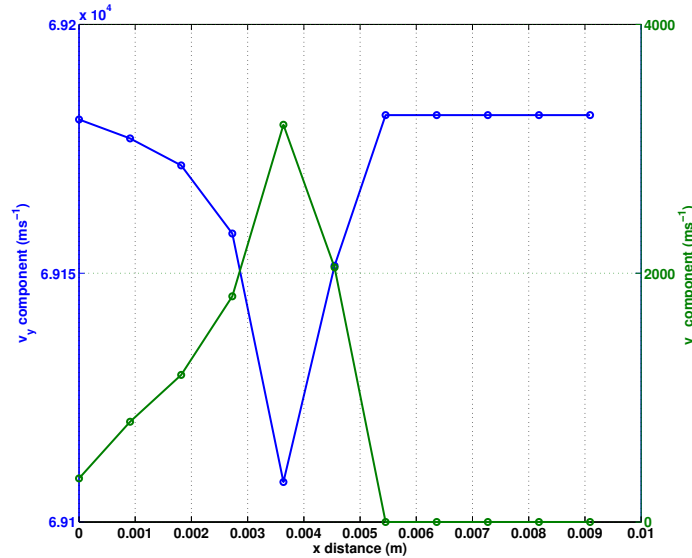


Figure 5.16: The modified boundary conditions for v_x and v_y as a consequence of the new boundary shown in Figure 5.15.

Figures 5.17 and 5.18 show the potential solution at stage 2. Within Figure 5.17, nodes behind the new boundary have been removed to highlight the new emission boundary (the missing nodes can just be seen at the upper right of the figure) and will not contribute to the following calculation stage. The calculated emission boundary is shown in Figure 5.18 and whilst the potential solution does not look significantly different to that shown in stage 1 (Figures 5.6 and 5.7), examination of the level curves (40 curves spaced 1

3 kV apart in both cases) near the emission boundary in both cases show that there is some boundary advancement (i.e. the two curves nearest the emission region are advancing from stage 1 to stage 2). This indicates advancement of the plasma boundary.

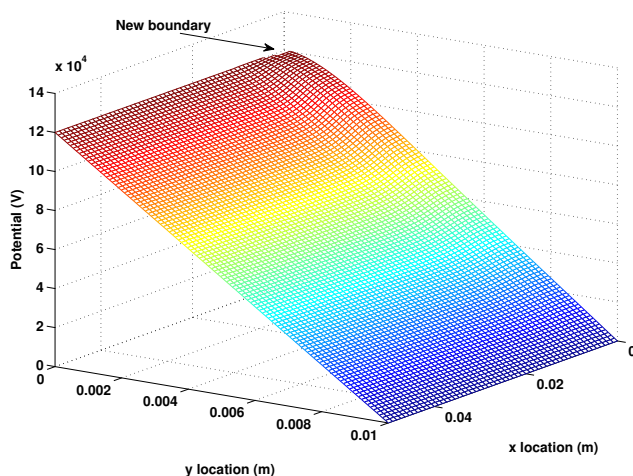


Figure 5.17: Stage 2 potential solution surface. Nodes behind the new emission boundary have been removed to highlight their location (just visible to the upper right) and do not contribute to the next stage.

As a way of determining the extent of the beam splaying at this stage, the charge density solution was scaled (by the reciprocal of the particle charge) in order to determine the particle number density across the region. Figure 5.19 shows the particle number density across the target (a logarithmic scale is used on the ordinate axis), where it can be seen that after ~ 0.015 m, there is less than one particle per unit metre within the region. Therefore we conclude that the very outer edge of the ion beam strikes the target at the location $x = 0.015$ m. This indicates some degree of beam splaying, considering that the majority of charge is emitted from a region between the

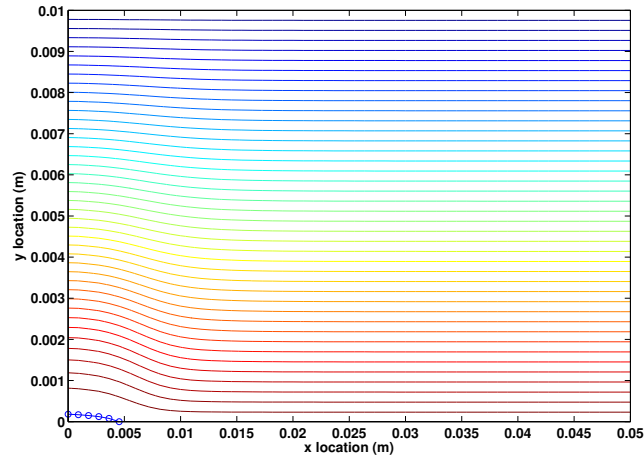


Figure 5.18: Stage 2 potential solution level curves. There is advancement of the curves nearest the boundary from stage 1. The new, calculated plasma boundary is shown as the blue line to the bottom left of the figure.

y axis and $x = 0.008$ m.

Figure 5.20 shows MRMS for the combined stages one and two (775 iterations). The discontinuity at iteration number 400 is likely to be caused by the minor modifications introduced as a consequence of the boundary shape in stage 1 (i.e. the velocity component modifications). Again, there is a clear reduction in MRMS as the calculation proceeds, indicating that until the stage was terminated, the solution was converging.

Modified boundary solution - stage 3 The final stage of calculation proceeded for a further 350 iterations, where it was terminated. Figure 5.21 shows the boundary location at the end of this stage. As before, the new boundary is shown as the blue line, with the underlying region nodes that are nearest, shown as the black, square markers. For comparison, the green

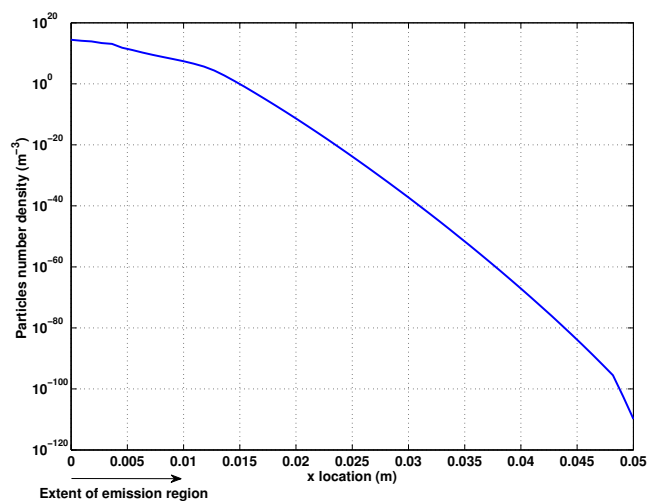


Figure 5.19: The particle number density across the target. The very outer edge of the beam is considered to be when the number density falls below one particle per cubic metre (in this case at 0.015 m).

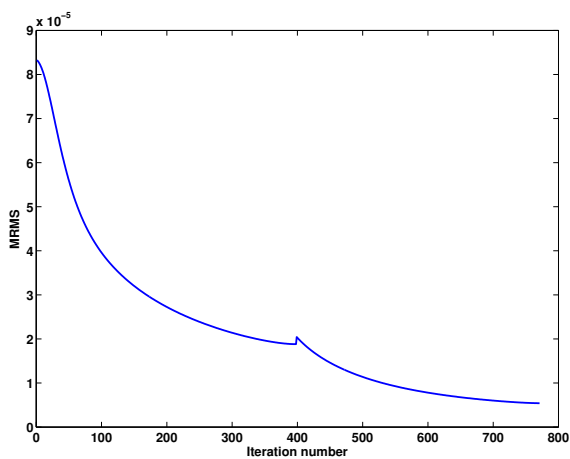


Figure 5.20: MRMS with iteration number - stages 1 and 2.

and red lines indicate the location of the boundary from stages 1 and 2, respectively. For comparison, the location of the boundary calculated from the

one-dimensional planar, analytic solution ((3.23)), for the given set of conditions is shown. It is noted that part of the boundary ($x > 0.0063$ m) does

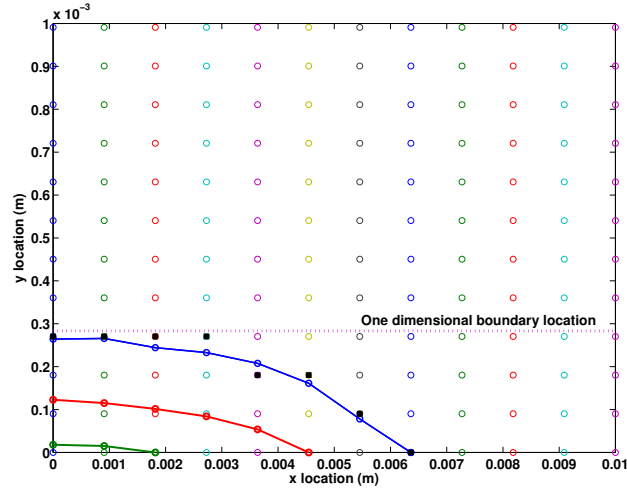


Figure 5.21: Calculated boundary location for stage 3. As before, the blue line shows the new boundary location and the black, square markers are the nodes nearest the boundary on the underlying grid. The red and green lines are the boundary locations from steps 2 and 1, respectively.

not penetrate into the body of the region. This is due to the applied source charge density ramp decaying rapidly beyond this point. In this region, the charge density is relatively low, and combined with the accelerating voltage, will give rise to a recessed boundary. Figures 5.22 and 5.23 show the potential solution at stage 3. As before, within Figure 5.17, nodes behind the new boundary have been removed to highlight the new emission boundary. The calculated emission boundary is shown in Figure 5.23, where the blue line to the bottom left hand corner indicates the plasma boundary location. The gap between the boundary and the first level curve is an indication that

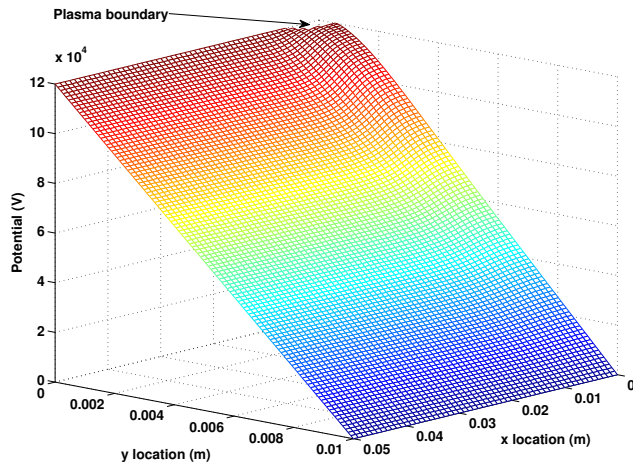


Figure 5.22: Stage 3 potential solution surface. Nodes behind the new emission boundary have been removed to highlight their location.

the potential solution is not changing rapidly there ((5.2c)). Indeed Figure 5.24 shows the calculated electric field magnitude across the region, where it can be clearly seen that the field magnitude is zero at the boundary surface (shown as the blue line).

Figure 5.25 shows the particle number density across the target. Here, the very outer edge of the beam, based on the previous definition, is found to be at about 0.014 m, indicating that the beam has focussed inwards slightly from the previous stage, this is slightly counter-intuitive, but the previous stage was an interim stage of the calculation.

Finally, figure 5.26 shows MRMS for the combined stages one, two and three (1125 iterations). The quite large discontinuity at iteration number 775 is most likely to have been caused by the boundary modifications introduced as a consequence of the boundary shape in stage 2 (i.e. the velocity

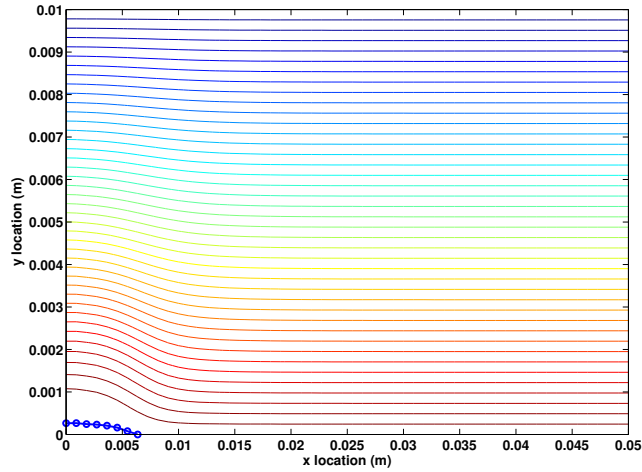


Figure 5.23: Stage 2 potential solution level curves. The calculated plasma boundary is shown as the blue line to the bottom left of the figure. The gap between the boundary and the first curve indicates that the solution is not changing rapidly there.

component modifications and the movement of the charge density conditions to the distended boundary). However, once again there is a clear reduction in MRMS as the calculation proceeds, indicating that until the calculation was terminated, the solution was converging.

5.3 Summary and Conclusion to the Two-dimensional Steady State Model

A strategy for a two-dimensional, planar steady-state solution to the plasma boundary problem has been proposed, and this is based in part on the second one-dimensional, time-dependent numerical method. The method uses

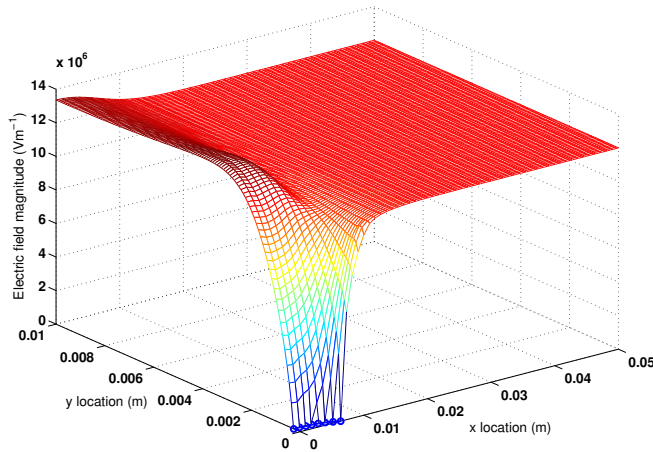


Figure 5.24: The electric field magnitude across the region. The electric field reaches zero at the plasma boundary, as required by (5.2c) (or the dimensionless equivalent).

the notion of space-charge limitation, whereby charge builds up away from a fixed boundary on the interior of an acceleration region, causing a potential maximum and drop in electric field. This happens as a consequence of the fixed boundary being unable to move, and thus for a given region, applied electric field and source charge density combination, charge cannot be accelerated away from the fixed boundary sufficiently quickly. In a moving boundary case, this would result in the boundary moving to increase the electric field near its surface, thus allowing charge to be accelerated away. In the fixed boundary case, however, the build-up of charge effectively creates a new boundary, whereby the electric field at its surface is zero. We detect the location of this boundary, by looking for a potential maximum within the region.

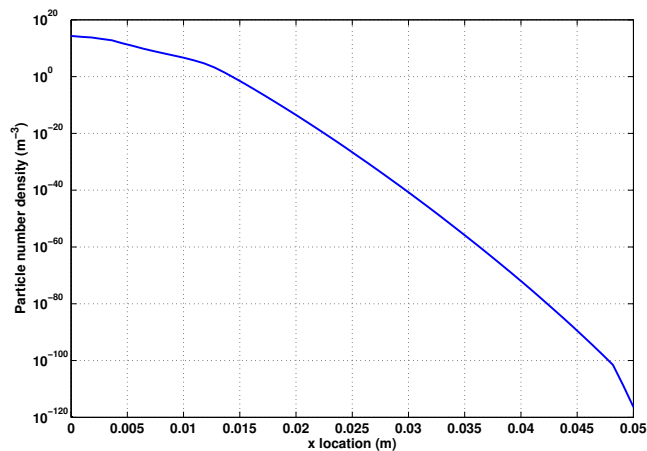


Figure 5.25: The particle number density across the target. The very outer edge of the beam is considered to be when the number density falls below one particle per cubic metre (in this case at 0.014 m).

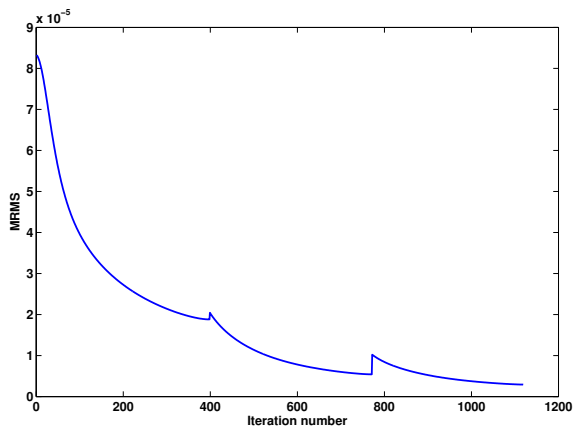


Figure 5.26: MRMS with iteration number - stages 1, 2 and 3.

Within the numerical method proposed, this is done in a number of discrete stages (three in the test problem shown here), where charge density and velocity boundary conditions are moved from the previous boundary lo-

cation, to the new boundary location, and iterations continued until a further potential maximum is found within the region. This process continues until the measure of solution variable change (MRMS) is deemed to be changing sufficiently slowly that the solution has converged.

The test case here shows that the method is entirely plausible and whilst not exhaustive, does indeed show the method converging (in three separate stages), whereby the final resting place of the boundary is close to that of the one-dimensional equivalent solution. The method, as implemented, does not allow for recessed boundaries, and dealing with this is future work.

Chapter 6

Summary, Conclusions and Further Work

6.1 Summary and Conclusions

The problem of determining the plasma free boundary location within an ion accelerator set-up has been considered for many different applications, and is detailed in §1.1.2. The work presented in this thesis has concentrated not only on determining the solution to the free boundary problem originating in a neutron tube acceleration region, but also on the full time-dependent moving boundary problem, of which the free-boundary problem is the steady case.

The formulation of system of non-linear equations describing the moving boundary problem is detailed in Chapter 2, with the full system of non-linear equations describing the time-dependent problem being given by (2.13), and the reduced system of non-linear equations describing the steady-state problem being given by (2.19).

6.1.1 One-Dimensional Steady-state Problem

The one-dimensional free boundary problem is considered in Chapter 3, where the full steady-state system, (2.19), is reduced to one dimension, giving rise to the planar system, (3.1) (with the associated boundary conditions (3.3)), and the radial system, (3.30) (with the associated boundary conditions (3.29)). The full analytical one-dimensional solution to (3.1), subject to (3.3) is developed and is eventually given by the rather unwieldy equation (3.28). However, the similar radial problem, detailed in §3.2, does not appear to be analytically soluble, and so a numerical method is developed that is tested against the analytical planar solution. This is successfully extended to the radial problem, where solution features that are particular to the radial problem, are highlighted.

6.1.2 One-Dimensional Time-dependent Solution

In Chapter 4, a one-dimensional time-dependent solution to the the full system of equations, (2.13), is sought. This is achieved by initially reducing the complexity of the system by making the physically realistic assumption that any magnetic field influence (either by that applied externally, or by that induced as a consequence of the charged particle flow) can be neglected. By doing this, the full one-dimensional time-dependent system can then be written as (4.1), with the associated boundary conditions, (4.2).

The one-dimensional time-dependent system is analysed, giving rise to the analytic expressions, (4.9), describing characteristic curves in the charge free region ahead of the advancing wavefront. Additionally, manipulation of the

time-dependent system allows it to be reduced to the parametric, ordinary, Riccati differential equation, (4.18), in terms of the solution variable $\partial v/\partial x$ (the rate of change of velocity with distance), as a function of the parametric coordinate σ measured along characteristic curves defined within the solution region. The form of the solution to this equation can be relatively easily determined to be (4.23), and is written in terms of $\partial v/\partial x$ as a function of time (to within two constants). One of the resulting constants can be relatively easily determined, and it is also believed that the other can also be determined, although the resulting equation for $\partial v/\partial x$ is likely to be implicit. This is something that will be considered in due course.

In order to develop a full time-dependent solution to the one-dimensional time-dependent system, (4.1), it is first re-written as the dimensionless equations (4.31), (4.33) and (4.34), with the associated dimensionless conditions, (4.36). Following this, two approaches to solving the system are proposed.

6.1.2.1 Numerical Method 1 for the One-dimensional Time-dependent System

The first method proposed for solving the system, (4.31), (4.33) and (4.34) (with associated boundary conditions), begins by mapping the system of equations that are to be solved on a moving domain, to a logical, fixed domain, where standard finite differences can be used to represent the derivatives within the now, logical, system. The mapping process incorporates a solution dependent spatial mapping function which controls nodal spacing in the physical region, and which also varies according to the changing physical

region size. Additionally, the physical time-step is also adjusted by a solution dependent time-step controlling function function, which allows non-constant physical time stepping to be achieved. Once the time-dependent solution has been determined at equally spaced nodes and at equal time-steps in the logical region, it can be transposed onto the unequally spaced nodes and time-steps in the dimensionless physical region, with the full dimensional solution being determined accordingly. Included within the method is a mechanism for determining the location of the moving boundary in dimensionless physical space.

A numerical algorithm for determining the solution of the one-dimensional time-dependent problem in the logical domain is developed and listed in detail; this has been implemented using Matlab. Numerical experimentation indicated that whilst field solutions generated by this method look viable, in order to calculate the boundary location using the mechanism proposed, a small, multiplicative parameter must be introduced to reduce calculated boundary movement at each time-step; without such a parameter, the method rapidly fails. The use of this parameter renders the calculated, time-dependent boundary movement unphysical, whilst additionally causing the algorithm to execute very slowly. These things aside, calculation results are presented for a particular test case in which the charge density applied at the emission boundary is ramped with time¹. Results show viable field solutions, and indicate that the solution dependent spatial and temporal mapping functions are operating as expected. However, as mentioned, the

¹As a result of the slow execution times, to examine the effects of the source charge density switch-on, a rapid charge density ramp is applied; this is only just within experimental range, and is not typical of normal tube operation.

rate of boundary movement is entirely unphysical.

6.1.2.2 Numerical Method 2 for the One-dimensional Time-dependent System

To avoid the problems experienced in the first numerical method, a new approach to the problem is proposed and developed. This new method reduces the number of equations in the system by one, by integrating Gauss' law, (4.35a), and then incorporating it into the Lorentz equation, (4.35b), yielding the coupled pair of equations, (4.75). Additionally, further manipulation of Gauss' law allows the integral equation, (4.79), to be written for the rate of change of boundary location.

A numerical algorithm to implement the new approach is developed and listed in detail. Owing to much improved execution speed, a test case, in which a more experimentally realistic source charge density ramp, is examined. Results clearly show the solution converging to a steady state, indicated by the fact that the calculated boundary location asymptotes to the expected analytic boundary location. Furthermore, boundary perturbation as a function of time, rapidly decays to zero as the calculation progresses. Comparisons between the exact, analytic solution and the time-dependent solution for differing numbers of nodes, show that as the nodal spacing across the region decreases within the time-dependent solution, the error in solution also decreases.

6.1.3 Two-Dimensional Steady-state Problem

A strategy for solving the two-dimensional steady-state problem is proposed, in which space-charge limitation, caused a high source current density at a fixed emitter surface, causes the electric field at the location of the build-up of charge to be neutralised; this effectively indicates the location of the new plasma boundary.

The strategy proposed uses an integral representation of the electric field (in a manner similar to that used in the second one-dimensional time-dependent method) within the Lorentz equation, (5.1a). This equation, representing the time dependence of the velocity field, is then split into its two Cartesian vectorial components, yielding a pair of integro-differential equations for the x and y velocity components. These equations, in addition to the Cartesian forms of the charge continuity equation, (5.10c), and Gauss' Law, (5.10d), now represent the system to be solved for the two-dimensional steady-state problem. But as in the one-dimensional time-dependent model, they are initially written in dimensionless form.

The numerical method developed, solves the system, (5.14), (5.16a), (5.16b), and (5.18), subject to the conditions, (5.19), on a fixed computational domain, using differences to represent derivatives. The initial solution, with a flat, fixed emission boundary proceeds until a potential maximum is detected within the interior of the solution domain. At this point, iterations are terminated and the location of the zero electric field level curve determined; this location (or the computational nodes nearest it) now represents the emission boundary for the next stage of calculation. Velocity components along the boundary are then updated as a consequence of its, now, curved shape. The

charge density and potential boundary conditions are then applied to the new boundary and iterations restarted, with any integration from the emission region starting at the new boundary; nodes behind the boundary are removed from the calculation. This process is repeated a number of times, until no further solution maximum is detected within the interior of the region, and the rate of change of MRMS (the mean root-mean-square change in solution between iterations, of all four solution variables) falls below a specified tolerance.

A test case, using typical conditions applied to a neutron tube (that it is expected will not result in a largely distended boundary), is examined. Results from the three stages of the calculation are displayed, where the boundary is clearly seen to advance into the solution region as iterations and stages progress. In stage 1, results show the advancement of charge into the region, with particles attaining a lateral acceleration as they progress towards the target. The MRMS at stage 1 clearly reduces with iteration number, showing convergence of the method until it was terminated. Results from the latter two calculation stages show the advancement of the boundary towards its resting place, just below the expected one-dimensional boundary location. An indication of the calculated beam splaying at the target is also shown, whilst MRMS decreases within each of the calculation stages.

The method, whilst a little unrefined at this point, is clearly plausible, offering a viable solution approach to the steady-state two-dimensional problem. Refinement of the method could include a better representation of the boundary, instead of it being represented by the discrete nature of the underlying computational grid. This could be done using a different numerical

approach (finite elements), or by modifying the difference equations near the boundary to accommodate its curved nature. Furthermore, as it stands, the method is unable to calculate recessed boundaries; part of the boundary calculated within the test case is likely to be recessed.

The methods and results detailed in this thesis offer not only an analytic expression for the planar one-dimensional steady-state plasma boundary problem for particles emitted with an initial energy from the plasma boundary, but also an insight into the rapid, time-dependent charge flow and plasma boundary movement that occurs over short periods of time immediately following neutron tube switch-on. These methods could be developed to model other charged particle accelerators that incorporate similar plasma sources.

6.2 Further Work

Throughout this work, a number of areas have come to light that merit further study; these are listed in their order of occurrence within the thesis.

1. A full study into analytical solution to the one-dimensional time-dependent planar system of equations (presented in §4.2.2) is to be carried out, with the aim of determining closed form analytic solutions on characteristic curves throughout the charge infused solution region.
2. A more accurate boundary representation within the two-dimensional steady-state model needs to be developed. This should accommodate situations in which recessed boundaries occur.
3. Two-dimensional solutions are to be tested against an experimental

set-up designed to give real physical information on the dimensions of the charged ion beam, as it strikes the ion accelerator target. The experimental set-up to be used is shown in Figure 6.1, where the source shield at the bottom left of the Figure is designed to represent planar emission with the incorporation of an elongated emission slot (this is labelled "Plasma Emission Region" in the accompanying schematic). The set-up shown is encased in a large (relative to the acceleration re-

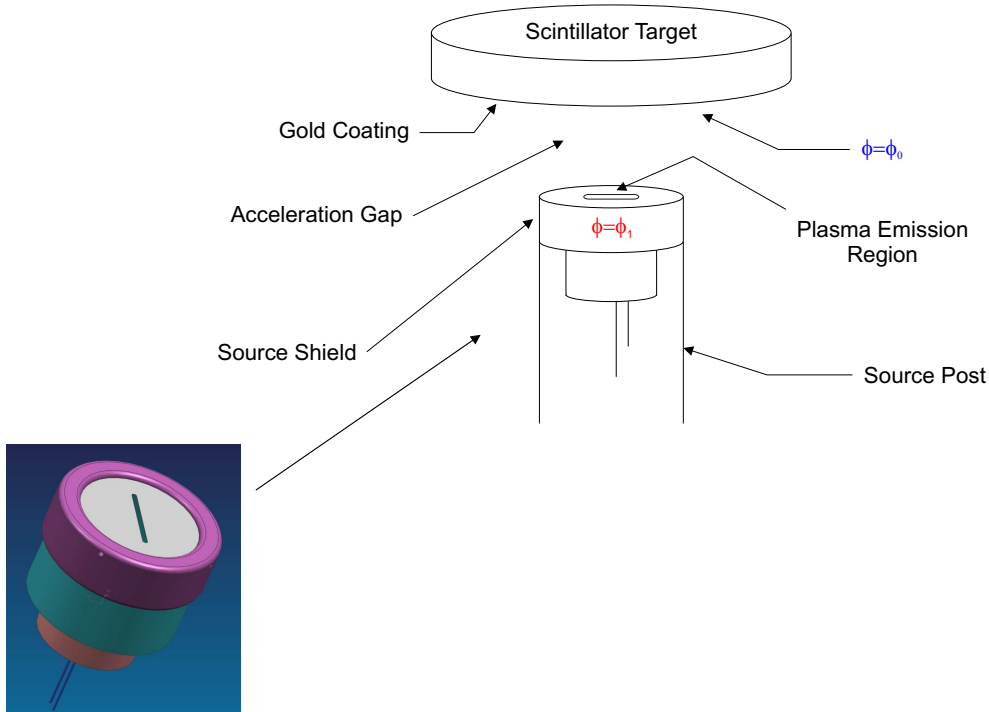


Figure 6.1: Experimental accelerator set-up. The components shown in the schematic are encased in a sealed envelope, with the required potential difference between the source shield and target scintillator applied with a large pulse forming network.

gion shown) sealed envelope, with the required short pulse acceleration

potential difference, applied across the acceleration gap between the source shield and scintillator target, by a large pulse forming network. Ions released from the plasma emission region strike the scintillator target where they are absorbed, and their kinetic energy released in the form of light that can be photographed by a high speed camera. Comparisons can then be made between the predicted ion beam width as it strikes the target, and the recorded scintillation photographs. Components for this experiment have already been designed and procured for use in existing facilities.

This experimental study will determine the validity of the mathematical model used and perhaps indicate modifications that may be necessary to capture the physics more effectively (such as tuning the charge density ramp in both space and time at the plasma emission region). Similar experimental studies, representing a cylindrically symmetric situation, say, will also be helpful in the longer term in further validating the modelling methodology when used in associated problems.

4. The work presented here is potentially informative in the modelling of other related problems, and the methodology for solving them. Industry largely uses a Lagrangian approach to charged particle beam modelling, but we have shown that the Eulerian framework is equally viable, offering potential advantages not seen in the Lagrangian approach (for example short timescale resolution of boundary movement). So there is the prospect that a significant amount of research could follow from the start made here.

Appendix A

D-T Fusion Reaction

Cross-Sections

For a fast moving particle incident upon a stationary target particle, the total fusion reaction cross-section is the apparent target area, as seen by the incident particle as it approaches the other. It is effectively a measure of the probability that a reaction will take place between those particles and is dependent upon the kinetic energy of the interaction.

For a fusion reaction between two ions, if the incident ion strikes the target ion with a low kinetic energy, it will be unable to penetrate the coulombic barrier existing between the two particle nuclei, thus causing the reaction probability (or the effective target area) to be low¹. If the incident ion strikes the target ion with a very high kinetic energy, whilst it will be able to penetrate the coulombic barrier existing between their two nuclei, the incident ion

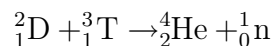
¹It is understood that the larger the target ion apparently is, the more likely the incident ion is to hit that target.

will be less likely to be captured by the target ion nucleus², thus scattering from it and again causing the reaction probability to be low. At a range of energies specific to the given reacting ion species, the probability of the incident ion nucleus being captured by the target ion nucleus is relatively high; at these energies, fusion between the particles is more likely.

We now explain how, for a fast moving ion incident upon a target ion that is stationary relative to the laboratory, the reaction cross-section in the laboratory can be determined from that given in, what is known as, the centre-of-mass (CM) frame of reference. The following analysis is taken, in part, from [21].

A.1 Kinetic Energy in the CM Frame of Reference.

For a pair of reacting particles, the laboratory frame of reference (L) is that frame which is stationary with respect to the laboratory; the CM frame of reference is defined as the frame in which the total momentum of the reacting particles is zero. To determine the relationship between the total kinetic energy of such a pair of particles measured in the CM frame of reference, and the kinetic energy for the same reaction measured in the laboratory, we consider the deuterium-tritium fusion reaction



²To be captured, the incident ion must approach the target nucleus to within a radius of 10^{-15}m , and must not have so much energy that it can escape the nuclear strong force existing at that radius.

in L, where D and T are the reacting deuterium and tritium ions, respectively; He and n are the helium nucleus and neutron, reaction products, respectively. The superscripts refer to the particle mass number, and are given in atomic mass units,³ whereas the subscripts refer to the particle atomic number, or the number of protons in its nucleus. Here, the deuterium ion is accelerated in a positive direction towards the stationary (relative to the laboratory) tritium ion; upon interaction, the fusion reaction takes place.

In the L frame, the total momentum of the the reacting particles is given by

$$p = m_D v_D,$$

with the total kinetic energy being

$$E = \frac{1}{2} m_D v_D^2, \quad (\text{A.1})$$

where m_D and v_D are the deuterium mass and velocity measured in the L frame. In the CM frame, the total momentum of the reacting particles is correspondingly

$$\begin{aligned} \bar{p} &= m_D \bar{v}_D + m_T \bar{v}_T, \\ &= 0, \end{aligned} \quad (\text{A.2})$$

with the total kinetic energy being

$$\bar{E} = \frac{1}{2} (m_D \bar{v}_D^2 + m_T \bar{v}_T^2), \quad (\text{A.3})$$

where m_T is the mass of the tritium ion, and where the over-line denotes quantities measured in the CM frame (\bar{v}_T is the velocity of the tritium ion

³An atomic mass unit is effectively the mass of a nucleon, or nuclear particle. Hence a particle with a given *mass* of 3 say, effectively consists of 3 nucleons.

in the CM frame, for example). Since the CM frame of reference moves in a positive direction relative to the laboratory, we denote the velocity of it, as measured in L, by v_{CM} . Furthermore, since only the deuterium ion is moving in L, then

$$\bar{v}_D = v_D - v_{CM} \quad (\text{A.4})$$

$$\bar{v}_T = -v_{CM}, \quad (\text{A.5})$$

where upon substitution of (A.4) and (A.5) into (A.2), we deduce that

$$v_{CM} = \left(\frac{m_D}{m_D + m_T} \right) v_D;$$

consequently

$$\begin{aligned} \bar{v}_D &= \left(1 - \frac{m_D}{m_D + m_T} \right) v_D \\ &= \left(\frac{m_T}{m_D + m_T} \right) v_D, \end{aligned} \quad (\text{A.6})$$

from (A.4). The total kinetic energy \bar{E} in the CM frame is then

$$\begin{aligned} \bar{E} &= \left(\frac{m_T}{m_D + m_T} \right) \frac{1}{2} m_D v_D^2 \\ &= \left(\frac{m_T}{m_D + m_T} \right) E \end{aligned} \quad (\text{A.7})$$

from (A.1) and (A.3) - (A.6).

A.2 Reaction Cross-Section in the CM and L Frames of Reference.

Given (A.7), if we know the function $\bar{\sigma}(\bar{E})$ representing the D-T reaction cross-section over a range of kinetic energies in the CM frame of reference, we

can scale this function's dependent variable (\bar{E}) by an appropriate parameter λ_L , where

$$\lambda_L = \frac{m_D + m_T}{m_T},$$

to give the equivalent function expressed in the laboratory (i.e. $\sigma(E) = \bar{\sigma}(\lambda_L \bar{E})$). Figure A.1 shows the effect of scaling the CM generic D-T reaction cross-section curve (in black) to give both the D-T reaction (in blue) in the laboratory (where deuterium is incident upon tritium), and the T-D reaction (in red) in the laboratory (where tritium is incident upon deuterium).

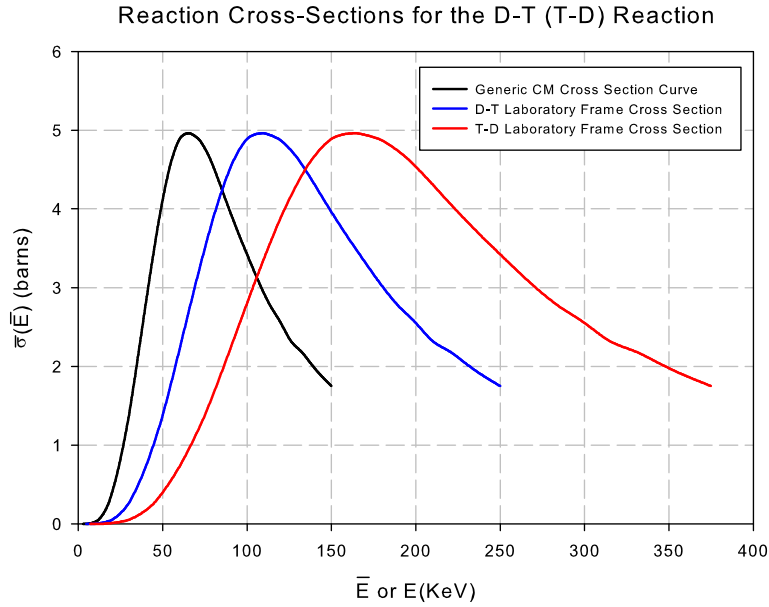


Figure A.1: Reaction cross-section as a function of energy for the D-T reaction in the CM frame of reference (black), with the scaled cross-sections for both the D-T (red) and T-D (blue) in the laboratory frame of reference also shown. The cross-section peaks occur at $\bar{E} \sim 66$ KeV for the CM frame, $E \sim 110$ KeV for D-T in the laboratory frame and $E \sim 165$ KeV for T-D in the laboratory frame. The original CM curve was taken from [4] and [5].

Appendix B

Magnetic Field Effects

In a neutron tube no external magnetic field is applied during its operation, and so the only possible contribution to \mathbf{B} , on the right hand side of (2.13a), is the magnetic field induced by the current of charged particles themselves as they flow across the region. Such a magnetic field is naturally induced by the electric field advection, caused by this passage of charged particles, and is a consequence of the continuity equation (2.13b) and of the electric field divergence, (2.13c); it can be derived as follows.

- **Magnetic field induction due to current flow**

By equating the time derivative of (2.13c) to (2.13b), we have

$$\nabla \cdot \left\{ \rho \mathbf{v} + \varepsilon_0 \frac{\partial \mathbf{E}}{\partial t} \right\} = 0,$$

so that upon integration we obtain,

$$\rho \mathbf{v} + \varepsilon_0 \frac{\partial \mathbf{E}}{\partial t} = \mathbf{g}(t), \tag{B.1}$$

where the vector function $\mathbf{g}(t)$ can be a function of time only. By comparing (B.1) to the well known differential form of Ampère's law

(noting the definition (2.16)),

$$\mu_0 \left(\mathbf{J} + \varepsilon_0 \frac{\partial \mathbf{E}}{\partial t} \right) = \nabla \times \mathbf{B} \quad (\text{B.2})$$

(see [14], for example), we see that $\mathbf{g}(t) = \frac{1}{\mu_0} \nabla \times \mathbf{B}$, with the implication that $\nabla \times \mathbf{B}$ must also be a function of time only; here, μ_0 is a scaling parameter known as the permeability of free space. Re-writing (B.2) using (2.13c) we obtain

$$\left(\mathbf{v} \nabla \cdot \mathbf{E} + \frac{\partial \mathbf{E}}{\partial t} \right) = c^2 \nabla \times \mathbf{B}, \quad (\text{B.3})$$

where $c = \sqrt{1/\mu_0 \varepsilon_0}$ is the speed of light in vacuum, with the immediate conclusion being that the flow of charged particles naturally introduces electric field advection, which in turn introduces a magnetic field that is perpendicular to the particle flow. The curl of this field is purely time dependent and by writing $\mathbf{f}(t) = \mathbf{g}(t)/\varepsilon_0 = c^2 \nabla \times \mathbf{B}$, we can say in two Cartesian dimensions that

$$\begin{aligned} \mathbf{f}(t) &= f_1(t) \hat{\mathbf{i}} + f_2(t) \hat{\mathbf{j}}, \\ &= c^2 \nabla \times \mathbf{B} \\ &= c^2 \left[\left(\frac{\partial B_z}{\partial y} - \frac{\partial B_y}{\partial z} \right) \hat{\mathbf{i}} - \left(\frac{\partial B_z}{\partial x} - \frac{\partial B_x}{\partial z} \right) \hat{\mathbf{j}} \right]. \end{aligned} \quad (\text{B.4})$$

In this thesis, we are only concerned with planar tube models in one and two dimensions, with a planar, two-dimensional (in the independent variables x and y) region being effectively the cross-section of a prism extending infinitely into the z direction. Hence, in this framework, partial derivatives in the z direction are zero, implying that the

functions $f_1(t)$ and $f_2(t)$ are given by

$$f_1(t) = c^2 \frac{\partial B_z}{\partial y}, \quad (\text{B.5a})$$

$$f_2(t) = -c^2 \frac{\partial B_z}{\partial x}, \quad (\text{B.5b})$$

since $\partial B_y / \partial z = \partial B_x / \partial z = 0$. We can then say that

$$c^2 B_z = y f_1(t) + \mathcal{F}_1, \quad (\text{B.6})$$

from (B.5a), and

$$c^2 B_z = -x f_2(t) + \mathcal{F}_2, \quad (\text{B.7})$$

from (B.5b), where \mathcal{F}_1 and \mathcal{F}_2 are arbitrary functions of (x, t) and (y, t) , respectively. By combining (B.6) and (B.7), the z component of the self-induced magnetic field can be written

$$B_z = \frac{1}{c^2} (y f_1(t) - x f_2(t)) + \mathcal{G}(t), \quad (\text{B.8})$$

where \mathcal{G} is an arbitrary function of time, clearly showing that the electric field advection induces the perpendicular magnetic field component $B_z = B_z(x, y)$. This component is small, indicated by the presence of $1/c^2$ on the right hand side of (B.8). Moreover, the presence of c^2 on the right hand side of (B.3) offsets the small magnitude of the self-induced field \mathbf{B} , making the vector function $\mathbf{f}(t)$ comparable to the electric field advection, thus balancing (B.3). The implication here is that both $\nabla \times \mathbf{B}$ and B_z are small functions (the presence of c^2 in both cases clearly indicates this) relative to the electric field advection propagated by the charged particle flow.

We now seek to further show that the effects of the small self-induced magnetic field on charged particle flow are also negligible in comparison to the effects caused by the application of the external electric field.

- **Effect of self-induced magnetic field on particle acceleration**

The component of accelerative force acting on the charged particle beam as a consequence of any magnetic fields is given by

$$\mathbf{F}_B = q\mathbf{v} \times \mathbf{B}, \quad (\text{B.9})$$

from (2.13a), or in this case, because the only magnetic field present is that due to self-induction,

$$\mathbf{F}_B = q \left[(v_y B_z) \hat{\mathbf{i}} - (v_x B_z) \hat{\mathbf{j}} \right], \quad (\text{B.10})$$

since the self-induced magnetic field only has a component perpendicular to the direction of particle motion (given by (B.8)), and where v_x and v_y are the x and y components of the particle velocity, respectively.

One-dimensional case

In one dimension, acceleration in the $\hat{\mathbf{j}}$ direction can be ignored, and additionally, there is no component of particle velocity in this direction. This implies (from (B.10)) that in one dimension, acceleration due to self-induced magnetic field can be ignored.

Two-dimensional case

From (B.10), it can be seen that in two dimensions, the magnitude of the self-induced magnetic field can cause an accelerative force in the $x-y$ plane. However, as a consequence of the presence of $1/c^2$ in (B.8), we know that the self-induced magnetic field component, B_z , must be small in comparison to any electric field advection caused by the charged particle flow, but we do not know the sizes of the functions $f_1(t)$, $f_2(t)$ and $\mathcal{G}(t)$. Nonetheless, an estimate of the magnitude of the

self-induced magnetic field can be determined from the Biot-Savart law ([14], p296) where its magnitude some distance r radially away from a long, current-carrying conductor (such as a neutron tube acceleration gap) carrying a current I , is given by

$$|\mathbf{B}| = \frac{\mu_0 I}{2\pi r}. \quad (\text{B.11})$$

From (B.9), the magnitude of the component of the force acting on the beam of charged particles, due to the self-induced magnetic field at r is then

$$\begin{aligned} |\mathbf{F}_B| &= q|\mathbf{B}||\mathbf{v}| \\ &= \frac{q\mu_0 I|\mathbf{v}|}{2\pi r}. \end{aligned} \quad (\text{B.12})$$

Choosing r to be of the order of the ion beam radius ($r \simeq 10^{-3}$ m), we find that for a typical 1A ion current, with the mean ion velocity being that of a particle with 50KeV energy (the typical mean energy of a deuteron within a neutron tube acceleration region), the magnitude of the force due to the self-induced magnetic field at one ion beam radius is $|F_B| \simeq 7 \times 10^{-17}$ N. In contrast, the magnitude of the component of the force acting on the charged particles due to the applied electric field,

$$|\mathbf{F}_E| = q|\mathbf{E}|$$

(from (2.13a)), is some five orders of magnitude greater for a typical acceleration potential difference of ~ 100 kV and acceleration gap of $\sim 10^{-2}$ m. With this in mind, the contribution to particle acceleration in (2.13a) (perpendicular to the direction of particle flow) due to the

self-induced magnetic field is deemed negligible and, in conjunction to experimental experience, allows it to be disregarded in this study.

- **Time varying magnetic field influence.**

The link between the electric and magnetic fields via the time derivative of the magnetic vector potential in (2.13e) implies that

$$\nabla \times \mathbf{E} = -\frac{\partial \mathbf{B}}{\partial t}, \quad (\text{B.13})$$

from (2.13f). Consequently, in the presence of a time varying magnetic field (as is the case with charged particle flow, shown in (B.8)), the electric field defined by (2.13f) clearly has the non-zero curl, (B.13), and cannot truly be considered a conservative field. However, by examining (B.13), we can show that no matter how large the rate of change of magnetic field at the wavefront is, it can be neglected, validating a conservative field approximation. We do this by expanding the curl term on the left hand side of (B.13), giving

$$\nabla \times \mathbf{E} = \hat{\mathbf{i}} \left(\frac{\partial E_z}{\partial y} - \frac{\partial E_y}{\partial z} \right) + \hat{\mathbf{j}} \left(\frac{\partial E_x}{\partial z} - \frac{\partial E_z}{\partial x} \right) + \hat{\mathbf{k}} \left(\frac{\partial E_y}{\partial x} - \frac{\partial E_x}{\partial y} \right), \quad (\text{B.14})$$

where E_x represents the component of \mathbf{E} in the x direction etc. Given that $\mathbf{E}(\mathbf{x}, t)$ is, at most, a two-dimensional field (in this thesis), its z component does not exist; moreover, derivatives in the z direction are zero. With these things in mind, (B.14) can be reduced to

$$\nabla \times \mathbf{E} = \hat{\mathbf{k}} \left(\frac{\partial E_y}{\partial x} - \frac{\partial E_x}{\partial y} \right), \quad (\text{B.15})$$

showing that $\nabla \times \mathbf{E}$, and consequently $\partial \mathbf{B} / \partial t$ (consistently with (B.8)) only have a non-zero component pointing out of the x - y plane. There-

fore, in the $x-y$ plane we must conclude

$$\nabla \times \mathbf{E} = 0,$$

from (B.15), implying that the electric field is conservative (with no vorticity) and that

$$\mathbf{E} = -\nabla\phi \tag{B.16}$$

must be true for some ϕ , from (2.13e). Hence, for the purposes of this study, (2.18) is considered the definition the electric field $\mathbf{E}(\mathbf{x}, t)$ for the scalar potential $\phi(\mathbf{x}, t)$.

Acknowledgements

Many things have changed in my life over the last seven years during which I have been studying to write this thesis. There have been several periods of time where my personal life and work have dramatically hindered study, with the thought of completing it sometimes feeling like a pot of gold at the end of a rainbow, to be seen but never reached. The arrival of my son, Charlie, brought everything firmly into focus, giving me the additional impetus needed to reach the pot.

Throughout this time my supervisors, Professors Mike Baines and Dave Porter, have somehow maintained interest in me and this work, and guided me expertly to this point; they have been superb role models. I would not have been able to finally get here without Mike's incisive eye, his huge experience, and his ability to point out the obvious (when the obvious sometimes didn't seem obvious), or without his patience and help when I needed it. Dave has been an unyielding source of inspiration; his precise, analytical way of looking at things and his use of English have taught me and changed me for the rest of my life; I am certain of that. They are both far too modest to accept such comments from me, but they are sincerely meant; it is for these reasons that I owe them both my deepest gratitude.

The company I work for, AWE plc, have sponsored this work for the entire seven years, and for that I am most grateful; they have been very generous with their time and money.

Finally, I would like to dedicate this thesis to my Mum and Dad, Mary and Maurice Spence. Mum, you have been wonderful to Charlie and you

have had faith in me throughout some really difficult times, when I may not have had such faith in myself - thank you Mum. Dad, you set me on this path when I was very young and all the hours you spent showing me how to fix things, teaching me what you knew when I asked why, were never wasted; I have and always will remember - thank you Dad.

Bibliography

- [1] L Tonks and I Langmuir, *Oscillations in Ionised Gases*; Physical Review, 33, 195; February 1929
- [2] L Tonks and I Langmuir, *A General Theory of the Plasma of an Arc*; Physical Review, 34, 876; September 1929
- [3] K R Spangenburg, *Vacuum Tubes*, McGraw Hill, 1948
- [4] H V Argo, R F Taschek, H M Agnew, A Hemmendinger, and W T Leland; *Cross Sections of the $D(T,n)He^4$ Reaction for 80 to 1200KeV Tritons*; Physical Review, 87, 612; August 15, 1952
- [5] J P Conner, T W Bonner, and J R Smith; *A Study of the $H^3(d,n)He^4$ Reaction*; Physical Review, 88, 468; November 1st, 1952
- [6] Sir Harold Jeffreys and Bertha Swirles, *Methods of Mathematical Physics - Third Edition*; Cambridge University Press, 1956
- [7] S A Self, *Exact Solution of the Collisionless Plasma Sheath Equation*; The Physics of Fluids, Vol 6, No. 12; December 1963

- [8] J Hyman Jr, W O Eckhardt, R C Knechtli, C R Buckley; *Formation of Ion Beams from Plasma Sources: Part 1*; AIAA Journal, Vol. 2, No. 10; October 1964
- [9] A M Winslow, *Numerical Solution of the Quasilinear Poisson Equation on a Non-Uniform Triangular Mesh*; Journal of Computational Physics, Vol 2, p149-172; 1967
- [10] C W Hirt, A A Amsden J L Cook; *An Arbitrary Lagrangian-Eulerian Computing Method for All Flow Speeds*; Journal of Computational Physics, Vol 14, p227-253; 1974
- [11] AWE Internal Report (unpublished), July 1975
- [12] J H Whealton, E F Jaeger and J C Whitson; *Optics of Single Stage Accelerated Ion Beams Extracted from a Plasma*; Journal of Computational Physics, Vol 27, No. 1; February 1977
- [13] J H Whealton, E F Jaeger and J C Whitson; *Optics of Single Stage Accelerated Ion Beams Extracted from a Plasma*; Rev. Sci. Instrum, Vol 48, No. 7, 829; July 1977
- [14] Martin A Plonus, *Applied Electromagnetics*; McGraw Hill, 1978
- [15] G Aston and P J Wilbur, *Ion Extraction from a Plasma*; Journal of Applied Physics, Vol 52(4), p2614; April 1981
- [16] C Lejeune, *Extraction of high-intensity ion beams from plasma sources: Theoretical and experimental treatments*; Advances in Electronics and Electron Physics, Supplement, Vol 13, p207; January 1983

- [17] J Crank, *Free and Moving Boundary Problems*, Clarendon Press, 1984
- [18] A Beiser, *Concepts of Modern Physics - 4th Edition*; McGraw Hill, 1987
- [19] Erwin Kreyszig, *Advanced Engineering Mathematics - Sixth Edition*; Wiley, 1987
- [20] L Fox and D F Mayers, *Numerical Solution of Ordinary Differential Equations - for Scientists and Engineers*; Chapman and Hall, 1987
- [21] K S Krane, *Introductory Nuclear Physics*, Wiley, 1988
- [22] J H Whealton, M A Bell, R J Raridon, K E Rothe and P M Ryan; *Computer Modelling of Negative Ion Beam Formation*; Journal of Applied Physics, Vol 64(11), p6210; December 1988
- [23] K J Binns, P J Lawrenson and C W Trowbridge; *The Analytical and Numerical Solution of Electric and Magnetic Fields*; Wiley, 1992
- [24] Randall J LeVeque, *Numerical Methods for Conservation Laws*; Birkhauser, 1992
- [25] B Abraham-Shrauner, *Hidden Symmetries and Lienarisation of the Modified Painlevé-Ince Equation*; Journal of Mathematical Physics, Vol 34, p4809; 1993
- [26] K W Morton and D F Mayers, *Numerical Solution of Partial Differential Equations*, Cambridge University Press, 1994
- [27] P Girdinio, M Repetto, and J Simkin; *Finite Element Modelling of Charged Beams*; IEEE Transactions on Magnetics, Vol 30, No. 5, p2932; September 1994

- [28] S Humphries Jr, *Numerical Modelling of Space Charge Limited Charged Particle Emission on a Conformal Triangular Mesh*; Journal of Computational Physics, Vol 125, p488; October 1996
- [29] P C Matthews, *Vector Calculus*, Springer-Verlag Berlin, January 1998
- [30] P J Spence. *Use of Adaptive Grid Methods in the Solution of a 1D Second Order ODE*, AWE Internal Memo, 1998
- [31] Y Okawa and H Takegahara, *Numerical Study of Beam Extraction Phenomena in an Ion Thruster*; Japanese Journal of Applied Physics, Vol 40, p314; January 2001
- [32] R Hippler, S Pfau, M Schmidt, K Schoenbach; *Low Temperature Plasma Physics*; Wiley-VCH, 2001
- [33] M J Baines, *A Lagrangian Moving Finite Element Method Incorporating Monitor Functions*, Proceedings of SCA03 Conference, Hong Kong, Jan 2003
- [34] P J Spence, *The Position of the Free Boundary Formed Between an Expanding Plasma and an Electric Field in Differing Geometries*, MSc Dissertation, University of Reading, September 2003
- [35] A D Polyanin and V F Zaitsev, *Handbook of Exact Solutions for Ordinary Differential Equations*; 2nd edition, Chapman and Hall, Boca Raton; 2003
- [36] Daniel Zwillinger, *CRC Standard Mathematical Tables and Formulae*; 31st edition, Chapman and Hall, CRC Press LLC; 2003

- [37] S Humphries Jr, *Modeling Ion Extraction from a Free-Plasma Surface with a Flexible Conformal Mesh*; Journal of Computational Physics, Vol 204, p587; 2005
- [38] Peter J Collins, *Differential and Integral Equations*, Oxford University Press, 2006
- [39] Heydorn, *Neutron Activation Analysis*, CRC Press, March 2009
- [40] B Cameron Reed, *The Physics of the Manhattan Project*, Springer-Verlag Berlin, October 2010
- [41] Umran S Inan and Marek Golkowski, *Principles of Plasma Physics for Engineers and Scientists*, Cambridge University Press, December 2010
- [42] Weizhang Huang and Robert D Russell, *Adaptive Moving Mesh Methods*; Applied Mathematical Sciences, Vol 174, p215-280; 2011
- [43] Supriya Mukherjee *et al.*, *Solution of Modified Equations of Emden-Type by Differential Transform Method*; Journal of Modern Physics, Vol 2, P559-563; 2011